SLAC-R-616
UC-414

A Precision Measurement of the Spin Structure Function G(2) (P)*

Nawal Benmouna

Stanford Linear Accelerator Center
Stanford University
Stanford, CA 94309

SLAC-Report-616
2001

Prepared for the Department of Energy
under contract number DE-AC03-76SF00515

Printed in the United States of America. Available from the National Technical Information Service, U.S. Department of Commerce, 5285 Port Royal Road, Springfield, VA 22161.

* Ph.D. thesis, American University, Washington DC, 20016.

A PRECISION MEASUREMENT OF THE SPIN STRUCTURE FUNCTION $\mathbf{g}_2^p$

by

Nawal Benmouna

submitted to the

Faculty of the College of Arts and Sciences

of American University

in Partial Fulfillment of

the Requirements for the Degree

of Doctor of Philosophy

in

Physics

Chair:

Raymond G. Arnold

Stephen E. Rock

Peter E. Bosted

Larry R. Medsker

Dean of the College

Date

2001

American University

Washington, D.C. 20016

A Precision Measurement of the Spin Structure Function g_2^p

BY

Nawal Benmouna

ABSTRACT

The spin structure function $g_2(x, Q^2)$ and the virtual photon asymmetry $A_2(x, Q^2)$ were measured for the proton using deep inelastic scattering. The experiment was conducted at the Stanford Linear Accelerator Center (SLAC), where longitudinally polarized electrons at 29.1 and 32.3 GeV were scattered from a transversely polarized NH_3 target. Large data sets were accumulated using three independent spectrometers covering a kinematic range $0.02 \leq x \leq 0.8$ and $1 \leq Q^2 \leq 20$ $(\mathrm{GeV/c})^2$. This new data is the first data precise enough to distinguish between current models for the proton. The structure function g_2^p was found to be reasonably consistent with the twist-2 Wandzura-Wilczek calculation. The Q^2 dependence of g_2 approximately follows the Q^2 dependence of g_2^{WW}, although the data are not precise enough to rule out no Q^2 dependence. The absolute value for A_2^p was found to be significant smaller than the Soffer limit over the measured range. The virtual photon asymmetry A_2 was also found to be inconsistent with zero over much of the measured range.

ACKNOWLEDGEMENTS

I would like to thank my advisors, Professors Raymond Arnold, Peter Bosted, and Steve Rock for giving me the opportunity to participate in an exciting project, and setting the example for excellence in work.

I would also like to thank the members of the E155X collaboration who contributed to the success of the experiment, in particular my fellow thesis students.

Special thanks to Dr. Lee Sorrell whose help truly made this work possible in so many ways. Lee's dedication to the students is unparalleled.

Back in the American University physics department, I would like to thank Professor Larry Medsker for taking the time to serve on my committee, Professor Howard Reiss for always doing everything possible to help the students, and Yana Shabaev who, even through hard times, manages to look out for everyone.

To my friends who from far away called to offer their support, to those who made life nicer at SLAC, thanks to all of you.

Most of all, I would like to thank my dear family for their continuous love and caring. My parents and my brother have given me the courage and strength to pursue my dreams. Your love, support and encouragement have allowed me to complete this challenging project, and it is to you that I dedicate this work.

CONTENTS

LIST OF TABLES

LIST OF FIGURES

CHAPTER 1

Introduction

Understanding the fundamental nature of matter is an ongoing effort that has lead to many discoveries along the way. Atoms which were once believed to be the most elementary particles, were found to be composed of *electrons*, *protons*, and *neutrons* (protons and neutrons are known as nucleons). Later on, the nucleons were found to be composed of *quarks*. In the current view of the composition of matter, described by the Standard Model, quarks are fundamental particles. The interaction between quarks is mediated by *gluons* and is described by the theory of strong interactions known as Quantum Chromodynamics (QCD). So far, quarks have only been observed bound to other quarks forming *baryons* (consisting of three quarks) such as the nucleons, and bound to antiquarks forming *mesons* (consisting of a pair of quark and antiquark). In QCD, a nucleon consists of three quarks known as "valence" quarks and a "sea" containing virtual quark-antiquark pairs known as sea quarks, and gluons. Although QCD is a very complete theory, current mathematical techniques are incapable of performing a full QCD calculation of real physical processes. To get around this problem, perturbative QCD (PQCD) is used. In PQCD, the calculation of physical processes is expanded in terms of the strong

coupling constant α_s. This "constant" is small at high energies (or equivalently, small distance scales), but becomes large at lower energies (or large distance scales). For processes involving very low energies, such as those that give rise to the sea quarks, a perturbative expansion fails to converge because α_s approaches or exceeds 1. However, these low energy terms can be separated from the high energy terms using a process known as factorization. These low energy terms, which include the functions describing the distribution of quarks and gluons within the nucleon (known as "parton distribution functions" or PDFs), must be measured experimentally. Once these measurements have been made, the PDFs can be applied in combination with the PQCD calculation of the hard scattering process to predict the result of any given scattering process. The accuracy of these PQCD predictions depends on both the ability to carry out the calculation to sufficient order in the expansion and the precision of the knowledge of the PDFs. Probing the interactions of the quarks and gluons inside the nucleons is a key to further understanding the nature of matter.

Deep Inelastic Scattering (DIS), explained in detail in the next section, is a powerful tool for investigating the electromagnetic structure of the proton and the neutron. The spin structure of the nucleons is studied using Polarized-DIS. Structure functions, F_1, F_2, g_1 and g_2 are measured to obtain information on different aspects of the nucleon structure. The functions F_1 and F_2 contain the unpolarized parton distributions. The function g_1 arises from the spin distribution in the nucleon. Finally, g_2 arises from the quark-gluon interactions. The functions F_1, F_2 and g_1

have been studied extensively, and are now known to high experimental precision. The current world data existing for these functions come from the efforts of a series of experiments performed at SLAC (E142 [1], E143 [2], E154 [3, 4, 5], and E155 [6, 7, 8]), as well at CERN in Switzerland (EMC [9] and SMC [10]) and at DESY in Germany (HERMES [11, 12]). Theoretical and experimental work on g_2 is still in its early stages, but one major interest in g_2 has been the information it can provide on higher order interactions between the quarks in nucleons, which cannot be calculated exactly using QCD. The subject of this dissertation is the measurement of the spin structure function g_2 for the proton from experiment E155X at SLAC, performed in the Spring of 1999.

The rest of this chapter will explain the formalism of Deep Inelastic Scattering, while the more theoretical basis of g_2 will be explained in Chapter 2. Chapter 3 describes the equipment used for the experiment, and Chapter 4 explains the analysis of the data. Finally, Chapter 5 contains the results of the analysis, followed with a conclusion in Chapter 6. Tables of results are given in Appendices A, B and C.

1.1 Deep Inelastic Scattering

Deep Inelastic Scattering was used in experiment E155X to measure the spin structure function g_2 for the proton and deuteron. The one-photon exchange diagram for the scattering of a lepton incident on a nucleon is shown in Fig. 1. Table 1 lists the kinematic variables used throughout this thesis, and the notation follows Anselmino et al. [13].

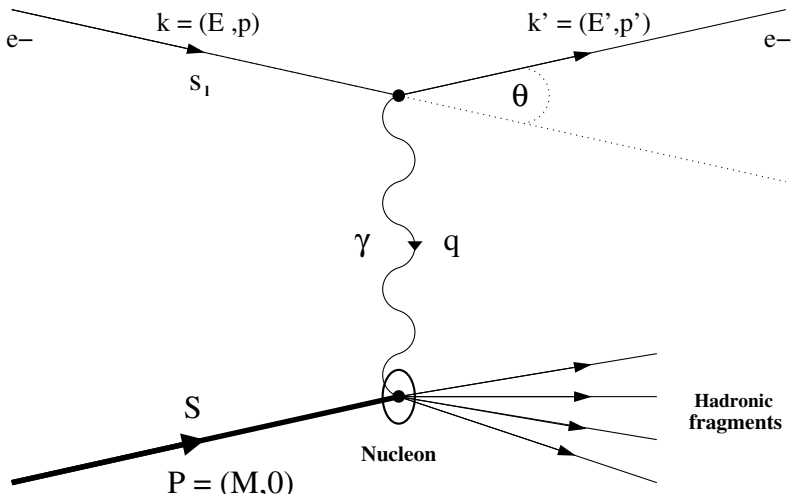

Figure 1: One photon exchange diagram for deep inelastic scattering of an electron off a nucleon.

The differential cross-section for the one-photon exchange diagram is given by

$$\frac{d^2\sigma}{d\Omega dE'} = \frac{\alpha^2}{2MQ^4}\frac{E'}{E}L_{\mu\nu}W^{\mu\nu} \tag{1}$$

where α is the fine structure constant,and $L_{\mu\nu}$ and $W^{\mu\nu}$ are the tensors that describe the lepton and hadrons currents respectively. The leptonic tensor has symmetric and antisymmetric parts ($L_{\mu\nu} = L^{(S)}_{\mu\nu} + L^{(A)}_{\mu\nu}$)

$$L^{(S)}_{\mu\nu} = \quad k_\mu k'_\nu + k'_\mu k_\nu - g_{\mu\nu}(k\cdot k' - m^2) \tag{2}$$

$$L^{(A)}_{\mu\nu} = \qquad\qquad m\epsilon_{\mu\nu\alpha\beta}s^\alpha q^\beta \tag{3}$$

where $g_{\mu\nu}$ is the metric tensor with diagonal elements (1, -1, -1, -1), and $\epsilon_{\mu\nu\alpha\beta}$ is the four dimensional Levi-Cevita tensor. The hadronic tensor $W_{\mu\nu}$ also has symmetric and asymmetric parts ($W_{\mu\nu} = W^{(S)}_{\mu\nu} + W^{(A)}_{\mu\nu}$)

$$W^{(S)}_{\mu\nu} = \quad \left(-g_{\mu\nu} + \tfrac{q_\mu q_\nu}{q^2}\right) W_1(\nu, q^2) + \tfrac{1}{M^2}\left(P_\mu - \tfrac{P\cdot q}{q^2}q_\mu\right)\left(P_\nu - \tfrac{P\cdot q}{q^2}q_\nu\right) W_2(\nu, q^2) \tag{4}$$

$$W^{(A)}_{\mu\nu} = \qquad \epsilon_{\mu\nu\alpha\beta}q^\alpha\left\{\mathbf{S}_\beta M G_1(\nu, Q^2) + \tfrac{1}{M}\left[(P\cdot q)\mathbf{S}_\beta - (S\cdot q)P_\beta\right] G_2(\nu, Q^2)\right\}. \tag{5}$$

M	Nucleon Mass
m	Lepton mass
E	Incident lepton energy
E'	Scattered lepton energy
$k = (E, \vec{k})$	Incident lepton four-momentum
$k' = (E', \vec{k}')$	Scattered lepton four-momentum
$\nu = E - E'$	Virtual photon energy
$q = k - k'$	Four-momentum of virtual photon
$Q^2 = -q^2 = 4EE' \sin^2(\frac{\theta}{2})$	Four-momentum transfer
$x = \frac{Q^2}{2M\nu}$	Bjorken scaling variable
θ	Laboratory scattering angle of lepton
s	Lepton spin
$\mathbf{S}$	Nucleon spin
P	Four momentum of nucleon

Table 1: Kinematic variables.

In Eqs. 4 and 5, $W_1(\nu, Q^2)$, $W_2(\nu, Q^2)$, $G_1(\nu, Q^2)$ and $G_2(\nu, Q^2)$ are independent form factors which contain information about the structure of the nucleon.

The sum of cross-sections with opposite lepton spins cancels out polarized terms and thus leads to the expression of the unpolarized cross-section (cross-section of unpolarized leptons incident on unpolarized nucleons). In contrast, the difference of cross-sections with opposite lepton spins cancels out terms which do not contain the spin of the lepton or the nucleon, leaving only polarized terms. The form factors W_1 and W_2, also known as structure functions, contribute to the *unpolarized* DIS cross-section. The form factors G_1 and G_2, also known as structure functions, contribute to the *polarized* DIS cross-section.

Consider the case of longitudinally polarized leptons (along the direction of $\vec{k}$) and nucleons which are polarized along an arbitrary direction $\vec{\mathbf{S}}$ as seen in Fig. 2.

Adding the cross-sections for opposite lepton spin directions we obtain

$$\frac{d^2\sigma^{\rightarrow,\mathbf{S}}}{d\Omega dE'} + \frac{d^2\sigma^{\leftarrow,\mathbf{S}}}{d\Omega dE'} = 2\frac{d^2\sigma^{unp}}{d\Omega dE'} \tag{6}$$

where the notation $(\rightarrow, \mathbf{S})$ refers to spin orientation of the lepton (longitudinally polarized in the direction of $\vec{K}$) and the nucleon (respectively). In the laboratory frame and neglecting the nucleon mass in Eq. 1, the unpolarized cross-section $\frac{d^2\sigma^{unp}}{d\Omega dE'}$ is written in terms of the form factors W_1 and W_2 [13]

$$\frac{d^2\sigma^{unp}}{d\Omega dE'} = \frac{4\alpha^2 E'^2}{Q^4}\left[2W_1 \sin^2\frac{\theta}{2} + W_2 \cos^2\frac{\theta}{2}\right] \tag{7}$$

where θ is the scattering angle of the lepton in the lab frame.

The difference of cross-sections with opposite lepton spins is given by [13]

$$\begin{aligned}\frac{d^2\sigma^{\rightarrow,\mathbf{S}}}{d\Omega dE'} \quad - \quad & \frac{d^2\sigma^{\leftarrow,\mathbf{S}}}{d\Omega dE'} = -\frac{4\alpha^2}{Q^2}\frac{E'}{E} \\ & \times \quad ([E\cos\alpha + E'\cos\Theta]MG_1 + 2EE'[\cos\Theta - \cos\alpha]G_2)\end{aligned} \tag{8}$$

where α is the polar angle of the nucleon spin direction, i.e. the angle between $\vec{k}$ and $\vec{\mathbf{S}}$, Φ is the azimuthal angle between the $(\vec{k}, \vec{k'})$ scattering plane and the $(\vec{k}, \vec{\mathbf{S}})$ polarization plane, and Θ is the angle between $\vec{k'}$ and $\vec{\mathbf{S}}$ with

$$\cos\Theta = \sin\theta\ \sin\alpha\ \cos\Phi + \cos\theta\ \cos\alpha. \tag{9}$$

The functions W_1, W_2, G_1 and G_2 provide precise characterizations of the structure of the nucleons. The functions W_1 and W_2 provide information on the unpolarized electromagnetic structure of the partons within the nucleon. Their determination

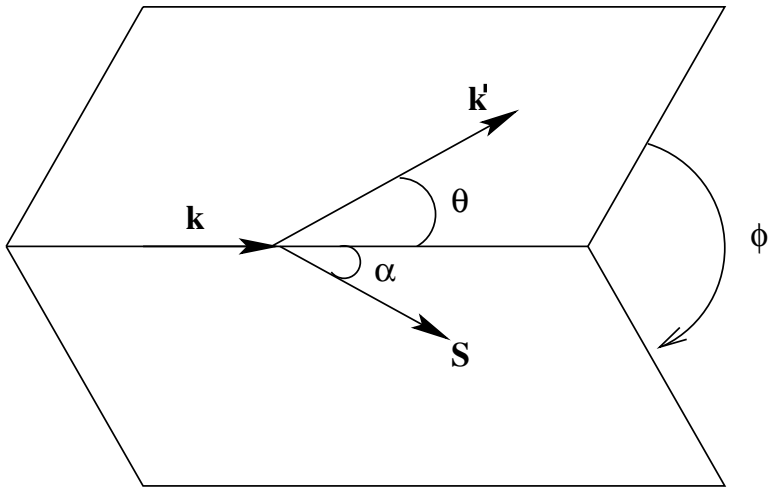

Figure 2: 3-D view of the electron scattering plane with respect to the nucleon spin plane. **S** indicates the nucleon spin.

has played an important role in the understanding of the quark and gluon sub-structure of the nucleon. The functions G_1 and G_2 provide information on the spin structure of the nucleon, which is the subject of this thesis. For convenience, new structure functions F_1, F_2, g_1 and g_2 are defined in terms of the functions W_1, W_2, G_1 and G_2

$$F_1(x, Q^2) = MW_1(\nu, Q^2) \tag{10}$$

$$F_2(x, Q^2) = \nu W_2(\nu, Q^2) \tag{11}$$

$$g_1(x, Q^2) = M^2 \nu G_1(\nu, Q^2) \tag{12}$$

$$g_2(x, Q^2) = M^2 \nu^2 G_2(\nu, Q^2) \tag{13}$$

where x and Q^2 are more relevant quantities for measuring sub-structure. In leading order in $\alpha(Q^2)$, F_1 and F_2 can be related to the spin averaged quark distributions. In the Quark Parton Model which will be discussed further in Sec. 2.1, g_1 is related

in leading order to the difference in the spin distribution functions. In PQCD, g_1 is also sensitive to the polarized gluon distribution through higher order terms. An equivalent simple picture for g_2 does not exist.

It is useful to mention here the "scaling" hypothesis put forward by J. D. Bjorken in 1969 [14], which states that in the deep inelastic region, defined by $Q^2 >> M^2$ and $W^2 >> M^2$, where W^2 is the invariant mass, the structure functions depend only on the scaling variable $x = \frac{Q^2}{2M\nu}$. In the scaling limit (ν,$Q^2 \rightarrow \infty$, and ν/Q^2 constant), x is the fraction of the total nucleon momentum carried by the struck quark and we have

$$\begin{aligned} F_1(x, Q^2) &= F_1(x) \\ F_2(x, Q^2) &= F_2(x) \\ g_1(x, Q^2) &= g_1(x) \\ g_2(x, Q^2) &= g_2(x). \end{aligned} \tag{14}$$

To experimentally extract the structure functions, it is preferable to measure an asymmetry instead of the difference in cross-sections since this difference is very small compared to the large uncertainty of the cross-sections. Measuring an asymmetry reduces the sensitivity to the uncertainties. The measured asymmetry is expressed as

$$A_{meas} = \frac{d\sigma^{\rightarrow,S} - d\sigma^{\leftarrow,S}}{d\sigma^{\rightarrow,S} + d\sigma^{\leftarrow,S}} \tag{15}$$

where $d\sigma$ is short for $d^2\sigma/d\Omega dE'$. We can now relate the measured asymmetry to the structure functions using Eqs. 7 and 9 for the denominator and numerator of

Eq. 15 to obtain an expression for g_2

$$g_2 = \frac{yF_1}{2E'(\cos(\Theta) - \cos(\alpha))}\left[A_{meas}\nu\frac{(1+\epsilon R)}{1-\epsilon} - \frac{g_1}{F_1}(E\cos(\alpha) + E'\cos(\Theta))\right] \quad (16)$$

where we make use of additional kinematic variables defined in Table 2. Equation 16 is the formula used in the final analysis as described in Sec. 4.7. The first term inside the brackets in Eq. 16 is the dominant term. In addition, g_1/F_1 is approximately independent of Q^2.

For E155X, we had $\alpha = 92.4^\circ$ rather than the desired $\alpha = 90^\circ$ when measuring g_2 (this will be discussed further in Sec. 4.7). It should be noted that for particular values of α, for example $\alpha = 0$ and $\alpha = \frac{\pi}{2}$, one obtains measurements for the parallel, $A_\parallel$, and perpendicular, $A_\perp$, asymmetries (respectively). As can be seen in Eq. 17 and Eq. 18, g_1 is dominated by $A_\parallel$ because $A_\perp$ is suppressed by a factor $\tan(\theta/2)$ which is small when θ is small, and g_2 is dominated by $A_\perp$ because $A_\parallel$ is suppressed by a factor $\sin\theta$, also small when θ is small.

$$g_1(x,Q^2) = \frac{F_1(x,Q^2)}{D'}\left[A_\parallel(x,Q^2) + \tan\left(\frac{\theta}{2}\right)A_\perp(x,Q^2)\right] \quad (17)$$

$$g_2(x,Q^2) = \frac{F_1(x,Q^2)}{D'}\frac{y}{2\sin(\theta)} \times \left[\frac{[E+E'\cos(\theta)]}{E'}A_\perp(x,Q^2) - \sin(\theta)A_\parallel(x,Q^2)\right] \quad (18)$$

y	νE
ϵ	$1/[1+2(1+\nu^2/\mathrm{Q}^2)\tan^2(\theta/2)]$
γ^2	Q^2/ν^2
D$'$	$(1-\epsilon)(2-y)/y[1+\epsilon R(x,Q^2)]$

Table 2: Additional kinematic variables.

1.2 Virtual Photon - Nucleon Asymmtries

So far we have seen an analysis for probing the nucleon in terms of electron-nucleon cross-sections. However, deep inelastic scattering actually occurs with the exchange of a virtual photon by the lepton and nucleon. The structure functions defined in Sec. 1.1, can also be expressed in terms of the photon absorption cross-sections.

Two virtual photon-nucleon asymmetries A_1 and A_2 are defined as follows

$$A_1 = \frac{\sigma^T_{1/2} - \sigma^T_{3/2}}{\sigma^T_{1/2} + \sigma^T_{3/2}} \tag{19}$$

$$A_2 = \frac{\sigma^{TL}_{1/2}}{\sigma^T} \tag{20}$$

where $\sigma^T_{1/2}$ and $\sigma^T_{3/2}$ are the transverse virtual photon-nucleon absorption cross-sections when the projection of the total angular momentum of the photon-nucleon system along the incident lepton direction is $(1-1/2) = 1/2$ (photon, nucleon spins anti-aligned) and $(1+1/2) = 3/2$ (photon, nucleon spins aligned) respectively. The total transverse absorption cross-section is equal to $\sigma^T = \frac{1}{2}\left(\sigma^T_{1/2} + \sigma^T_{3/2}\right)$. The term $\sigma^{TL}_{1/2}$ arises from the interference between longitudinal and transverse amplitudes which can be positive or negative. There is an additional cross-section $\sigma^L_{1/2}$ related to the longitudinal virtual photon absorption which appears later. We will also use

the ratio of longitudinal to transverse absorption cross-sections $R(x,Q^2) = \frac{\sigma_{1/2}^L}{\sigma^T}$. These absorption cross-sections are related to the previously defined kinematics and structure functions as follows

$$\sigma_{1/2}^T = \frac{4\pi^2\alpha}{K}\left(W_1 + M\nu G_1 - Q^2\right) \tag{21}$$

$$\sigma_{3/2}^T = \frac{4\pi^2\alpha}{K}\left(W_1 - M\nu G_1 - Q^2\right) \tag{22}$$

$$\sigma_{1/2}^L = \frac{4\pi^2\alpha}{K}W_2\left(1 + \frac{\nu^2}{Q^2}\right) - W_1 \tag{23}$$

$$\sigma_{1/2}^{TL} = \frac{4\pi^2\alpha}{K}\sqrt{(}Q^2)\left(MG_1 + \nu G_2\right) \tag{24}$$

where $K = \nu - Q^2/2M$. The polarized spin structure functions are related to the virtual photon-nucleon asymmetries as follows

$$g_1 = \frac{F_2}{2x(1+R)}(A_1 + \gamma A_2) \tag{25}$$

$$g_2 = \frac{F_2}{2x(1+R)}(A_2/\gamma + A_1) \tag{26}$$

Combining Eqs. 16 and 25, we obtain the following expression for A_2 in terms of the measured asymmetry, A_{meas}

$$A_2 = \frac{y(1+\epsilon R)\gamma\nu A_{meas}}{2E'(\cos(\Theta) - \cos(\alpha))(1-\epsilon)} + \gamma\left[1 - \frac{y(E\cos(\alpha) + E'\cos(\Theta))}{2E'(\cos(\Theta) - \cos(\alpha))}\right]\frac{g_1}{F_1} \tag{27}$$

The dominant term in the expression of A_2 is the term containing A_{meas}. Since the virtual photon carries only part of the polarization of the scattered electron, by measuring A_2 we are considering an idealized case without the depolarization. Furthermore, the determination of A_2 provides an additional comparison with theory as will be seen in Sec. 2.6.

CHAPTER 2

Theoretical background for g_2 and A_2

In addition to the general theoretical framework discussed in Chapter 1, there exist several specific theoretical predictions for g_2 and A_2 that will be tested by the E155X data. Calculations for g_2 have been performed in the Quark Parton Model, the Bag models, and the Chiral Soliton model. Comparing the experimentally measured results for g_2 to theoretical predictions can help in further understanding this structure function and the dynamics of the nucleon. Two predictions for A_2, the positivity limit and the Soffer limit are also discussed.

2.1 Quark Parton Model

In the simplest version of the Quark Parton Model (QPM), the Naive Quark Parton Model (NQPM), the nucleon is considered to be made of collinear, free constituents, each carrying a fraction x of the nucleon four momentum, $p^\mu = xP^\mu$, and of mass $m_q = xM$ [13]. In the NQPM, DIS is described as the incoherent sum of all interactions between the incoming lepton and the constituent quarks. The spin structure function g_2 measures the interactions between quarks inside the nucleons. Thus, since the NQPM assumes that the quarks are free in the nucleon,

the prediction for g_2 is

$$g_2(x) \equiv 0 \tag{1}$$

Non-zero values for g_2 can be obtained by allowing the quarks to have an intrinsic Fermi motion inside the nucleon, $p^\mu = (e_q, p_x, p_y, xP_z)$ (in a nucleon moving along the $\hat{z}$ axis), in the infinite momentum frame ($|P_z| \to \infty$). At leading order in $\frac{M}{P_z}$ the prediction is

$$g_2(x) = \frac{1}{2}\Sigma e_q^2 \left(\frac{m_q}{xM} - 1\right) \Delta q(x) \tag{2}$$

where m_q is now the effective mass of the quarks, e_q is the charge of the quarks and $\Delta q(x)$ is the difference between the number density of quarks with same helicity as the nucleon and those with opposite helicity. If the intrinsic transverse momentum of the quarks is neglected, then $m_q = xM$, and the result from Eq. 1 is recovered.

The introduction of intrinsic transverse momentum gives rise to non-zero values for g_2. However, the values obtained are extremely sensitive to the effective quark mass. Therefore, reliable calculations of $g_2(x)$ cannot be expected in the QPM.

2.2 Operator Product Expansion

We have seen that the QPM cannot give a reliable prediction for g_2 due to terms that are sensitive to the quark mass. In 1962, Wilson presented a more accurate description of g_2 using the "Operator Product Expansion" (OPE) technique [15]. In this technique, g_2 can be approximated by expanding the matrix element for the forward virtual Compton scattering process in a series of terms proportional

to $1/\sqrt{Q^2}$. The following discussion will briefly illustrate this technique.

The hadronic tensor $W^{\mu\nu}$ is related to the matrix element of a product of current operators [16]:

$$W^{\mu\nu}(q^2,\nu) = \frac{1}{4\pi}\int d^4z e^{-iq.z} < P|J^{\mu}(0)J^{\nu}(z)|P > \tag{3}$$

where P is momentum and J^{μ} and J^{ν} are electromagnetic currents. Using translational invariance this can be written

$$W^{\mu\nu} = \frac{1}{4\pi}\int d^4z e^{-iq.z} < P|J^{\mu}(\frac{1}{2}z)J^{\nu}(-\frac{1}{2}z)|P > \tag{4}$$

Products such as the product of electromagnetic currents in Eq. 4 are singular as $z^2 \to 0$, and Wilson's result is that these singularities can be isolated in ordinary, i.e. non-operator, functions, multiplied by non-singular operators:

$$J\left(\frac{1}{2}z\right)J\left(-\frac{1}{2}z\right) = C_J^N(z^2)z^{\mu_1}z^{\mu_2}...z^{\mu_N}O^{J,N}_{\mu_1...\mu_N}(0) \tag{5}$$

The operators $O^{J,N}_{\mu_1...\mu_N}$ are non-singular and are evaluated at $x = \frac{1}{2}[\frac{1}{2}z + \left(-\frac{1}{2}z\right)] = 0$. These operators are referred to as "spin N" operators. The coefficient functions $C_J^N(z^2)$ are also singular as $z^2 \to 0$. If $d_{J,N}$ is the dimension of the operator $O^{J,N}$, then $\tau_{J,N} = d_{J,N} - N$ is called the twist of the operator $O^{J,N}$. The coefficients $C_J^N(z^2)$ are are expected to behave as follows

$$C_J^N(z^2) \to \left(\frac{1}{z^2}\right)^{\frac{1}{2}(2d_J - \tau_{J,N})} \qquad as \;\; z^2 \to 0 \tag{6}$$

where d_J is the dimension of J. From Eq. 6, it can be noted that the smaller $\tau_{J,N}$ is, the more singular $C_J^N(z^2)$ will be. The lowest twist operators will therefore control the dominant terms of the expansion of the hadronic tensor as $z^2 \to 0$.

So far we have seen that with the OPE technique, the hadronic tensor can be written as a series of terms based on their degree of singularity. The Fourier transform of the $C_J^N(z^2)$ coefficients can then be related to the N^{th} moment of the structure functions $W_j(\nu, q^2)$. This leads to the following set of sum rules:

$$\int_0^1 x^N g_1(x, Q^2) dx = \frac{1}{2} a_N \quad N = 0, 2, 4... \tag{7}$$

$$\int_0^1 x^N g_2(x, Q^2) dx = \frac{1}{2} \frac{N}{N+1} (d_N - a_N) \quad N = 2, 4... \tag{8}$$

The a_N and d_N coefficients are the matrix elements of the twist-2 and twist-3 operators respectively, in the OPE. The twist-3 term in g_2 is related to quark-gluon interactions. The twist terms with $\tau > 3$ are predicted to be negligible [17]. There exist other conventions for d_N differing by a factor of 2 [18].

2.2.1 The Wandzura-Wilckek Relation

If Eqs. 7 and 8 are solved by assuming that the twist-3 term is negligible, one obtains an expression for the twist-2 part of g_2. This calculation was first performed by Wandzura and Wilczek [19], and the result was the following prediction for g_2:

$$g_2^{WW}(x, Q^2) = -g_1(x, Q^2) + \int_x^1 \frac{dy}{y} g_1(y, Q^2). \tag{9}$$

2.2.2 A Complete Description of g_2

At finite Q^2, the twist-3 term should not be neglected. Moreover, the additional twist-2 term which is due to the quark's spin distribution transverse to the nucleon momentum should also be taken into account. The correct expression at

finite Q^2 up to twist-3 is then

$$g_2(x,Q^2) = g_2^{WW}(x,Q^2) - \int_x^1 \frac{\partial}{\partial y}\Big(\frac{m}{M}h_T(y,Q^2) + \xi(y,Q^2)\Big)\frac{dy}{y} \tag{10}$$

where m is the effective quark mass, M is the nucleon mass, and h_T is a twist-2 term which describes the quark transverse spin distribution. The h_T term is sometimes referred to as transversity. The magnitude of this term is still not well known. Equation 10 is often written

$$g_2(x,Q^2) = g_2^{WW}(x,Q^2) + \overline{g_2}(x,Q^2) \tag{11}$$

where

$$\overline{g_2}(x,Q^2) = -\int_x^1 \frac{\partial}{\partial y}\Big(\frac{m}{M}h_T(y,Q^2) + \xi(y,Q^2)\Big)\frac{dy}{y} \tag{12}$$

The contribution of the h_T term is expected to be small because of the small value of the ratio of the quark mass to the nucleon mass, $\frac{m}{M}$ [20]. Therefore, any deviations in the measured g_2 from g_2^{WW} will arise primarily from the twist-3 term in g_2, which as mentioned previously, is related to the quark-gluon interactions. The structure function g_2 has been the subject of considerable interest because of this twist-3 term contribution which provides a tool to study nucleon dynamics.

2.2.3 Extraction of the Twist-3 Matrix Elements

From the sum rules in Eqs. 7 and 8, we obtain the following expression for the twist-3 matrix elements d_N:

$$d_N = 4\int_0^1 x^N[g_1(x) + \frac{N+1}{N}g_2(x)] \quad N = 2,4... \tag{13}$$

An experimental measurement of the twist-3 matrix element d_2 obtained for $N = 2$ can be compared to theoretical predictions. Calculations for d_2 exist in the bag model and the chiral model. These models are described in later sections. However, the two methods that are usually used to provide calculations of the OPE matrix elements are Lattice QCD and QCD sum rules calculations. (See reference [21] for a summarized explanation of these latter two calculations).

2.3 Sum Rules

2.3.1 Burkhardt-Cottingham Sum Rule

The Burkhardt-Cottingham (BC) sum rule [22] for g_2 at large Q^2 does not follow from OPE since $N = 0$ is not included in the expansion in Eq. 8, but complements the OPE sum rules. The BC sum rule was derived from virtual Compton scattering dispersion relations, and is expressed as follows

$$\int_0^1 g_2(x)dx = 0. \tag{14}$$

The BC sum rule has been shown to be correct to order α_s for a gluon target [23] and quark target [24].

2.3.2 Efremov-Leader-Teryaev Sum Rule

Just as for the OPE, it can be argued that the hadronic matrix elements in the hadronic tensor should be small, leading to approximate sum rules for the moments of the valence parts of g_1 and g_2. For the case $N = 2$, it has been proven that the hadronic matrix element vanishes, which leads to the exact Efremov-Leader-Teryaev

(ELT) sum rule [25] written as follows

$$\int_0^1 x \left(g_1^V(x) + g_2^V(x)\right) dx = 0 \tag{15}$$

where g_1^V and g_2^V are the net structure function contribution due to valence quarks. Assuming that the sea quarks are the same in protons and neutrons, then the ELT sum rule becomes

$$\int_0^1 x \left(g_1^p(x) + 2g_2^p(x) - g_1^n(x) - 2g_2^p(x)\right) dx = 0. \tag{16}$$

While the ELT sum rule relies on the assumption of a symmetric sea, it does not rely on neglecting twist-3 contributions. The ELT sum rule can be used to obtain information about g_2 and provides a further test of QCD up to the limits of the assumptions.

2.4 Bag Models

As discussed in the previous section, both twist-2 and twist-3 operators make contributions to the structure function g_2. The twist-3 operators are related to the quark-gluon interactions and quark masses. The function g_2 has been evaluated in the bag model to estimate the importance of the twist-3 operator. The bag models have had intuitive utility in the past, such as providing an explanation for the EMC effect [26]. Bag models are also a useful tool for calculating structure functions because they incorporate the "confinement property" in a simple manner. The bag boundary simulates the confinement effects which arise from quark-gluon effects. The bag model calculation is not expected to provide a quantitatively accurate

prediction for $\overline{g_2}$. Instead, it is viewed as a toy model or cartoon, lacking Regge behavior and the proper $x \to 1$ limit, but giving a rough estimate of the size of $\overline{g_2}$ [17]. There exist several bag models which differ by their definition of the boundary conditions, the number and type of fields contained in the bag, or the calculation technique used to extract the results. The results of the g_2 measurement from this experiment will be compared to two different bag model calculations, the modified MIT model by M. Stratmann [30], and the Center of Mass model by X. Song [33].

2.4.1 The MIT Bag Model

In the bag model, the hadron is considered to be an extended region of space (the bag) containing quark fields. A universal pressure, B, confines the quarks to the bag. The quarks are only weakly coupled to one another (by vector gluons) inside the bag. Such a model of a nulceon allows a parton interpretation and exhibits Bjorken scaling. In 1975, R. Jaffe presented a calculation for deep-inelastic structure functions in the bag theory known as the MIT model [27]. The starting point of the MIT bag model calculation of the structure function g_2 is the insertion of the MIT bag wave functions [27], which are solutions to the equations of motion of the quarks and gluons inside the bag, into the hadronic tensor. The MIT bag model presented some disadvantages such as the constant value obtained for the ratio of the u and d valence quark distributions ($u_v(x)/d_v(x)$), in disagreement with the experimental result of F_2^n/F_2^p. A modified version of the MIT bag model (the SST bag model) was proposed by Schreiber et al. in 1991 [28] which adopted improvements to the

MIT bag model. In the SST bag model, a different behavior was obtained for $u_v(x)$ and $d_v(x)$ by introducing some phenomenological extensions such as the "one-gluon-exchange" [29] which can be applied to the remaining diquark not participating in the hard process. In 1993, Stratmann proposed yet another modified version of the MIT bag model known as the MOD bag model [30]. An important difference is that unlike the SST bag model, the MOD bag model, satisfies the Burkhardt-Cottingham (BC) sum rule [22]. A violation of the BC sum rule would imply a non-conventional behavior of g_2. However, if the BC sum rule is found to be incorrect, then the MOD bag model can no longer be considered an acceptable model.

The limitations of the MIT bag model calculation come from the difficulty of fixing the introduced model parameters which are not currently calculable, i.e. how to relate the model to experimental data. The bag model parameters are determined via a fitting procedure which uses evolution equations to relate the calculated g_2 in the bag model to experimentally relevant Q^2 regions. The evolutions of g_2^{WW} and $\overline{g_2}$ are treated separately because they are governed by different evolution equations. The evolution of g_2^{WW} is completely determined through the well-known evolution kernels of g_1 [31]. The evolution of $\overline{g_2}$ is not yet well known because the number of independent twist-3 operators increases with the moment N under consideration. A. Ali et al. [32] determined a simple Q^2 evolution equation for $\overline{g_2}$ which was used in the MOD bag model. It is difficult to know how well these results can be trusted because possibly important (especially at low x) singlet contributions to $\overline{g_2}$ are currently unknown.

2.4.2 The CM Bag Model

Another model, known as the CM (center-of-mass) bag model, was used by Song [33] to provide predictions for the spin structure functions. The CM bag model re-defines the parameters of the bag in terms of its center of mass. In the CM bag model the antisymmetric part of the hadronic tensor (given in Eq. 3) is written

$$W^A_{\mu\nu} = i\epsilon_{\mu\nu\sigma\rho}(q^\rho/\nu)I^\sigma(x, Q^2) \tag{17}$$

where $I^\sigma(x, Q^2)$ depends on the model of the nucleon and the approximations used in the calculations. The basic assumptions of the CM bag model are [33]:

- The nucleon electromagnetic current, J_μ, can be approximately expressed by the incoherent sum of single quark electromagnetic currents. This assumes the impulse approximation. The current includes contributions both from the struck quark and the spectator quarks.

- The nucleon consists of three valence quarks in their S-wave state; higher excited states which include gluons and sea quarks are neglected.

- The scalar u-d quark pair is assumed to occupy a smaller spatial size than the vector u-u and d-d quark pairs in the nucleon.

- The effect of quark confinement due to non-pertubative quark-gluon and gluon-gluon interactions is described in terms of bound state quark spatial wave functions.

Several parameters were used in the CM bag calculation such as the bag radius ($R = 5$ GeV^{-1}), the maximum momentum of quarks inside the nucleon ($|p_{max}| = 0.6$ GeV/c), and the SU(3) symmetry breaking parameter ($\zeta = 0.85$). The results from the CM bag calculation were evolved to higher Q^2 from the renormalization scale $Q_o^2 = 0.81$ (GeV/c)^2 to compare to experimental data. The BC sum rule holds true in the CM bag model. However, the ELT sum rule is violated.

2.5 Chiral Soliton Model

The spin structure g_2 has also been computed by H. Weigel [34] in the Chiral Soliton Model (CSM), also known as the Nambu-Jona-Lasinio chiral soliton model (NJL) [35]. A chiral transformation is a symmetry of the non-mass term in the Dirac Lagrangian. The CSM is a dynamical theory in which nucleons and mesons are derived in a unified way from a fundamental spinor field. The CSM has the characteristic features of a compound-particle model in which baryons are described as a group of mesons in the CSM.

The scheme of the CSM was motivated by analogy between the properties of Dirac particles and the quasi-particle excitations that appear in the theory of superconductivity [36]. The characteristic feature of the theory of superconductivity is that it produces an energy gap between the ground state and the excited state of a superconductor, due to electron interactions. By analogy, the mass of a Dirac particle in the CSM is assumed to be due to some interaction between massless fermions. A quasi-particle in a superconductor is a mixture of bare electrons with

opposite electrical charges. Correspondingly in the CSM a massive Dirac particle is a mixture of bare fermions with opposite chiralities, but with the same charge or fermion number. In a refined theory of superconductivity, collective excitations of quasi-electric pairs appear in addition to the individual quasi-particle excitations. With this observation, if a Dirac particle is considered to behave as a quasi-particle, then collective excitations of bound quasi-particle pairs must also exist. This is of course only an approximate description of an entire system where chirality is conserved. Taking chirality conservation implications into account, it was shown that the collective state must be a pseudo-scalar. A pion fits this characteristic of a collective state, thus leading to description of nucleons as groups of pions in the CSM. The Chiral model prediction for g_2, along with the other predictions discussed previously, are plotted in Fig. 3.

2.6 A_2 Positivity Limit

In addition to the g_2 predictions discussed above, there is a positivity limit on A_2 which can also be tested by experimental measurements. Recall that the virtual photon absorption asymmetry in virtual forward Compton scattering is related to the cross-sections σ^{TL} and σ^T by Eq. 20 in Sec. 1.2. The cross-section σ^{TL} represents the case where the incoming transversely polarized photon flips its spin and becomes longitudinally polarized. σ^T represents the case where the incoming and outgoing photon are both transversely polarized. σ^{TL} and σ^T can be expressed in terms of

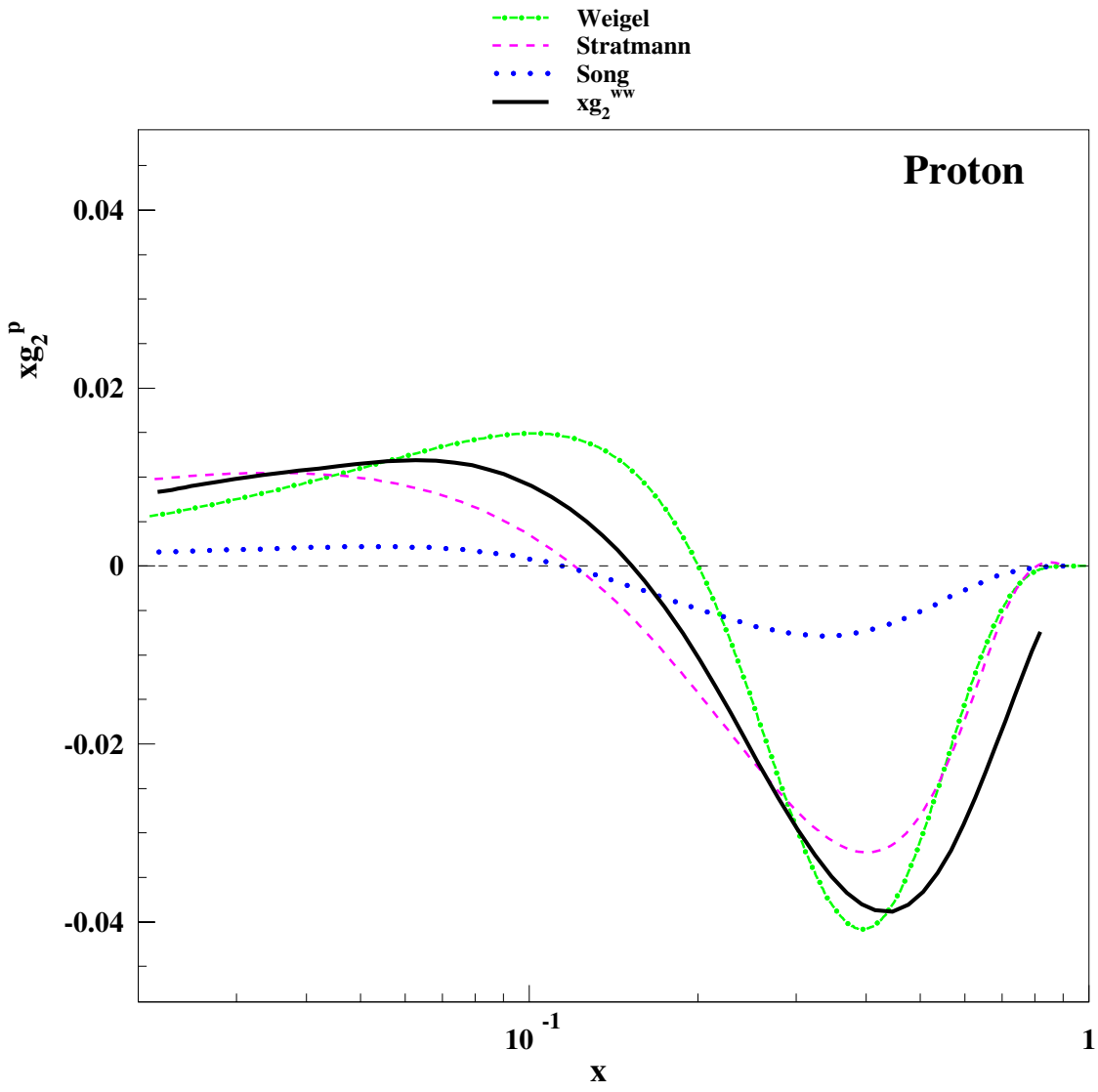

Figure 3: Theoretical models for g_2 plotted versus x for the proton at $Q^2 = 5$ GeV^2. Weigel's chiral soliton model calculation is shown as the dot-dashed curve, Stratmann's modified MIT model calculation is shown in the dashed curve. The dotted curve represents Song's CM bag model calculation, and the solid curve is xg_2^{WW} using the E155 fit to g_1.

two amplitudes A_T and A_L. A_2 can then be written:

$$A_2 = \frac{| < A_T | A_L > |^2}{| < A_T | A_T > |^2} e^{i\Phi} \tag{18}$$

where $e^{i\Phi}$ is the phase difference between the cross-sections. Using the Schwartz inequality we obtain

$$|A_2| \leq \frac{| < A_T | A_T > || < A_L | A_L > |}{| < A_T | A_T > |^2} = \frac{| < A_L | A_L > |}{| < A_T | A_T > |} \tag{19}$$

The last term of Eq. 19 can be recognized as the square root of the quantity $R(x, Q^2)$ defined in Sec. 1.2. The positivity limit for A_2 is then:

$$|A_2| \leq \sqrt{R(x, Q^2)} \tag{20}$$

The bound shown in Eq. 20 represents a non-trivial positivity condition on the photon-nucleon helicity amplitudes. If photons are substituted for gluons, the similar bound holds for the different matrix elements for longitudinal gluons in a nucleon. This bound was rederived by Soffer [37] in line with the positivity bound in the quark case. Soffer obtained the following stronger bound

$$|A_2| \leq \sqrt{R(x, Q^2)(1 + A_1)/2} \tag{21}$$

which is known as the Soffer limit.

CHAPTER 3

Experimental Setup

Experiment E155X used polarized deep inelastic scattering produced by scattering polarized electrons off a polarized hadron target to study the spin structure function g_2. To obtain the physics result, the scattered electrons at different kinematics needed to be detected and counted. Magnetic spectrometers were used to detect the scattered electrons. The design choices of the spectrometers were motivated by the need to count electrons at high rates by making tracks out of detector hits, while unambiguously separating electrons from the backgrounds of charged hadrons and low energy neutral particles by carefully imposing certain cuts. The magnetic fields and geometry of the spectrometers must be well known to determine the kinematics of the detected particles using a good computer model. This chapter will describe the different pieces of equipment used.

3.1 Electron Beam

The electron beam at SLAC is produced by shining circularly polarized laser light on a strained GaAs cathode [38]. Longitudinally polarized electrons are emitted from the cathode and accelerated in the linear accelerator (linac). The linac uses a series of copper microwave resonant cavities, where the microwave sources are known

as klystrons, to accelerate the electrons. The energy of the electrons can reach up to 50 GeV. For fixed target experiments, at the end of the two-mile-long linac, the beam is deflected into the End Station A (ESA) where the target and spectrometers are located. The beam is then stopped in the beam dump. The SLAC Main Control Center (MCC) steer, tune and continuously monitor the beam.

Although the energy of the beam could reach 50 GeV, during E155X the accelerator delivered beams of energies of about 29 and 32 GeV. Higher beam energies enable a deeper probing into the nucleus which is the goal of DIS experiments. However, the chosen energies were a balance between the desire to probe as deep as possible into the nucleus, and maximizing the collection of electron events with the lowest possible background, which is mainly due to pions. Indeed, at lower beam energies, the DIS-cross section is increased, while the pion production is reduced.

When the linac is delivering lower beam energies, the klystron timing can be used to lengthen the beam pulses. The advantage of having a longer beam pulse in this type of experiment is that hits are more spread out in time, reducing the overlap of hits due to the dead time of the detectors.

Two different beam energies were used for E155X. Initially data were collected at a beam energy of 29.1 GeV. However, the background rate in the detectors was too high because the chicane magnets were not providing enough bending power for the electrons, allowing them to "scrape" the inside of the beam pipe past 3B4 as seen in Fig. 4. The role of the chicane magnets was to compensate the bending of the electrons in the vertical direction due to the transverse magnetic field. However,

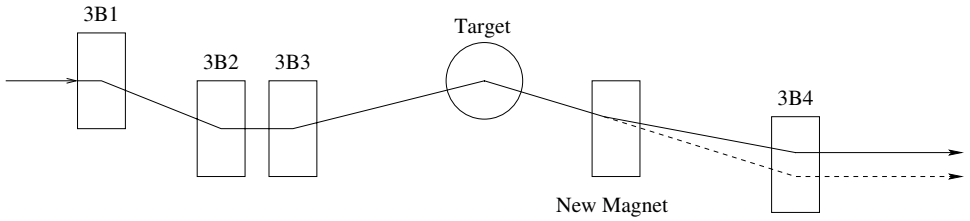

Figure 4: Diagram showing where the "kicker" magnet was added. The dashed line shows the path of the particles before the kicker magnet was added.

since the bending power of the chicane magnets was not sufficient, the beam energy was raised to 32.3 GeV, which reduced this background rate but slightly reduced the number of DIS events collected as well. Roughly halfway through the run, a small magnet was added downstream of the target to provide additional bending (See Fig. 4). The background rates were then low enough in the detectors to return to our initial choice of optimal beam energy, 29.1 GeV. In fact, at this energy, the beam current could be raised compared to 32.2 GeV because the background rate was lower. The current on average was $2.5 * 10^9$ e^-/pulse at 29.1 GeV, and $1.5 * 10^9$ e^-/pulse at 32.3 GeV. The beam pulse length was about 420 ns long.

The helicity of the electrons was determined at the source by controlling the laser light helicity with a pseudo-random 32-bit number generator for every pulse. Different sets of polarization bits provided the helicity information. A comparison between these polarization bits was performed for E155X, and the one with the lowest error rate was used in the final analysis. Reference [39] contains the details of the comparison between these different polarization bits.

The beam conditions were monitored and recorded pulse by pulse during data taking. The energy was measured with a flip coil mounted in a magnet connected

in series with the A-line bend string which is shown in Fig. 5. The beam current was measured with two toroids located at the entrance to the End Station. The beam position was measured using a secondary emission foil array, located about 9 m downstream of the target which consisted of two sets of 48 foils, one aligned vertically and the other horizontally. The position of the beam could be determined to about ± 1 mm. In addition, "spill monitors" were used to look for rapid changes in the beam conditions. The spill monitors were each made out of a scintillator paddle connected to a photomultipier tube (PMT). The signal was monitored in real-time on an oscilloscope during the experiment, and sent to an ADC gated over the entire signal. One of the spill monitors, which we called the "bad spill monitor", was placed at the beam entrance to the End Station, close to the final beam line collimator in the alcove. When particles were detected by the bad spill monitor, this meant that the beam conditions were poor, and this resulted in increased backgrounds in the end station. The "good spill monitor" was located below the target, and measured the scattering rate from the target. The amount of signal detected changed if the beam was missing the target or hitting some thicker part of the target apparatus. In addition, for E155X some of the planes of the front hodoscopes in the 2.75° spectrometer were used in an OR configuration as a second good spill monitor.

The beam polarization was measured using Møller polarimetry [40]. The asymmetry in the cross-sections of positive and negative helicity electrons scattering off polarized electrons in a thin polarized ferromagnetic foil was measured. This measured asymmetry is proportional to the beam polarization, the target foil po-

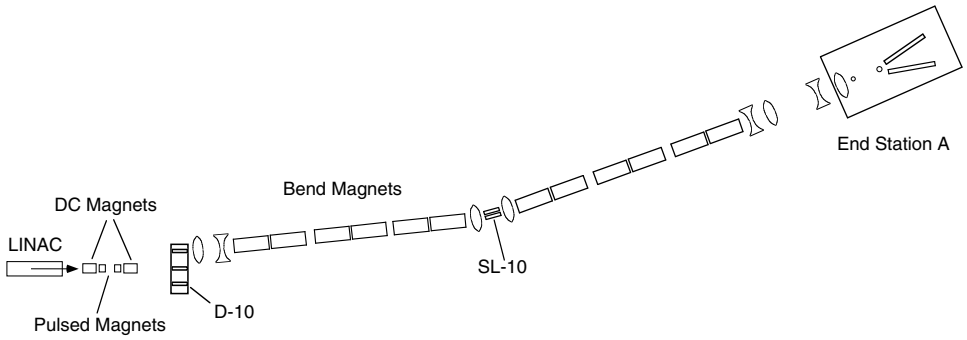

Figure 5: A schematic of the A-line showing the twelve dipole bend magnets.

larization and a theoretical asymmetry. Therefore, when these last two factors are known, the measurement of this experimental Møller asymmetry provides a value for the beam polarization. The results of the Møller analysis are presented in Sec. 4.4.1.

3.2 Polarized Target

In addition to a polarized beam of electrons, the measurement required a target of polarized nuclei. To study the proton spin structure function $g_2(x, Q^2)$ an ammonia, $^{15}NH_3$, target was used. The material was in solid granular form and kept at a temperature of 1° K. A cross section of the target system is shown in Fig. 6. The cooling of the material was provided by a refrigerator, which maintained the material at low temperature and compensated for the heating that came from the beam and the microwaves directed onto the material. The target material was contained in a cylindrical cell 3 cm long with a 2.5 cm diameter attached to a long rod, called the target "insert". Each target insert had three cells for targets. Two of the cells contained the polarized material, and were referred to as the upper and

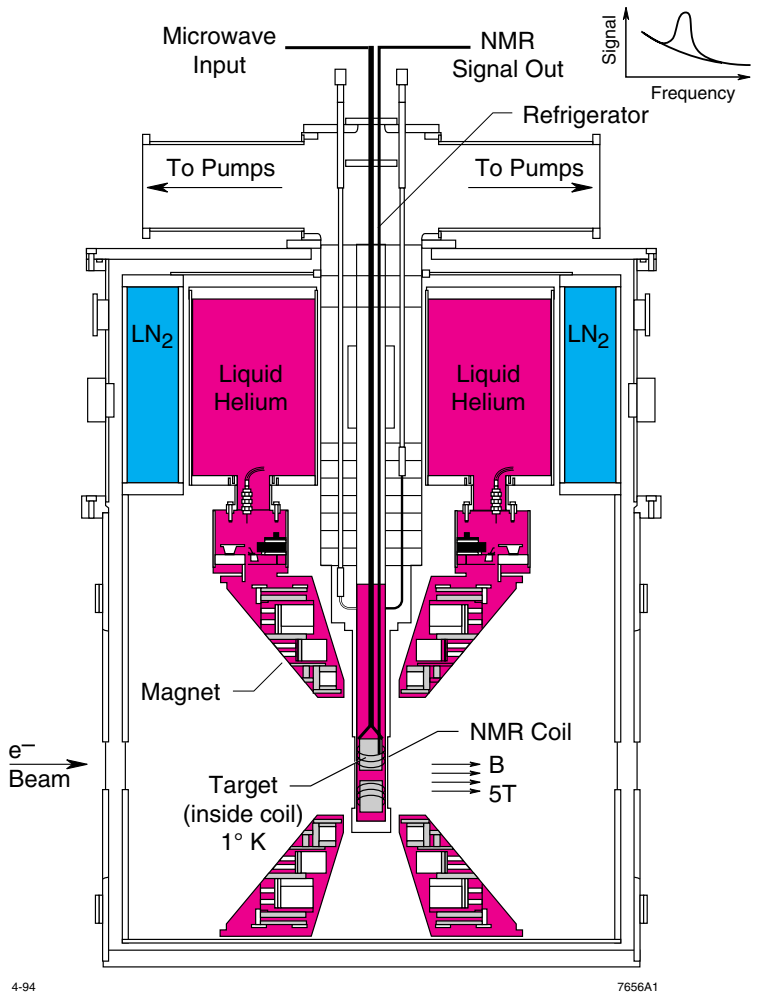

Figure 6: Schematic cross-section of the E155X target system.

lower cells. The third cell contained a solid carbon target which had similar total thickness as the $^{15}NH_3$ target, and was used to determine the dilution factor of the $^{15}NH_3$ target. E155X also took data on a deuteron target using solid LiD_3, and a Be target was used to determine the dilution factor as it provides a closer match to LiD_3 for the radiation length.

Polarization of the nuclei was achieved through the process of Dynamic Nuclear Polarization (DNP) [41]. The material was pre-irradiated to create a dilute

system of paramagnetic centers, i.e. unpaired electrons. For E155X, a warm pre-irradiation, at 80-90°K, was performed at Stanford's 30 MeV SUNSHINE facility. After the material has been doped with paramagnetic defects, the Hamiltonian system of one electron and one nucleon has three terms [42]:

$$H = \mu_e.B + \mu_n.B + H_{ss} \tag{1}$$

The first term in the above equation is a Zeeman term which arises from the magnetic moment of the electron, the second Zeeman term arises from the nucleon's magnetic moment, and the last term represents the spin-spin interaction between the electron and the nucleon.

Ignoring the H_{ss} term, which is small compared to the other two terms, and considering a system with a half-spin nucleon and an electron, there will be four states of the system with different energy levels as seen in Fig. 7. The only allowable transitions according to the dipole selection rules are the transitions W1 and W4. However, if the material is bombarded with photons of frequency $\nu = (\mu_e - \mu_n)B/h$ then the transition W3 will occur. Because the relaxation time of the nucleon spins is much longer than for the electron spins, the W1 transition will follow the W3 transition to the $\left(+\frac{1}{2}, +\frac{1}{2}\right)$ instead of the W4 transition. The consequence of these two transitions is that states with anti-aligned nucleons are converted into states with aligned nucleons. The same technique produces anti-aligned nucleons when microwaves of frequency $\nu = (\mu_e + \mu_n)B/h$ are used to drive the W2 transition, which is then followed by the W1 transition.

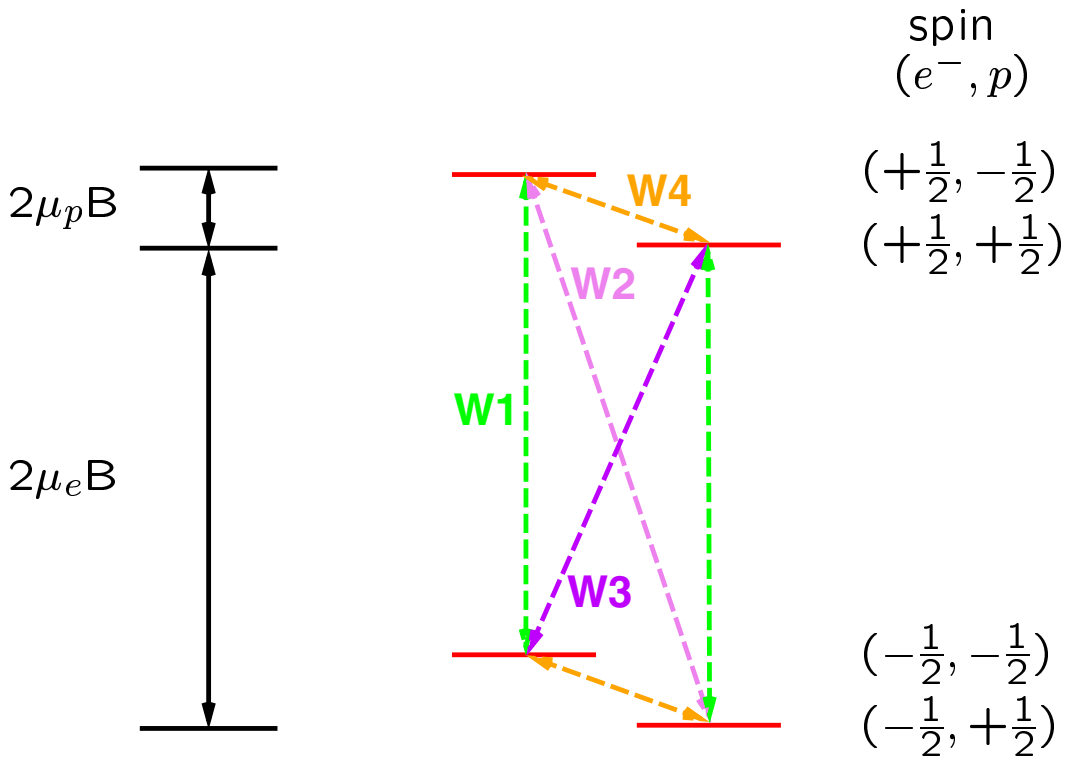

Figure 7: Energy levels of the proton-electron system in a magnetic field.

The protons were polarized by applying microwaves of frequency of about 140 GHz to drive the W3 transition (positive enhancement). To drive the W2 transition (negative enhancement) microwaves with a frequency about 350 MHz higher were applied.

This DNP polarization only occurs near paramagnetic centers, which are sparse. Through a process of spin diffusion, the dipole-dipole interaction between nuclei allows the spin of one nucleon to be transferred to a nucleon close by.

The polarization of the nucleons decays through spin-spin coupling with neighboring paramagnetic centers. Therefore, the presence of too many paramagnetic centers would cause the polarization of the material to decrease. During the

experiment, additional paramagnetic centers were produced in the material by the electron beam, causing the polarization to decrease. When the polarization reached an unacceptably low level, an "anneal" was performed on the material. This consisted of warming the target material to its pre-irradiation temperature (85 K for the ammonia and 185 K for the lithium deuteride). During the anneals, the polarization losses due to radiation damage to the crystal lattice structure, and due to the accumulation of too many paramagnetic centers, was partially recovered. The decay lifetime of the polarization of the material decreased with every anneal. When the polarization could no longer be brought up to an acceptable level after an anneal, the target material was changed.

The polarization of the material was measured using Nuclear Magnetic Resonance (NMR), which measures the net nuclear magnetization of the material [42]. To perform this measurement, a coil, known as the NMR coil, was placed in and around the target material. When an alternating current is passed through this coil, it creates a time varying field perpendicular to the static field from the target magnet, and the magnetic susceptibility of the target material becomes a function of the frequency of the varying field. The magnetic susceptibility can be written as

$$\chi(\omega) = \chi'(\omega) + i\chi''(\omega) \tag{2}$$

where χ' is the dispersive component of the magnetic susceptibility, and χ'' is the absorptive component. The integral over all frequencies of this absorptive component is proportional to the polarization of the material. The absorptive component

is non-zero only in a small region around the Larmor frequency of the target material. Therefore, it suffices to take the integral of the absorptive term, χ'', over a small region spanning the Larmor frequency of the target species to determine its polarization. In addition, the inductance of the NMR coil is a function of this absorptive term, and can be written as

$$L(\omega) = L_o[1 + 4\pi\eta\chi(\omega)] \tag{3}$$

where L_o is the impedance of this coil with the material completely unpolarized, and η is the filling factor which describes the coupling of the coil's field to the material. The impedance of the coil can then be written

$$Z_{coil} = R_{coil} + i\omega L(\omega) \tag{4}$$

which becomes

$$Z_{coil} = [R_{coil} - 4\pi\omega L_o\eta\chi''(\omega)] + i[\omega L_o[1 + 4\pi\eta\chi'(\omega)] \tag{5}$$

Therefore, measuring the impedance of the NMR coil, Z_{coil}, leads to the value of χ'', which in turn leads to the value of the polarization. The method used in E155/E155X to determine the impedance of the NMR coil was to place the NMR inductor in series with a capacitor and a resistor to form a series resonant LRC circuit. The capacitance was chosen such that the resonant frequency of the circuit is the Larmor frequency of the spin species to be measured. More details on the NMR system can be found in Reference [42]. Some of the proportionality constants in the equation for the polarization are very difficult to measure. Instead of measuring

these constants directly, an overall constant of proportionality was measured when the spins of the material were in thermal equilibrium (TE) with the lattice. In this state, the polarization is given by the lattice temperature and the external magnetic field. The measurement of the area of the TE signal was used to calibrate the enhanced polarization values. In E155/E155X the TE calibrations were periodically performed at 5 T and 1.6 K. Typical polarizations for the proton were on the order of 95%. Section 4.4.2 gives the results of the target polarization analysis performed for E155X.

3.3 Spectrometers

The scattered electrons were detected in three different magnetic spectrometers located downstream of the target. These spectrometers were at fixed angles of 2.75°, 5.5° and 10.5° from the beam line. A diagram of the spectrometer layout is shown in Fig. 8. Each spectrometer consisted of a set of magnets for momentum selection followed by three detector systems. These detector systems consisted of threshold Cherenkov gas counters for particle identification, lead glass shower counters for energy measurement and particle identification, and plastic scintillator hodoscopes for tracking and momentum measurement. The detectors were inside shielded huts made of thick concrete blocks to minimize the radiation penetrating the spectrometers.

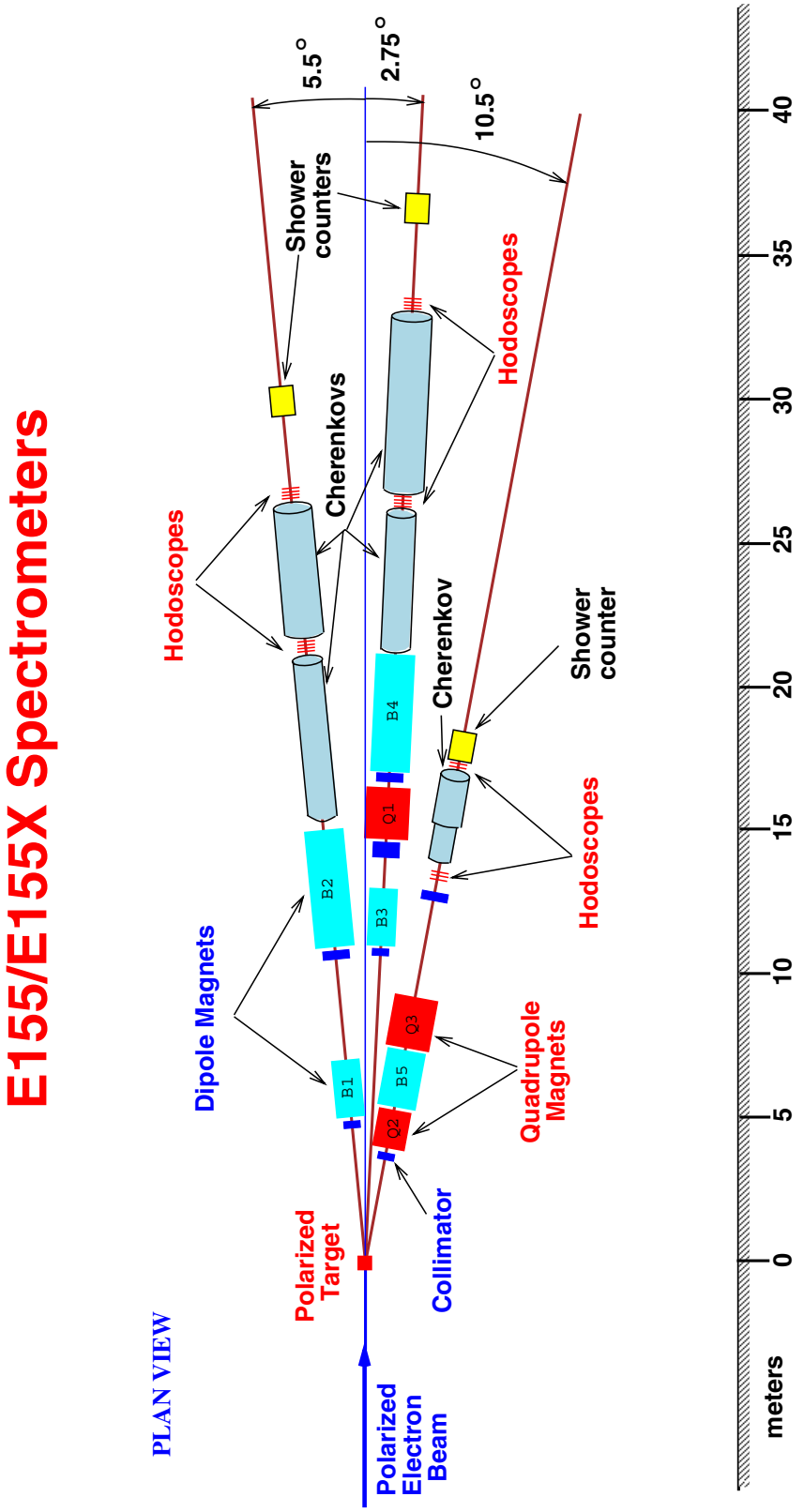

Figure 8: E155X spectrometer layout.

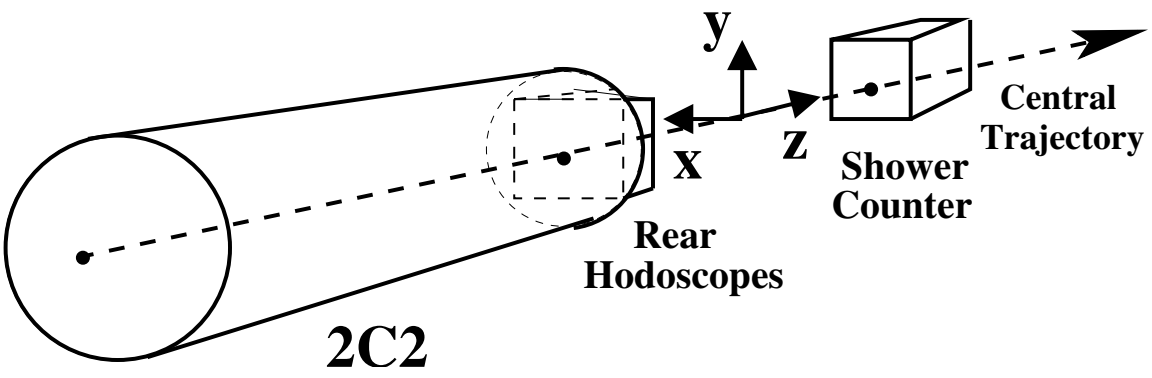

Figure 9: Spectrometer coordinate system relative to 2C2, the rear hodoscopes and the shower counter in the 2.75° spectrometer. This diagram is not drawn to scale.

3.3.1 Spectrometer coordinate system

The "spectrometer" coordinate system is a right handed coordinate system for each spectrometer with the target as origin. The line along the spectrometers is taken as the z axis. The y axis is vertical. The x axis is horizontal and perpendicular to the z direction. The x axis points roughly north in the End Station. Fig. 9 gives a visual description of the spectrometer coordinate system relative to the detectors.

The dipole magnets bend electrons in the vertical direction, thus the (y-z) plane is called the "bend" plane. The angle of a particle path in the bend plane with respect to the y axis is denoted ϕ. The "non-bend" plane (x-z) is horizontal, and a particle path has an angle θ with respect to the x axis in this plane.

Tracks in the spectrometer are related to an imaginary ray called "central trajectory", defined by the optics of the magnetic spectrometers. The trajectory of a particle is defined by specifying its position and momentum vector relative to this central trajectory. The central ray was chosen in such a way that the optics of the spectrometer is approximately symmetric around it. For the analysis a slightly

different coordinate system was used, which was referred to as the "analysis" coordinate system, and will be described in section 4.1.5.

3.3.2 Spectrometer Magnets

Magnets were used to allow particles with only a certain range of momenta to enter the detectors. Collimators placed inside the magnets stopped particles that did not have the correct momentum. A side view of the spectrometers is given in Fig. 10. The 2.75° and 5.5° spectrometers both had two dipoles placed in a "reverse" bend configuration [44], meaning that the fields of the dipoles were in opposite directions. A reverse bend configuration spreads the particles out by momentum, which then makes the collimation very effective. The reverse bend configuration also increases the solid angle acceptance compared to a same bend configuration, because the particles of different momenta are re-focussed, which leads to a wider kinematic coverage of the experiment. This configuration also requires low energy particles, such as the photons originating at the target, to "bounce" at least twice off the collimator or the magnet before entering the spectrometers. The neutral background in the spectrometers is therefore reduced to a tolerable level.

In addition to the two dipoles (B3 and B4), the 2.75° spectrometer had a quadrupole (Q1) magnet between the two dipoles to defocus the particles in the horizontal direction and thus to spread the instantaneous rate of the particles over the shower counter and the hodoscopes. This defocusing also provided a better correlation between the position and momentum of the detected particles. The

5.5° spectrometer did not need such a quadrupole since the instantaneous rate of the particles was not as high as in the 2.75° spectrometer.

The 10.5° spectrometer had one dipole magnet (B5) located between two quadrupole magnets (Q2 and Q3) to maximize particle acceptance. Q2 defocused the trajectories in the vertical direction and focussed them in the horizontal direction, which resulted in an increase of the scattering angle range. Q3 focussed the trajectories in the vertical direction, which provided a correlation between position and momentum and reduced the rate of the background hits.

The spectrometer optics were calibrated by mapping the field of each magnet and using this information as input to a Monte Carlo simulation [45]. Additional calibrations were provided with the test beam experiment T418, in which single electrons at selected energies were directed into the 10.5° and parts of the 2.75°. This allowed for a direct means of calibrating those two spectrometers [46, 47].

The spectrometers covered different kinematic areas as shown in Fig. 11. The 2.75° and 5.5° accepted particles with momentum greater than 9 GeV, and the 10.5° accepted particles with momentum greater than 6 GeV.

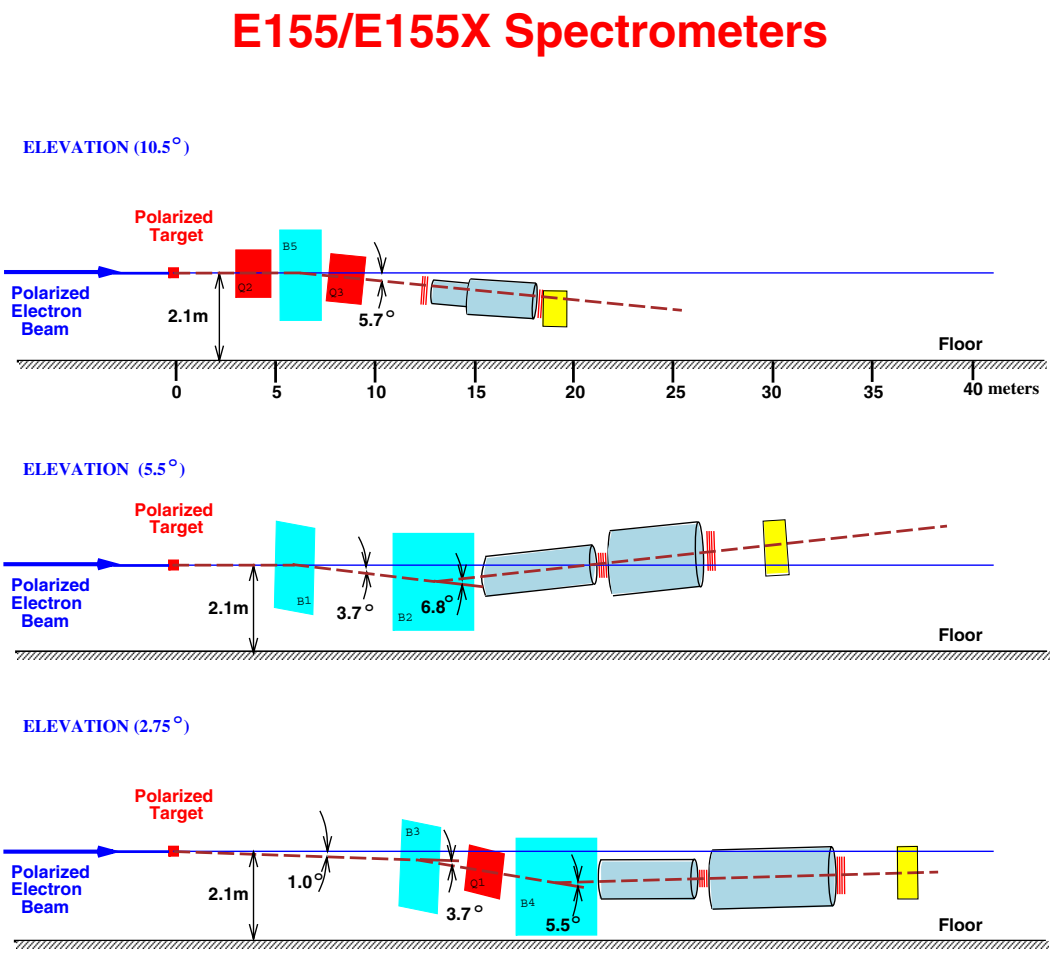

Figure 10: Side view of the E155X spectrometers.

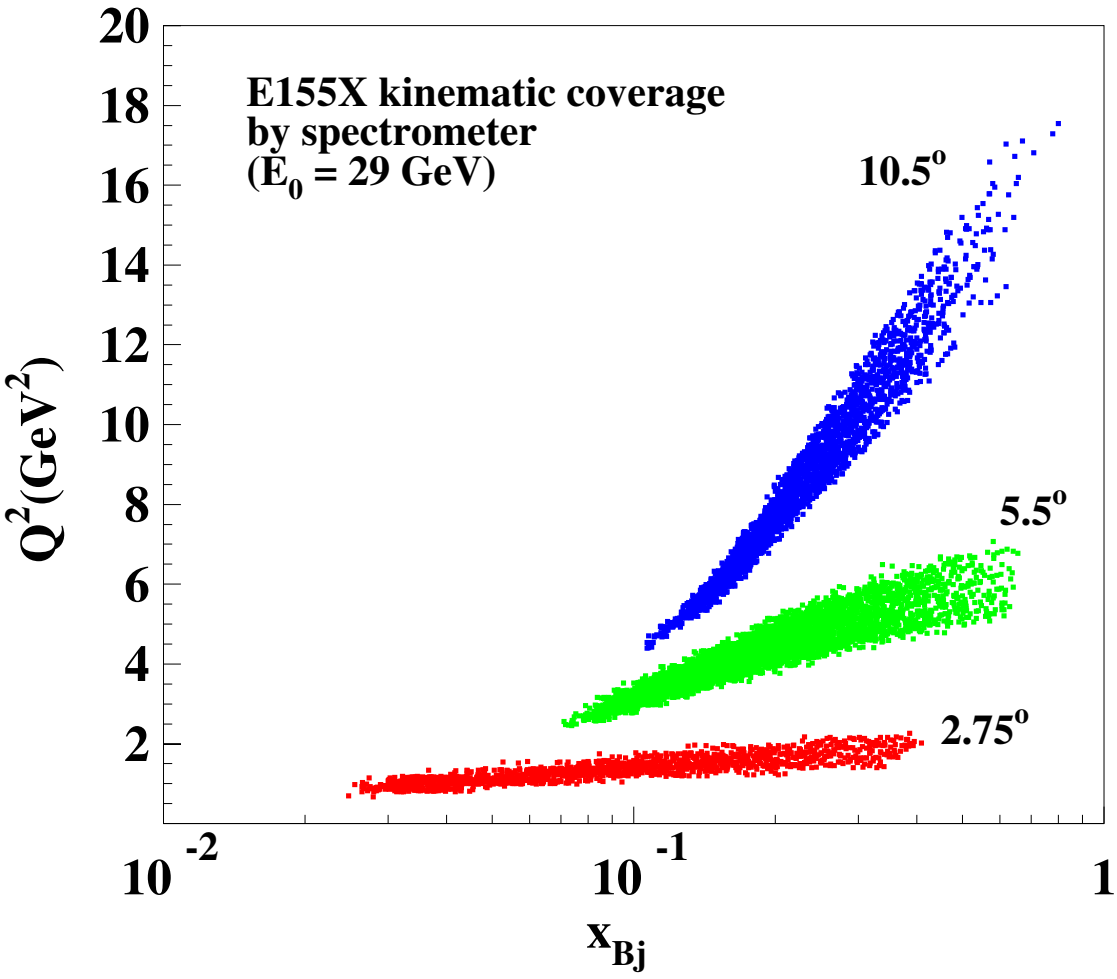

Figure 11: Q^2 vs. Bjorken x_{Bj} kinematic coverage of the three spectrometers.

3.3.3 Threshold Gas Cherenkov Counters

To identify the particles passing through the spectrometers, threshold Cherenkov gas detectors were used. The 2.75° and 5.5° spectrometers each had two tanks (2C1, 2C2, 5C1 and 5C2 respectively), and the 10.5° spectrometer had one tank (10C). These tanks were large vessels filled with a mixture of 90% nitrogen (N_2) and 10% methane (CH_4) [48]. Pure nitrogen is a traditional gas used in Cherenkov gas detectors, but the addition of methane had the effect of quenching most of the scintillation light produced in the nitrogen [49].

The mechanism of the threshold Cherenkov gas counters is based on a straightforward concept. Namely, a charged particle traveling through a medium with a velocity greater than the phase velocity of light (c/n, where n is the index of refraction of the medium) will produce Cherenkov radiation [50]. Moreover, the minimum momentum at which a particle with mass m will have a velocity greater than this threshold (c/n) is given by

$$p_{min} = \frac{mc}{\sqrt{n^2 - 1}} \tag{6}$$

Particles with different masses will have different threshold momenta. The threshold of the Cherenkov gas tank is a function of the index of refraction of the gas, which varies by changing the pressure of the gas. The gas is assumed to behave as a perfect gas [51]. The pressures in the tanks were chosen to prevent hadrons, mainly pions, from producing a signal while making sure electrons did. The threshold for electrons was set at about 50 MeV. Pions were below threshold if there energy was less than

19 GeV in the 2.75° spectrometer, 16 GeV in the 5.5° spectrometer and 13 GeV in the 10.5° spectrometer. The kaon threshold was 50 GeV and the proton threshold was 100 GeV.

Moreover, the number of Cherenkov photons produced depends on the velocity of the particle [52]. Once the particle is well above threshold (eg: all electrons and some pions), the number of photons produced is constant. This provides an additional way of differentiating electron candidates from hadrons.

The Cherenkov radiation emitted by the particles passing through the tanks was reflected by large, thin mirrors onto photomultiplier tubes (PMTs) in the tanks. The anode signal of each PMT was connected to a VME flash ADC (FADC), and the dynode signal was connected through a fan-out to four discriminators, each with a different threshold. The signals from these discriminators were sent to TDCs [48]. The FADCs sample the PMT output at 1 ns intervals and convert the voltage signal to digital values. The FADCs provided a full waveform which allowed the resolution of two different signals close together in time. This led to a better measurement of the amplitude of the signal. However, at times these FADCs were not very reliable, and the TDC backup system was used in these instances. The information provided by the backup system was not as precise as for the FADC system, but sufficient for a rough particle identification.

Analysis software was written to find pulses in the waveform and determine their height and integrated size. This analysis will be summarized in Sec. 4.1.4.

3.3.4 Shower Counters

Each of the three spectrometers had a shower counter which consisted of a stack of lead glass blocks instrumented by PMTs. As their name indicates, the shower counters measure the energies of electromagnetic showers produced by incident particles. An electromagnetic shower consists of the repetition of two successive interactions. First, the high energy charged particles interact with the atoms in the material and bremsstrahlung radiate. This interaction produces a photon which in turn interacts with the atoms and produces an electron-positron pair. These electrons then interact with atoms and emit bremsstrahlung radiation, and the cycle continues. The energy of the particles decreases as :

$$E(z) = E_0 e^{-z/L_{rad}} \tag{7}$$

where L_{rad} is the radiation length of the material. The shower of particles almost stops when the particle energies become less than the critical energy (E_{crit}). The critical energy depends on the absorbing material and is typically tens to a few hundred MeV. At this critical energy, the energy loss rate due to ionization and excitation becomes equal to the energy loss rate due to bremsstrahlung.

The shower counters are in reality Cherenkovs counters, which enable the identification of electrons by providing a measure of the energy of the incident electron. To understand how the Cherenkov light provides a measurement of the energy of the incident particles, it is necessary to consider the total length of all the shower track lengths. The shower track length of the electromagnetic shower is the

sum of the distances traversed by each of the particles in the shower. For an electron, the full electromagnetic shower is contained within the material, and therefore, the shower track length is proportional to the energy of the incident electron. Moreover, in a material with a high index of refraction, all of the electrons will emit Cherenkov light until they have reached extremely low energies. The amount of light produced is proportional to the shower track length, which in turn is proportional to the incident energy of the electron. Thus, by measuring the amount of Cherenkov light produced, we obtain a measurement of the energy of the electron. The knowledge of the shower energy is an important key to differentiating electrons from hadrons.

Unlike electrons, hadrons will generally only deposit part of their energy in the shower counter. In fact, most hadrons do not shower at all, but simply emit Cherenkov radiation as they pass through the block. However, some hadrons can inelastically collide with a nucleus in the material and produce a shower of particles. The length of these hadronic showers is usually much longer than that of electromagnetic showers, so the hadronic shower is not fully contained in the calorimeter. In sum, hadrons almost always deposit a small amount of their energy in the shower counter, as compared to the electrons which deposit all of their energy. Thus, the amount of energy deposited is a good criterium to use to differentiate between the two. A more powerful tool is the ratio of the energy to the momentum, E/p. At the relativistic energies involved in this experiment, an electron's measured energy, E, will be about equal to its momentum, p, whereas a hadron's shower energy will be smaller than its momentum.

The shower counters in 2.75° and 5.5° spectrometers each consisted of 20 rows by 10 columns of lead glass blocks. Each 6.2 cm x 6.2 cm x 75 cm block had its long axis parallel to the z-axis of the spectrometers. A length of 75 cm of lead glass corresponded to about 24 radiation lengths for the particles to go through. The index of refraction of the lead glass was 1.62. The stack in the 5.5° spectrometer was raised by 16 cm compared to experiment E155. Because of beam optics, at the lower beam energies of E155X, the lower three rows would not be hit by electrons. Raising the shower counter also provided better coverage of the top rows [53]. The 2.75° and 5.5° shower counters were enclosed in aluminum boxes and angled a few degrees relative to the horizontal direction so that particles would not go entirely through the small gaps between the blocks.

The shower counter in the 10.5° spectrometer was of a slightly different design. It consisted of a 2 radiation length pre-radiator (PR) and a 15 radiation length total absorber (TA). The PR was segmented vertically into ten horizontal bars, each bar having a PMT at either end. The TA consisted of 30 lead glass blocks, stacked 6 blocks wide by five blocks tall. Reference [54] contains specific details about the 10.5° spectrometer PR and TA. For E155X a lead pre-pre-radiator, which consisted of a 0.25 inch thick lead sheet placed in front of the PR, allowed the electromagnetic showers to start sooner, therefore increasing the signal, which resulted in an enhanced performance of the PR for E155X as compared to E155.

3.3.5 Scintillator Hodoscopes

Scintillator hodoscopes were used to track the charged particles going through the spectrometers. By tracking the particles we were able to accurately determine their paths through the spectrometers, and thus measure their momentum and scattering angle, θ.

The hodoscopes consisted of several planes of long fingers of plastic scintillators. The scintillators were instrumented by PMTs. The combination of the scintillator and the PMT was referred to as a hodoscope finger. The PMTs were connected to discriminators. The signals from the discriminators were sent to TDCs set in leading-edge mode. The hodoscope planes were transverse to the particle trajectories.

Particles passing through the scintillators would create scintillation light which was then collected by the PMTs. From the information provided by the electronics, a hit with its exact location and time was determined. The hodoscope hits were matched with Cherenkov and shower counter hits consistent in time and space. A track was thus determined by connecting these spatial hit points. Spreading the hodoscopes out along the z direction in the spectrometers gave a separation of about 5 or 6 meters along the path of the electrons in the 2.75° and 5.5°. With the fine segmentation of the hodoscopes in these two spectrometers, this separation was sufficient to give an angular resolution of about 0.4 mrad and a position resolution of about 5 mm as measured at the location of the shower counter. The momentum of the particle was determined by matching the angle of the track with the tracks

determined by a Monte-Carlo simulation in which particles with known momentum were simulated in the spectrometers.

10.5° Hodoscopes

The 10.5° hodoscopes were built specifically for E155X. There were two packages of hodoscopes in the 10.5° spectrometer. One was upstream of the Cherenkov tank, replacing the one used in E155 which had larger fingers, and thus higher hit rates which led to higher dead time losses. The new smaller fingers reduced the backgrounds to a tolerable level in each finger. The second hodoscope was located immediately downstream of the Cherenkov tank. This hodoscope was added for E155X to improve the tracking resolution in the 10.5° spectrometer compared to E155.

Table 3 describes the details of the front hodoscope package. The fingers were placed in frames which were covered by a light-tight box. The fingers received high voltage through splitters which were adjusted to deliver the appropriate operating voltage to each tube. The operating voltages were determined prior to the experiment by studying the gains of the photomultiplier tubes [55]. During the experiment several fingers in these planes failed, most likely due to the old age of the tubes. A "plane 0" was added in front of plane 1 to compensate for these losses. This plane was made from fingers salvaged from the 10.5° hodoscope for E155. The new fingers were given the names of the fingers they replaced.

Plane Name	Angle (°)	Number of fingers	Location
10H01Y	0	20	10.5° front
10H02Y	0	21	10.5° front
10H03Y	0	20	10.5° front

Table 3: Hodoscope parameters in the front hodoscope package of the 10.5° spectrometer.The angles given are relative to the horizontal.

The downstream hodoscope, also referred to as the rear hodoscope consisted of two planes of fingers as described in Table 4. The fingers were placed in a frame that fit in the limited space between the Cherenkov counter and the shower counter. Specific details on the construction of the frame and assembly of the fingers can be found in Reference [58].

Prior to installing the fingers into the rear frame, they were tested and gain matched. Plateau measurements were performed on the tubes to find their operating voltages. The plateau region of a tube is the region where it has a high hit efficiency without excessive background rates. In this region the efficiency is the least sensitive to changes in the applied voltage. Choosing the operating voltage in this plateau ensures a minimum of counting variations due to drifts in the voltage supplied. The optimal voltages were determined to be around 1700V in most cases. The main difficulty in these measurements came from the lack of information on the tubes which were of different vintages. Reference [59] contains the complete details of these tests.

Once the fingers were placed in the rear frame, precise internal measurements, relative to tooling balls on the frame, were performed prior to installing the entire

Plane Name	Angle (°)	Number of fingers	Finger width (mm)	Finger overlap (mm)	Location
10H04Y	0	24	25.4	12.7	10.5° back
10H05Y	0	25	25.4	12.7	10.5° back

Table 4: Hodoscope parameters in the rear hodoscope package of the 10.5° spectrometer. The angles given are relative to the horizontal.

package in the 10.5° spectrometer hut. Reference [60] contains the details of these measurements.

2.75° and 5.5° Hodoscopes

The hodoscopes in the 2.75° and 5.5° spectrometers were the same ones used in E155 [40, 61]. In these spectrometers the fingers were oriented in three different directions. Horizontal fingers provided a y coordinate, vertical fingers provided an x coordinate, and angled fingers in the U and V planes, provided both x and y components. In both spectrometers there were two packages of hodoscopes, one in between the Cherenkov tanks, referred to as the front hodoscopes, and the second in between the downstream hodoscope and the shower counter, referred to as the back hodoscopes. The individual characteristics of each plane are given in Table 5. The momentum resolution was 2.4% in the 2.75° spectrometer and 2.7% in the 5.5° spectrometer.

Before the experiment all the electronics were checked. Some failing fingers were found but it was impossible to change them without opening the entire hodoscope. The location of most of the planes were determined by survey after the

Plane Name	Angle (°)	Number of fingers	Finger width (mm)	Finger Overlap (mm)	Location
2H1U	+15	44	15	5	2.75° front
2H2V	-15	44	15	5	2.75° front
2H3X	90	64	13	1	2.75° front
2H4Y	0	72	13	1	2.75° front
2H5Y	0	31	30	10	2.75° front
2H6X	90	34	20	7	2.75° front
2H7X	90	90	13	1	2.75° back
2H8Y	0	90	13	1	2.75° back
2H9Y	0	55	30	10	2.75° back
2H10X	90	27	30	10	2.75° back
5H1U	-45	25	45	15	5.5° front
5H2X	90	23	30	10	5.5° front
5H3Y	0	36	30	10	5.5° front
5H4V	+45	25	45	15	5.5° front
5H5U	-45	21	75	25	5.5° back
5H6X	90	27	30	10	5.5° back
5H7Y	0	55	30	10	5.5° back
5H8V	+45	21	75	25	5.5° back

Table 5: Hodoscope characteristics in the 2.75° and 5.5° spectrometers. The angles shown are relative to the horizontal.

experiment [56, 57]. This new survey was performed after finding some problems with the tracking efficiency. The new survey numbers improved the tracking efficiency by a few percent, and resolved some long-standing questions from E155 and E154. The details of this surveying are discussed further in section 4.1.5.

3.4 Data Acquisition and Monitoring

A VME-based system [62] was used to read in the data from the various CAMAC modules (TDCs, ADCs and discriminators) and VME modules (FADCs).

CAMAC and VME are international standards for electronics modules and interfacing electronics with a computer. Figure 12 shows a block diagram of this VME-based system. The upper right block shows the readout from the detector electronics. The lower right block shows the silo tape servers used to store the data. The data acquisition system read the data from detector electronics and wrote it to tapes locally in End Station A for every beam spill. Additional software was used to transfer the data from local tapes to 1 GB tapes into storage. The data acquisition system could handle rates of about 1 MB per second. About 3000 runs were recorded on tape, with each run lasting about half an hour. Calibration runs (LED, pedestal and toroid runs) were performed frequently.

In addition to these VME and CAMAC systems, E155X also used interactive programs to control and monitor the various detector hardware systems, such as the high voltage to the detectors, the low voltage in the CAMAC crates and spectrometer magnet power supplies. The DAQ control software was run on a VAX workstation using messaging to control the various parts of the data acquisition. The incoming data was monitored at four different workstations, one for each spectrometer and one for the beam data. An on-line analysis at each of these workstations was run during the entire data collection to monitor the quality of the data and to detect the failure of any of the systems in order to perform repairs as soon as possible.

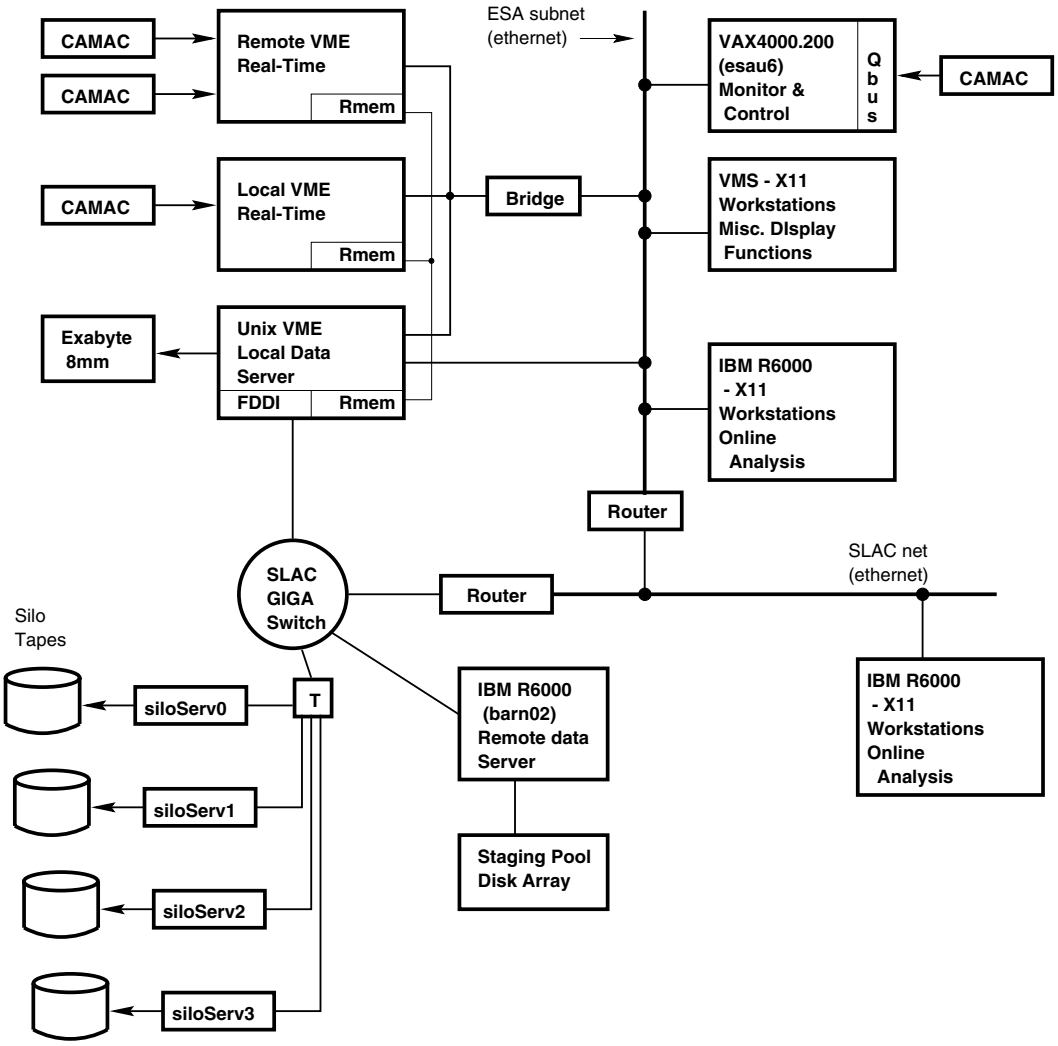

Figure 12: Block diagram of the Data Acquisition system.

CHAPTER 4

Data Analysis

The data analysis was performed in several stages. The first stage, "Raw Data Analysis", involved the processing of the data tapes collected during the run, referred to as the raw data tapes, into data summary tapes. The next stage, "Event Selection", was the creation of "counts files" which contained a selection of electron events from the data summary tapes. The last stage, "Asymmetry Measurement", was the determination of the asymmetry from these count files. Corrections were then applied to the measured asymmetry to obtain the physics asymmetry, and from that g_2. The following sections describe in detail each of these steps in the data analysis.

4.1 Raw Data Analysis

The raw data tapes were processed using a "group analysis code" and a "batch computing system" to make data summary tapes, known as the DSTs. The group analysis code was a collection of Fortran 90 subroutines which handled different parts of the analysis of raw data tapes. The group analysis code also contained some subroutines written in C language for the input and output handling. The batch computing system included an interface to a computer farm consisting of

about thirty IBM UNIX machines. Each machine processed two raw data tapes at a time. The time required to reconstruct the electron and hadron candidates from one raw data tape was about one day of real time. The information from the raw data tapes was processed spill by spill, with each spill corresponding to a separate record on the raw tapes.

This section starts with a discussion of the motivation for the creation of DSTs. Next the coordinate system used in the data analysis is briefly described. The different parts of the raw data analysis performed are then explained.

4.1.1 Motivation for the DSTs

The clustering and tracking processes dominated the computer time used by the analysis software. Therefore, by having data summary tapes, a considerable amount of time is saved when studying the properties of an electron event sample. For comparison, it took only about twenty minutes to analyze a DST tape, which typically contained 10 runs, while it took about twenty-four hours to analyze a raw data tape containing (in general) only one run. The DSTs were recreated several times as the raw data analysis was refined, to obtain a much cleaner sample of electron clusters, Cherenkov hits and tracks. Relevant beam data were also stored on the DSTs to perform cuts on beam quality and location.

4.1.2 Analysis Coordinate System

In addition to the "spectrometer" coordinate system described in Sec. 3.3.1, an "analysis" coordinate system was also used. The z axis of the analysis coordinate system coincides with the central ray in the spectrometer hut which is angled up by Φ_{cr}=0.81° for both the 2.75° and 5.5° spectrometers, and offset down by Δy=104.9 cm (114.9 cm) in the 2.75° (5.5°) spectrometer relative to the spectrometer coordinate system. The origin of the analysis coordinate system is chosen such that the target is at $z = 0$. The transformation from the spectrometer coordinate system (x',y',z') to the analysis coordinate system (x,y,z) is given by

$$\begin{pmatrix} x \\ y \\ z \end{pmatrix} = \begin{pmatrix} 1 & 0 & 0 \\ 0 & \cos\Phi_{cr} & -\sin\Phi_{cr} \\ 0 & \sin\Phi_{cr} & \cos\Phi_{cr} \end{pmatrix} \begin{pmatrix} x' \\ y' \\ z' \end{pmatrix} + \begin{pmatrix} 0 \\ \Delta y \\ 0 \end{pmatrix} \quad (1)$$

4.1.3 Shower Analysis

The shower counter played a crucial role in the analysis of each spectrometer, because it provided a measure of the energy of the electrons. In each block of the shower counter, a hit was defined by an ADC value greater than the pedestal by at least four counts. The energy due to multiple hits in the same block was separated using the TDC information with a technique known as energy sharing [63], in which the durations of the pulses were examined to assign an amount of energy to each shower. The TDC information also provided a hit time for the individual hits. Adjacent blocks with hit times within a defined time window were grouped together

to form a "cluster". The sum of the energies of all the hits forming a cluster was the energy of the event that produced this cluster. Further details on the shower analysis are provided in Reference [63]. For experiment E155X, the momentum reconstruction in the 2.75° and 5.5° spectrometers was changed as will be described in Sec. 4.1.5, and therefore the shower counter energy calibration values for the 2.75° and 5.5° spectrometers were recalculated. References [64, 65] describe the details of this new calibration.

4.1.4 Cherenkov Analysis

The Cherenkov counters allowed us to differentiate electron candidates from hadron candidates using the measured value of the peak voltage, as described in Sec. 3.3.3. In each Cherenkov counter, the raw FADC spectrum was searched for pulses, and the peak height and area underneath each pulse were measured. These quantities play an important role in the particle identification as will be described later. A more detailed explanation of the Cherenkov analysis is provided in Reference [48].

4.1.5 Tracking

The raw hodoscope TDC hits were grouped together with shower clusters and Cherenkov hits consistent within a time window and consistent within a defined spatial volume for the hodoscopes and shower clusters. The hits that were grouped together were required to belong to the same straight line which consti-

tuted a "track". The tracks are qualified by their "class" which describes which combination of detector systems was used to fit a track. The two different track classes used for the E155X analysis were:

- Class 1: a shower cluster, at least one Cherenkov hit, and at least the minimum number of hodoscope hits (6 and 4 hits in the 2.75° and 5.5° spectrometers respectively).

- Class 2: a shower cluster and at least the minimum number of hodoscope hits; no Cherenkov hit found within the time window.

More details on the tracking process can be found in Reference [63]. The following sub-sections will discuss additional studies involving the tracking.

Tracking parameter input study

For E155X, a study was done on the tracking input parameters to improve the tracking efficiency in the 2.75° and 5.5° spectrometers, while optimizing the speed of execution of the tracking code. The tracking input parameters in question included confidence level parameters used in the optics cuts to reduce the combinatorial background in the hodoscopes. In addition, the minimum number of hodoscope hits required in a track was also analyzed. Detailed explanations on each of these parameters can be found in Reference [63]. In this study, the electron tracking efficiency was measured for different values of these paramaters. When changing the minimum number of hits required in a track, the E/p values of the tracks found

were also taken into account to make sure that these were electron tracks. This study led to reducing the minimum number of hodoscope hits required in a track compared to E155, as well as slightly reducing the confidence level windows. The specific results of this study can be found in Reference [66]. The new values for these parameters chosen for E155X improved the tracking efficiency by 1% in the 2.75° spectrometer and by 3% in the 5.5° spectrometer. The electron tracking efficiencies in the 2.75° and 5.5° spectrometers were respectively 97.5% and 92.8%. The execution time of the code improved by about 2.4% with these new parameters. The electron tracking efficiency was taken as the ratio of the number of events with tracks to the number of events with an electron-like signal in the Cherenkov and shower counters.

Adjustment of hodoscope finger positions

Questions about the positions of several hodoscope planes were raised during E155. However, final resolution of these questions was not possible while the Cherenkov tanks were blocking the view of the hodoscopes. The planes in question, 2H1U, 2H1V, 2H4Y, 2H5Y, 2H8Y, 2H9Y, 5H3Y and 5H7Y, were the ones which provided a measure of y position information, which directly affects the track momentum.

As a temporary fix, a study was performed for E155X by moving the position of the fingers in these hodoscope planes vertically in the software along the y axis to determine the positions that resulted in the highest tracking efficiency. Once

the Cherenkov tanks were removed, the surveyors were able to survey fingers in the hodoscopes in question. The numbers obtained from the surveyors were converted to the analysis coordinate system using the matrix in Sec. 4.1.2. The results of the survey revealed that the actual positions of the fingers were indeed slightly different from the original E155 numbers and consistent with the results determined from the study mentioned above. Further details of this survey can be found in References [56] and [57].

Hodoscope timing offsets

To accommodate the backgrounds for E155X, new voltages were used for the hodoscopes. As a result, new timing offsets, determined by finding time coincidences between detector hits, had to be evaluated to maximize the hit efficiency while minimizing the background.

The hodoscope timing offsets were adjusted in two stages. The first stage consisted of adding offsets to the hodoscope hit times to remove the time difference between these hodoscope hits and their corresponding Cherenkov hits in C1. The second stage involved comparing the hodoscope hit times with the corresponding track time. The details of the timing offset determination for the 2.75° and 5.5° spectrometers can be found in Reference [67]. The second stage which involved the tracking was not performed in the 10.5° spectrometer as the tracking was not as efficient as in the smaller angle spectrometers.

Data Sample	2.75°	5.5°	10.5°
Proton 29 GeV	428	422	327
Proton 32 GeV	688	727	712
Deuteron 29 GeV	264	283	165
Deuteron 32 GeV	401	406	403

Table 6: Number of runs used in each spectrometer for each target and beam energy.

4.2 Run Selection

As the DSTs were being produced, each run was checked to make sure that the analysis worked properly and that there were no hardware failures during the data taking. Good runs were selected for each spectrometer by monitoring the histograms produced during the DST processing. Among the variables that were examined were the Cherenkov peak voltage spectrum, the E/p spectrum, the time difference between Cherenkov hits and shower hits, the momentum spectrum, and the reconstructed θ and Φ angles. A total of 3010 runs were written to tape. Table 6 shows the number of runs used in the analysis for each target type and beam energy. About a quarter of the total number of runs collected were calibration runs. In the 2.75° spectrometer, the main reason for not using several of the runs was the failure of the 2280 ADC controllers. This failure resulted in the loss of the shower counter data in the 2.75° spectrometer. In the 5.5° spectrometer, problems with FADCs in the beginning of the experiment resulted in the loss of several runs. Low target polarization also led to the loss of a few runs.

4.3 Electron Event Selection

Electron events were selected in the three spectrometers using a Fortran 90 code known as the "counts making code". The counts making code created files (known as the counts files) which contained the number of electron events found for each run using the DSTs. A counts file was produced for every asymmetry run.

Several beam cuts, which were the same for all three spectrometers, were used for the event selection. First, a cut on the beam charge for each spill was implemented. This cut required that the beam charge measured by the most reliable of the two toroids, which was toroid 2, was in the range $[0.5 \times 10^9, 5 \times 10^9]$ electrons per spill, otherwise the spill was not used. Toroid 1 was unreliable because it was located in a high background area. The second cut was on the polarization bit. If the polarization monitor PMON, described in Sec. 3.1, did not register 1 (for left polarization) or 2 (for right polarization), the event was not counted. Only about fourteen runs did not register a correct value for the polarization bit for all events in the run. Specific details on the polarization bits study can be found in Reference [39].

The additional cuts required for the electron definition were different for each spectrometer. The 2.75° and 5.5° definitions were similar, whereas the 10.5° definition required a "hybrid" definition as will be explained in the following sections. The 10.5° spectrometer will be presented first since it used a completely new algorithm designed specifically for E155X. This was required because the 10.5° spectrometer was upgraded as discussed previously and therefore the E155 code could not be

used for this spectrometer. For the 2.75° and 5.5° spectrometers, a slightly modified version of the E155 code was used. The main goal of the electron definitions was to maximize the statistics while reducing the pion contamination (main background) as much as possible.

4.3.1 Electron cuts in the 10.5° Spectrometer

The algorithm used to determine electron events in the 10.5° spectrometer was a hybrid electron definition because electrons were defined both with and without associated hodoscope tracks. The diagram in Fig. 13 describes this algorithm. The algorithm starts with an outer loop over all Cherenkov hits and then an inner loop over all the shower clusters. Inside these two loops, the tracks are searched to find if one was formed with this Cherenkov hit and cluster by the tracking code. If a track is found then it must also pass some cuts described below to determine if it is an electron event. However, since the tracking in the 10.5° spectrometer was not perfect, electron candidates were also formed by using only Cherenkov hits in coincidence with shower clusters. The additional cuts required in this case are also described below. The electron cuts in the 10.5° spectrometer were:

- The Cherenkov peak voltage (V_{peak}) is greater than 15 FADC counts
- The shower energy (E) is greater than 5 GeV
- |C1(hit time) - Shower(hit time)| $<$ 4ns
- If a track exits: E/p $>$ 0.75 where p is the momentum

- If no track exits: V_{peak} >20 and $E/E_{min} > 0.9$

where E_{min} is the minimum energy a spectrometer electron would deposit in a particular shower counter block as determined by a Monte Carlo program.

A peak voltage in the Cherenkov counter greater than 15 FADC counts was used to separate out the electrons from the hadrons. In principle, only electrons were supposed to produce a peak voltage in the threshold Cherenkov counters as explained in Sec 3.3.3. However, hadrons can also produce scintillation light in the counters, but the peak voltage recorded is lower compared to electrons. Figure 14 shows the difference in the peak voltages produced by hadrons and electrons.

An energy greater than 5 GeV measured by the shower counter was required since electrons have more than a 99% probability of depositing all of their energy into the calorimeter through electromagnetic showering, whereas pions generally do not produce electromagnetic showers. Figure 15 shows the energy spectrum in the 10.5° spectrometer, from which we can see that electrons have energies greater than 5 GeV, while most of the pions/hadrons deposit less than 5 GeV.

The Cherenkov hit must be close in time with the shower cluster to assure that it was produced by the same particle that produced this particular shower cluster. Figure 16 shows the time difference between hits in the Cherenkov and shower counters. The hits with time differences in the range (-4 ns,4 ns) are considered to be due to electrons. The excellent signal to background ratio in Fig. 16 permits the use of the hybrid definition where a track is not necessarily required for an electron

event.

In the case where a track is found, the E/p cut is based on the fact that electrons will most likely deposit all their energy in the calorimeter. Thus, the energy E for electrons in the spectrometer as measured by the shower counter will be very close to the momentum of the particle as measured using the track. Therefore, the ratio E/p for electrons should be very close to 1. Figure 17 shows the difference between the E/p values for electrons and hadrons. A cut of E/p greater than 0.75 was used if a track was found, to ensure that no electrons were being lost.

If a track was not found, then the peak Cherenkov voltage was required to be greater than 20 FADC counts instead of just 15. This stricter cut on V_{peak} increased the chances that an electron was being detected. An additional cut on the ratio E/E_{min}, defined previously, was used.

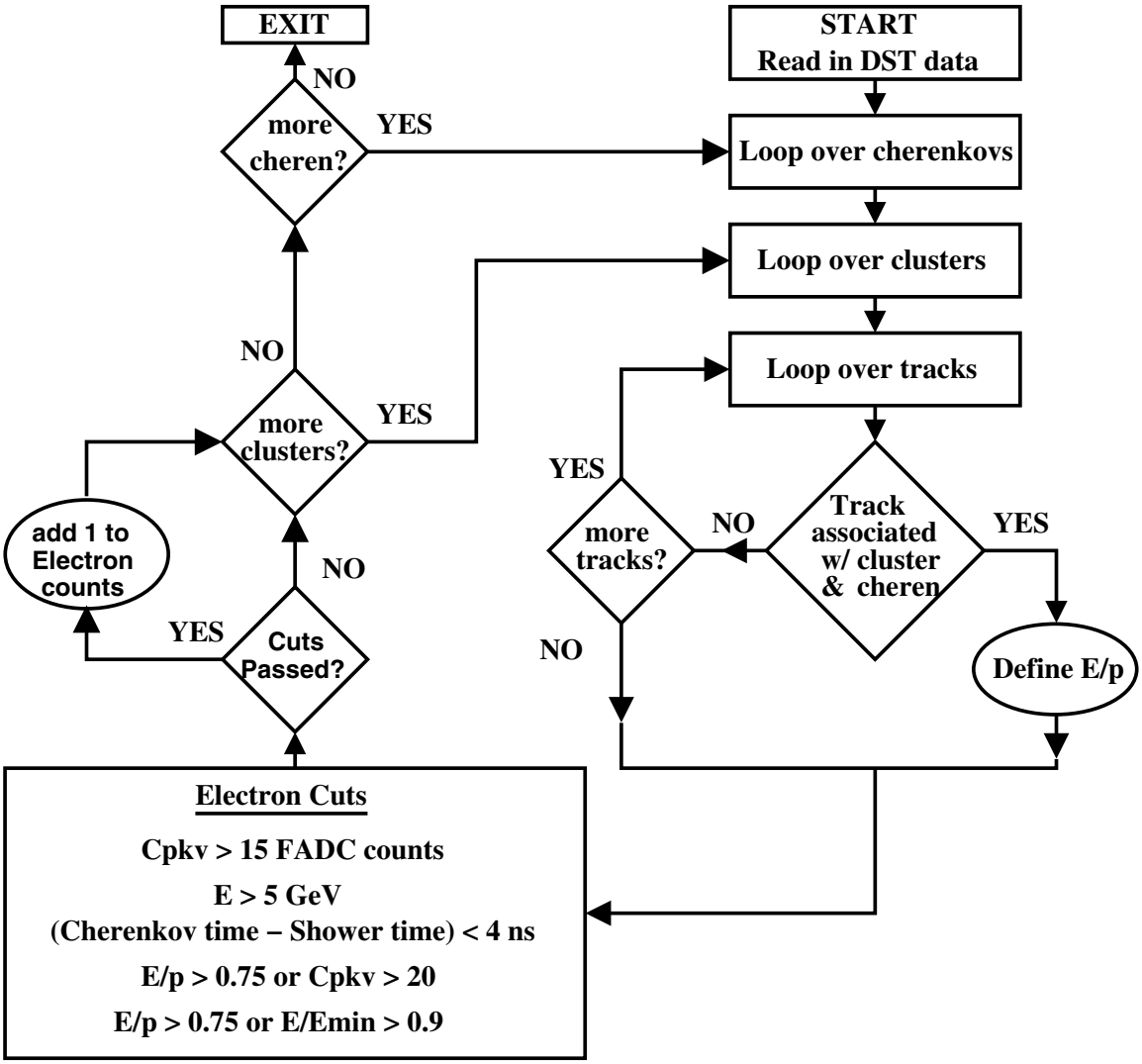

Figure 13: Algorithm used for the electron selection in the 10.5° spectrometer

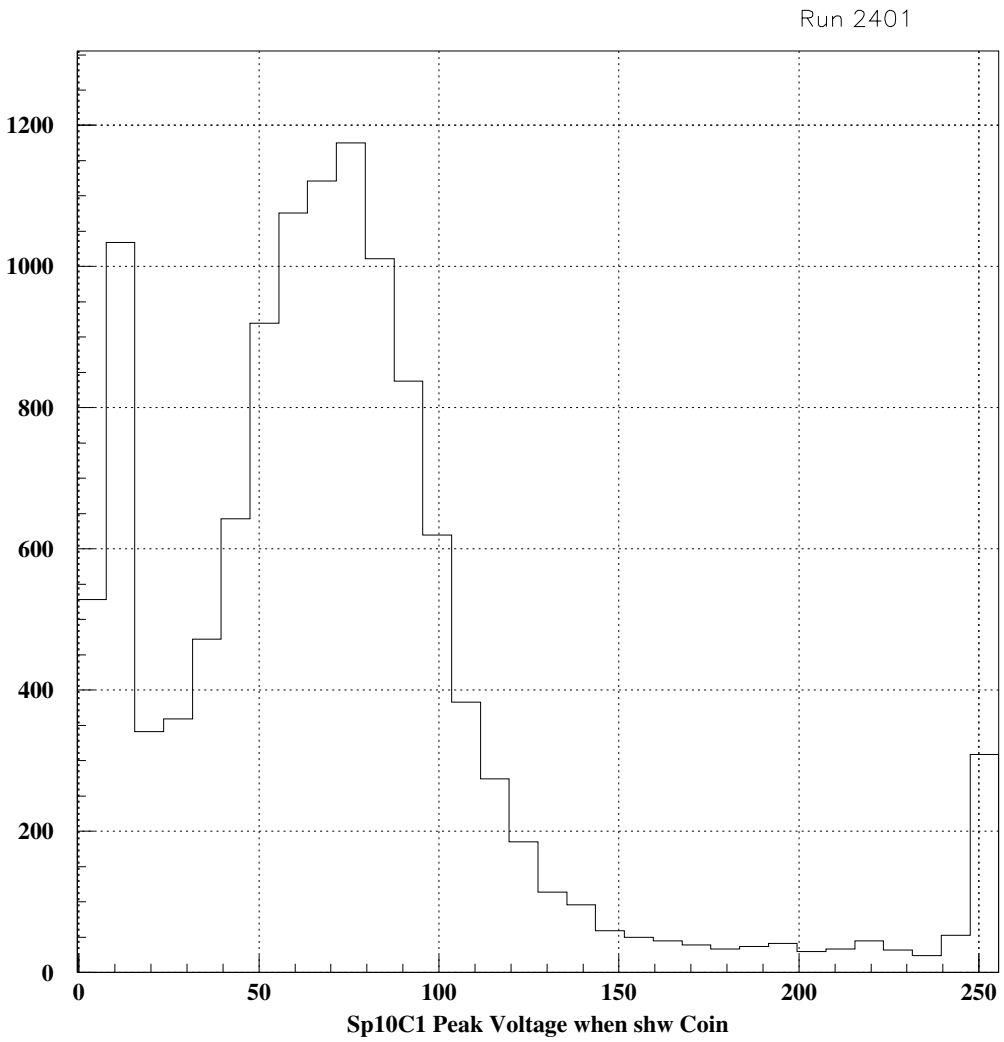

Figure 14: Event distribution of peak Cherenkov FADC voltage for 10C1 when the Cherenkov and shower hits are in time coincidence. The peak at around 10 V is produced by hadrons, and the peak at around 75 V is produced by electrons. The peak at around 250 is from the saturation of the FADC. A cut of 15 FADC separates the electron events from the background.

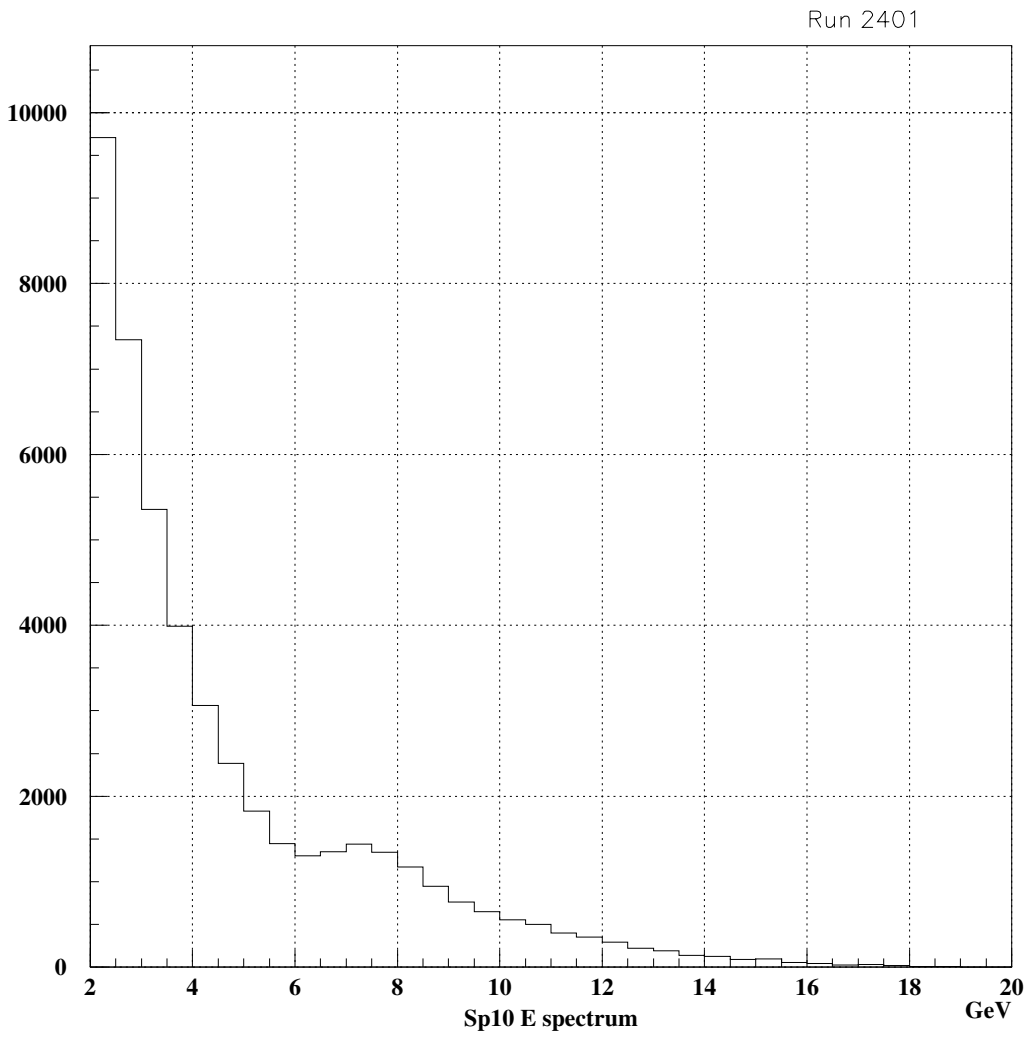

Figure 15: Energy spectrum for all events in the 10.5° spectrometer. The accumulation below about 5 GeV is produced by hadrons and edge block events. The broad peak at about 7 GeV is produced by electrons. An energy cut at 5 GeV removes a large fraction of the background.

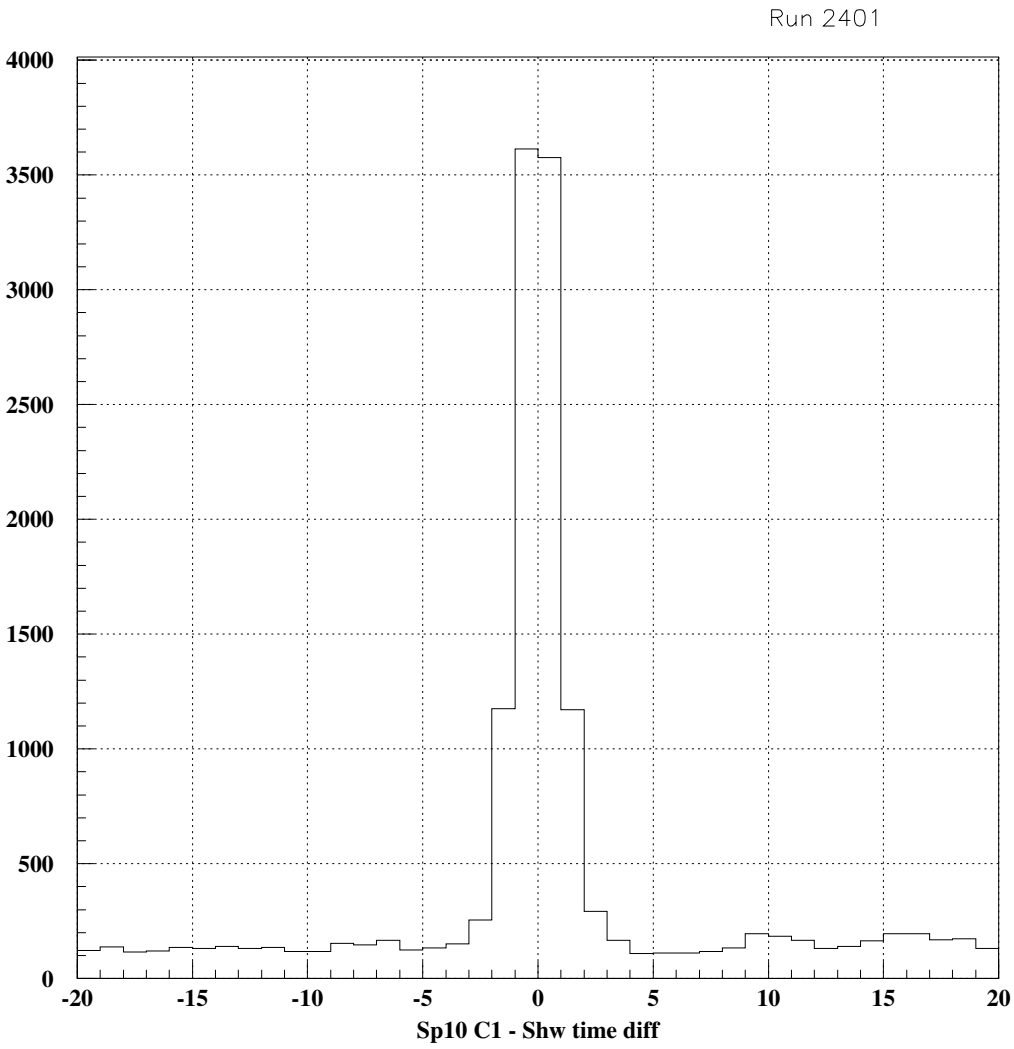

Figure 16: Event distribution of the time difference in ns between Cherenkov and shower counter hits for the 10.5° spectrometer. The signal is contained in a window of about 8ns. Electron events must have a time difference in the range [-4 ns,4 ns].

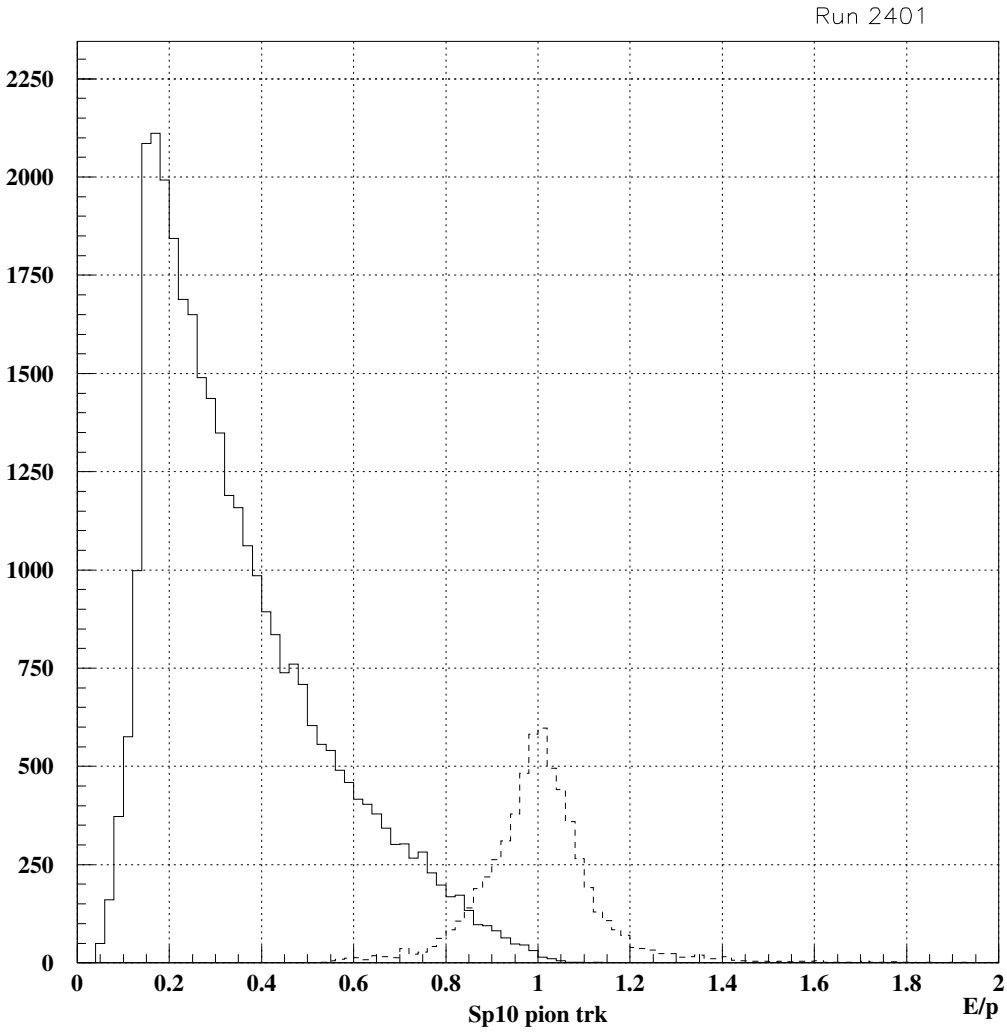

Figure 17: E/p spectrum for pion tracks in the 10.5° spectrometer (solid curve). The electron E/p spectrum (dashed curve) is plotted on top to show the difference between E/p distributions for electrons compared to hadrons.

4.3.2 Electron cuts in the 2.75° and the 5.5° Spectrometers

Th electron definition in the 2.75° and 5.5° was :

- Class 1 track with E/p > 0.75
- E >8 GeV
- Two Cherenkov hits in time coincidence
- $\sqrt{V_{peak1} \times V_{peak2}}$ > 20 FADC counts OR V_{peak1} > 30 FADC counts OR V_{peak2} >30 FADC counts

Where V_{peak1} and V_{peak2} are the peak voltages respectively in C1 and C2. This last cut was modified compared to E155 by adding two OR statements that would compensate for the random failure of the FADCs during the run. If only one tank recorded a substantial signal, this was sufficient along with the other cuts to identify an electron. The rest of the cuts used on the 2.75° and 5.5° spectrometers are based on the same principles explained in Sec. 4.3.1.

4.4 Asymmetry Measurement

The raw asymmetry was measured using the electron counts stored in the counts files described in Sec. 4.3. The raw asymmetry was determined run by run using equation 2:

$$A^{raw} = \frac{(\frac{N}{Q})^{\downarrow\Leftarrow} - (\frac{N}{Q})^{\uparrow\Leftarrow}}{(\frac{N}{Q})^{\downarrow\Leftarrow} + (\frac{N}{Q})^{\uparrow\Leftarrow}} \tag{2}$$

where $\downarrow$ and $\uparrow$ indicate the two helicity states of the incident electrons, and $\Leftarrow$ indicates that the target field is perpendicular to the beam. The ratio N/Q is the number of counts (N) normalized by the incident charge (Q). In E155X, the target field was actually at an angle α=92.4° from the beam direction instead of 90°. The consequence of this rotation was that a more general formula was needed to determine g_2. This angle rotation will be discussed in Sec. 4.7. The raw asymmetry was measured for each x bin in each spectrometer, and accumulated over all runs.

The raw asymmetry was corrected for the beam polarization P_B, the target polarization P_T, the target dilution factor f, and the target nuclear correction C_1. The uncorrected measured asymmetry, $A_{\perp}^{uncorr}$, is written:

$$A_{\perp}^{uncorr} = \frac{A^{raw}}{P_B P_T f C_1} \tag{3}$$

We are using the subscript $\perp$ in the asymmetry notation because the dominant contribution comes from the perpendicular part despite the rotation of 2.4° away from a true perpendicular orientation. These correction factors, P_B, P_T, f, and C_1, were applied on a run by run basis, and will be addressed individually in the following sub-sections.

4.4.1 Beam Polarization

The beam polarization is the net fraction of electrons in the beam that are polarized in the desired direction, and its sign depends on the beam energy. All the electrons in the beam can scatter off the nucleons in the target. However, only the net polarized contribution should be taken into account in the physics asymmetry measurement. The raw asymmetry must therefore be corrected for the beam polarization, P_B. Møller polarimetry was used to measure the beam polarization as described in Sec. 3.1. The result of this measurement was $P_B = 0.832 \pm 0.002 \pm 0.031$. Reference [68] describes the details of the analysis of the Møller measurements.

4.4.2 Target Polarization

The target polarization is the net fraction of nucleons in the target that are polarized in the desired direction. The incident electrons can scatter off all the nucleons in the target, however we must only take into account the nucleons that were polarized to determine the physics asymmetry. Thus the raw asymmetry must also be corrected for the target polarization, P_T. As described in Sec. 3.2, the target polarization was measured using Nuclear Magnetic Resonance. The target polarization was measured on-line during the experimental run. However, the actual values used in the data analysis were determined by an off-line analysis performed after the target technical run. This off-line analysis is described in Reference [69]. Figure 18 shows the the corrected polarizations per run used in the analysis. The fractional error on the target polarization was found to be 0.017.

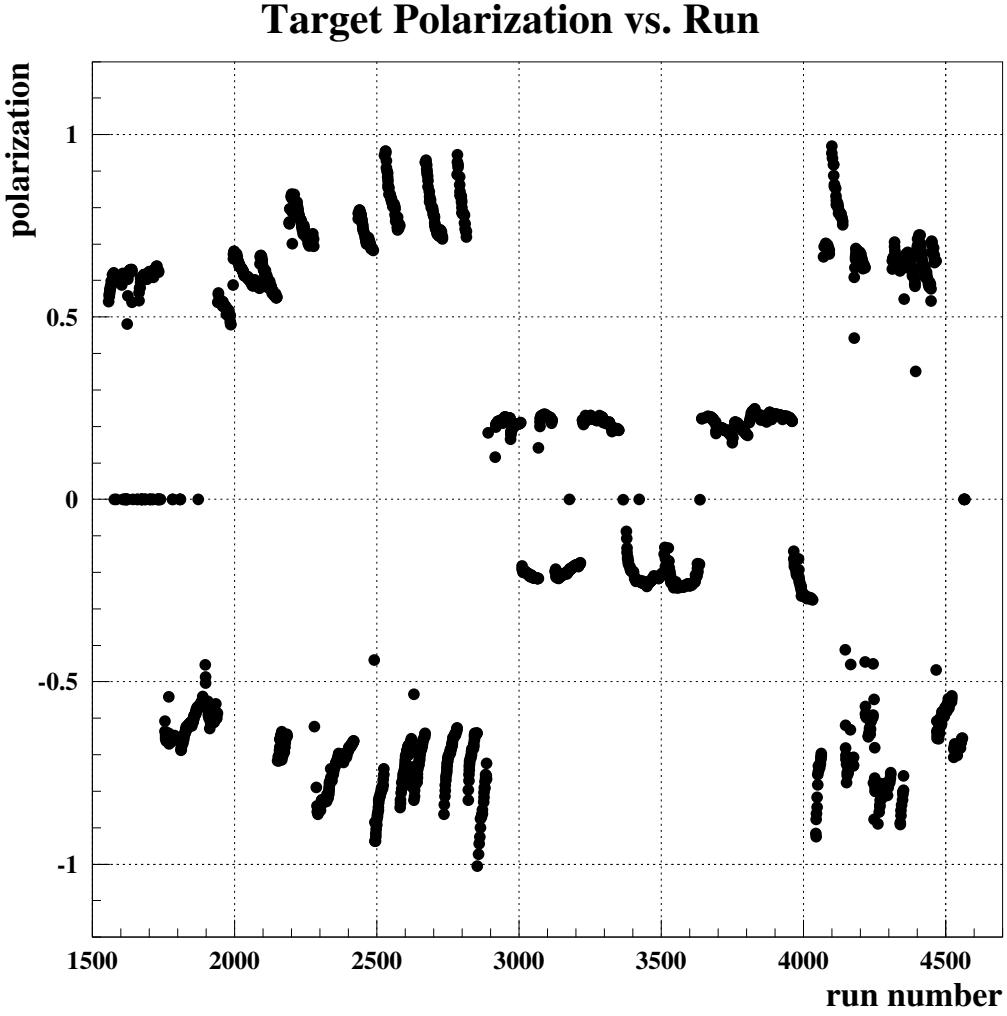

Figure 18: Target polarization as a function of run number. From run 2887 to 4044, the deuteron target was used. For all other runs the proton target was used.

4.4.3 Dilution Factor

The incident electrons not only can scatter off the polarized nucleons in the target, but also from unpolarized nucleons and non-target materials such as ^{4}He and the support framework. These unpolarized materials "dilute" the measurement of the physics asymmetry and are accounted for by the dilution factor. A detailed analysis of the dilution factor was performed for E155X, and is described in Reference [70]. The average value of the dilution factor for the proton target was about 0.2, with an average uncertainty of about 0.0035.

4.4.4 Nuclear Corrections

When polarizing the primary target material, which is $^{15}NH_3$, the goal is to polarize the hydrogen. However, the nitrogen is polarizable as well, and contributes to the measured asymmetry. The nitrogen consists mostly of ^{15}N with a small fraction of the total nuclei being ^{14}N. Based on Reference [71], the asymmetry is corrected for the polarized nitrogen using

$$C1 = 1 - \frac{1}{3}\frac{1}{3}\frac{P_N}{P_P} g_{EMC}(x) \tag{4}$$

with the -$\frac{1}{3}$ due to Clebsch-Gordon coefficients from the nitrogen wave function, the following $\frac{1}{3}$ due to one nitrogen atom per three hydrogen atoms, g_{EMC}(x) is the factor for the EMC effect [26], taken at atomic mass 15, and $\frac{P_N}{P_P}$ is the ratio of ^{15}N to proton polarization. For the target material $^{1}5NH_3$, the following fit was used to

express P_N in terms of P_P:

$$P_N = 0.136P_P - 0.183P_P^2 + 0.335P_P^3 \tag{5}$$

This nuclear correction was on the order of 1%. A description on how this correction was implemented in the analysis code can be found in Reference [72].

4.5 Corrections to the Measured Asymmetry

Several corrections must be applied to the measured asymmetry $A_\perp^{uncorr}$, discussed in Sec 4.4. First, a correction for the electroweak asymmetry was applied, and the obtained asymmetry is denoted $A_\perp^{corr-ew}$. Next the background contamination was removed, and the obtained asymmetry is denoted $A_\perp^{corr-bk}$. Finally, a correction for the radiative effects is applied to extract the physics asymmetry $A_\perp$. The corrections needed to obtain $A_\perp$ from $A_\perp^{uncorr}$ will be discussed in detail in the following sub-sections.

4.5.1 Electroweak Correction

The electroweak interaction of the polarized beam with any material produces an asymmetry which arises from the parity violating interference between electromagnetic and weak coupling. This asymmetry, known as the electroweak asymmetry, is unrelated to the DIS asymmetry $A_\perp$, and therefore must be subtracted out run by run as shown in Eq. 6

$$A_\perp^{corr-ew} = A_\perp^{uncorr} - (1/fP_TC_1)A_{ew} \tag{6}$$

where A_{ew} is the electroweak asymmetry, and radiative corrections are neglected. Additional details on the electroweak asymmetry can be found in reference [74].

The contribution of the electroweak asymmetry to the measured asymmetry was minimized experimentally by running about equal time with opposite target polarizations. To understand how the contribution of the electroweak asymmetry was minimized, consider two runs with opposite target enhancements, but with all other factors, including the number of electron events, being equal. If run 1 has positive target enhancement (target polarization parallel to the target magnet field) and run 2 has negative target enhancement (target polarization anti-parallel to the target magnet field) then adding the asymmetries from these two runs we would obtain:

$$A_\perp = \Big[A_\perp^{uncorr(1)} - (1/fP_TC_1)A_{ew}^{(1)}\Big] + \Big[A_\perp^{uncorr(2)} - (1/f(-P_T)C_1)A_{ew}^{(2)}\Big]. \quad (7)$$

Equation 7 can be re-organized as follows

$$A_\perp = A_\perp^{uncorr(1)} + A_\perp^{uncorr(2)} - (1/fP_TC_1)\Big[A_{ew}^{(1)} - A_{ew}^{(2)}\Big]. \quad (8)$$

The electroweak asymmetries in Eq. 8 (A_{ew}^1, A_{ew}^2) have roughly the same size magnitudes. The effect of the electroweak asymmetry will therefore roughly cancel by having equal numbers of runs with positive and negative target enhancement.

A correction for the electroweak asymmetry is nevertheless needed when comparing the positive enhancement data to the negative enhancement to look for false asymmetries, as will be discussed in Sec. 4.6. Reference [73] gives the expression

for the electroweak asymmetry A_{ew}^{d} in DIS for an isospin symmetric nucleus such as deuterium

$$A_{ew}^{d}(x) = 10^{-4} Q^2(x) \left(0.77 \left[1 + 0.44 R_s(x)\right] + 0.11 Y\right) \tag{9}$$

where the measured average Q^2 at each x bin was used. The term Y is given by

$$Y = \frac{1 - (1-y)^2}{1 - (1-y)^2 - \frac{y^2 R}{1+R}} \tag{10}$$

where y was defined in Sec. 1.1. An approximation was used for $R_s(x)$, which was a ratio of light quark distributions [74]

$$R_s(x) = \frac{2s(x)}{u(x) + d(x)} \approx \begin{cases} 0.5 & \text{for } x < 0.2 \\ 0.0 & \text{for } x > 0.2. \end{cases} \tag{11}$$

For a $^{15}NH_3$ target, the electroweak asymmetry A_{ew}^{p} is roughly equal to A_{ew}^{d}. Radiative corrections should be applied to the electroweak asymmetry A_{ew}^{p}. These corrections were applied through a multiplicative factor which was estimated by roughly extrapolating radiative correction values from Reference [73]. This multiplicative factor was found to be about 0.5.

Figure 19 shows a comparison between the measured asymmetry with both target enhancements combined, with and without a correction for the electroweak asymmetry. Note that the effect is negligible on the final result. Figure 20, on the other hand, shows a comparison between the average asymmetry separated by target enhancement direction, with and without a correction for the electroweak asymmetry. In this case the correction is slightly more noticeable, and tends to make the average asymmetries for most of the cases agree better.

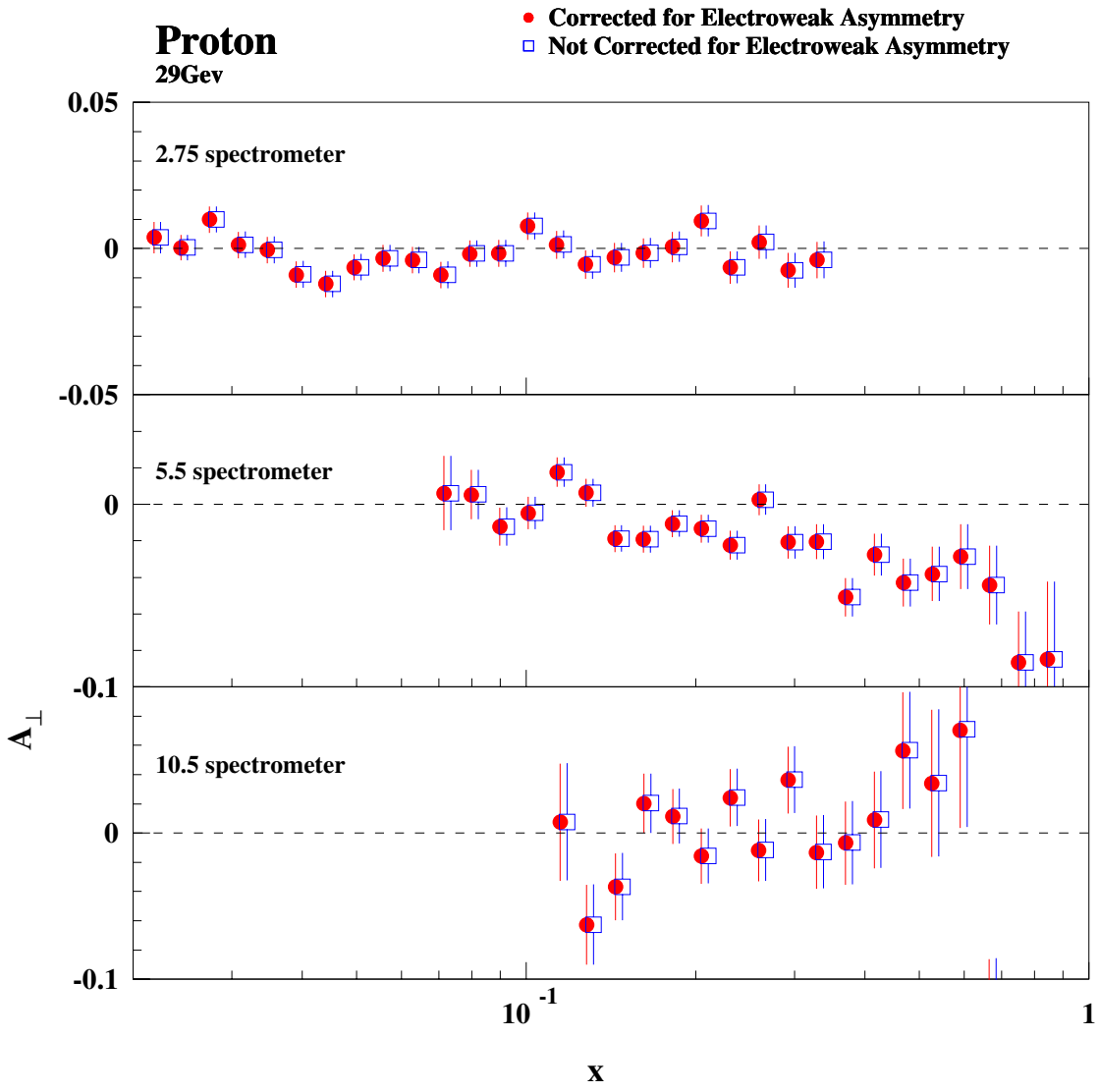

Figure 19: Comparison of $A_\perp$ results with and without the electroweak asymmetry correction applied. No other corrections have been applied yet.

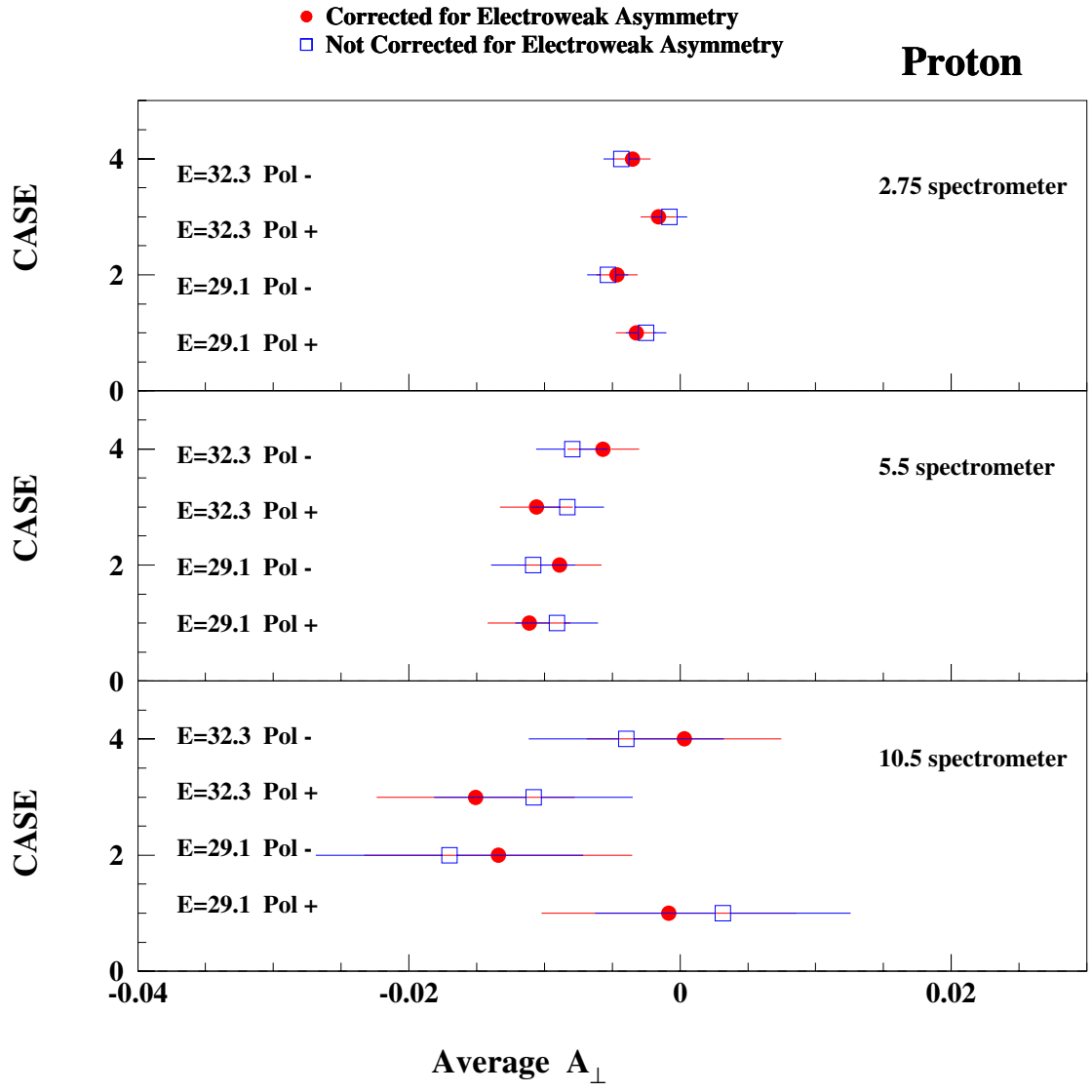

Figure 20: Comparison of the average $A_\perp$ over all bins separated into energy and target polarization, with and without a correction for the electroweak asymmetry. The energies are given in GeV, and Pol - , Pol +, respectively mean negative and positive target polarizations. No other corrections have been applied yet.

4.5.2 Background Substraction

The measured asymmetry can be contaminated by the background, i.e. by pions that were misidentified as electrons, and by non-DIS electrons. The background pions mainly come from the fragmentation of the target nucleons. The non-DIS electrons come from pair-symmetric processes, and are produced in equal numbers with the positrons. The background contamination tends to dilute the measured asymmetry and should therefore be subtracted out.

Qualitative implementation of this correction

The uncorrected measured asymmetry, $A_{\perp}^{uncorr}$, can be written as follows for an electron run

$$A_{\perp}^{uncorr} = \frac{1}{f P_B P_T C_1} \frac{[N_{e-}^L + N_{e-_\gamma}^L + N_{\pi-}^L] - [N_{e-}^R + N_{e-_\gamma}^R + N_{\pi-}^R]}{[N_{e-}^L + N_{e-_\gamma}^L + N_{\pi-}^L] + [N_{e-}^R + N_{e-_\gamma}^R + N_{\pi-}^R]} \tag{12}$$

where we have:

- $N_{e-}^{L,R}$ is the number of left, right events coming from DIS electrons
- $N_{e-_\gamma}^{L,R}$ is the number of left, right events coming from non-DIS electrons (mainly $\gamma \rightarrow e^+e^-$)
- $N_{\pi-}^{L,R}$ is the number of left, right pion events

Defining three dilution factors α_{e-}, α_{e-_γ} and $\alpha_{\pi-}$, Eq. 12 can then be written

$$A_{\perp}^{uncorr} = \alpha_{e-} \frac{[N_{e-}^L - N_{e-}^R]}{[N_{e-}^L + N_{e-}^R]} + \alpha_{e-_\gamma} \frac{[N_{e-_\gamma}^L - N_{e-_\gamma}^R]}{[N_{e-_\gamma}^L + N_{e-_\gamma}^R]} + \alpha_{\pi-} \frac{[N_{\pi-}^L - N_{\pi-}^R]}{[N_{\pi-}^L + N_{\pi-}^R]} \tag{13}$$

where the three dilution factors are defined using the inclusive cross sections σ_{e-}, $\sigma_{\pi-}$ and $\sigma_{e-\gamma}$, respectively for DIS-electrons, non-DIS electrons and pions.

$$\begin{aligned} \alpha_{e-} &= \frac{\sigma_{e-}}{\sigma_{e-}+\sigma_{e-\gamma}+\sigma_{\pi-}} \\ \alpha_{e-\gamma} &= \frac{\sigma_{e-\gamma}}{\sigma_{e-}+\sigma_{e-\gamma}+\sigma_{\pi-}} \\ \alpha_{\pi-} &= \frac{\sigma_{e-}}{\sigma_{e-}+\sigma_{e-\gamma}+\sigma_{\pi-}} \end{aligned} \tag{14}$$

Equation 13 can then be re-written to obtain Eq. 15, which gives the measured asymmetry for an electron run

$$A_{e^-}^{uncorr} = \alpha_{e-}A_{e-} + \alpha_{e_\gamma}A_{e-\gamma} + \alpha_{\pi-}A_{\pi-} \tag{15}$$

where A_{e^-}, $A_{e_\gamma^-}$ and A_{π^-} are the asymmetries for DIS- electrons, non-DIS electrons and pions respectively. Following the same reasoning as previously, the measured asymmetry for a positron run would be given by Eq. 16

$$A_{e^+}^{uncorr} = \alpha_{e^+}A_{e^+} + \alpha_{\pi^+}A_{\pi^+} \tag{16}$$

where α_{e^+} and α_{π^+} are the dilution factors for positrons and π^+'s respectively, A_{e^+} and A_{π^+} are the asymmetries for positrons and π^+'s respectively. Thus, since we have $A_{e_\gamma^-} = A_{e^+}$, we can insert the expression for A_{e+} from Eq. 16 in Eq. 15. The background contamination corrected expression for the measured asymmetry used in the E155X asymmetries code is then given by Eq. 17

$$A^{corr-bk} = \frac{1}{\alpha_{e^-}}[A_\perp^{corr-ew} - \frac{\alpha_{e_\gamma^-}}{\alpha_{e^+}}(A_{e^+} - \alpha_{\pi^+}A_{\pi^+}) - \alpha_{\pi^-}A_{\pi^-}]. \tag{17}$$

Quantitative implementation of this correction

A quantitative method was established to evaluate the number of positrons and mis-identified pions in order to subtract them from the number of measured electrons. The pion rate is very low in the 10.5° spectrometer, so only the positrons need to be subtracted from the number of measured electrons in this spectrometer. A good estimation of the number of measured electrons (positrons) is the area under the electron (positron) E/p curve in the range [0.75,2.5]. The number of pions being mis-identified as electrons can be evaluated by normalizing the area under a pion E/p curve to the pion rate in an electron E/p spectrum. To evaluate the areas under the curves mentioned above, a fit was performed on each of these curves, followed by an integration of these fits over the desired range.

The functional form used for the fit to the π^+ (π^-) E/p curve in the 2.75° and 5.5° spectrometers is given by

$$y_{\pi^{+(-)}}(x) = p_1 e^{p_2+p_3x+p_4x^2+p_5x^3}. \tag{18}$$

The fit to the pion E/p curve was first performed in the x region [0.2,2.5], to evaluate the parameters p_1, p_2, p_3, p_4 and p_5. This fit is shown in the top plot of Fig. 21. The fit y_π was then normalized to the pion rate in the electron E/p spectrum by fitting the electron E/p spectrum in the range [0.2,0.75], using the functional form in Eq. 18, but this time allowing only p_1 to vary and using the values determined from the first fit for all the other parameters. This second fit provided a new value for p_1, and is shown in the middle plot of Fig. 21.

The functional form used for the fit to the positron (electron) E/p curve in the 2.75° and 5.5° spectrometers is given by

$$y_{e^{+(-)}}(x) = y_{\pi}(x) + p_6 e^{-\frac{1}{2}\left(\frac{x-p_7}{p_8}\right)^2} + p_9 e^{-\frac{1}{2}\left(\frac{x-p_{10}}{p_{11}}\right)^2} + p_{12} e^{p_{13}+p_{14}x+p_{15}x^2+p_{16}x^3}. \quad (19)$$

The fit to the positron (electron) E/p spectrum was performed in the x range [0.75,2.5], and includes the normalized pion E/p fit (y_{π}), since the electron E/p spectrum includes pions mis-identified as electrons. This fit is shown in the bottom plot of Fig. 21.

To obtain the areas under the fitted curves, the following four integrals were then calculated for the 2.75° and 5.5° spectrometers

$$\begin{aligned} I_1 &= \int_{0.75}^{2.5} y_{\pi+}(x)dx \\ I_2 &= \int_{0.75}^{2.5} y_{\pi-}(x)dx \\ I_3 &= \int_{0.75}^{2.5} y_{e+}(x)dx \\ I_4 &= \int_{0.75}^{2.5} y_{e-}(x)dx. \end{aligned} \quad (20)$$

I_1 and I_2 are respectively equal to the number of π^+'s and π^-'s mis-identified as positrons and electrons. I_3 and I_4 are respectively equal to the number of measured positrons and electrons. The number of true positrons is then equal to (I_3 - I_1), and the number of true DIS electrons is equal [I_4 - (I_2+I_3-I_1)]. The cross-sections σ_{π^+}, $\sigma_{\pi-}$, σ_{e+} and σ_{e-} are therefore respectively proportional to I_1, I_2, (I_3-I_1) and [I_4-(I_3+I_2-I_1)]. The dilution factors for the 2.75° and 5.5° spectrometers are then

defined by:

$$\begin{aligned} \alpha_{e-} &= (I_4 - I_3 - I_2 + I_1)) \,/\, (I_4) \\ \alpha_{e-\gamma} &= (I_3 - I_1) \,/ I_4 \\ \alpha_{e+} &= (I_3 - I_1) \,/ I_3 \\ \alpha_{\pi-} &= I_2 / I_4 \\ \alpha_{\pi+} &= I_1 / I_3. \end{aligned} \tag{21}$$

We should note that the sum of these coefficients is equal to 1.

The pion contamination was negligible in the 10.5° spectrometer compared to the lower angle spectrometers, thus only one fitting function was used to subtract the positron contamination. The functional form of the fit had the following expression

$$y_{e^{+(-)}}(x) = p_1 e^{-\frac{1}{2}\left(\frac{x-p_2}{p_3}\right)^2} + p_4 e^{-\frac{1}{2}\left(\frac{x-p_5}{p_6}\right)^2}. \tag{22}$$

The areas under the positron and electron E/p spectra were then given by the integrals

$$\begin{aligned} I'_1 &= \int_{0.75}^{2.5} y_{e+}(x)dx \\ I'_2 &= \int_{0.75}^{2.5} y_{e-}(x)dx. \end{aligned} \tag{23}$$

Therefore the following expressions for the contamination dilution factors were used in the 10.5° spectrometer:

$$\begin{aligned} \alpha_{e-} &= (I'_2 - I'_1) \,/ I'_2 \\ \alpha_{e-\gamma} &= I'_1 / I_2 \\ \alpha_{e+} &= 1 \\ \alpha_{\pi-} &= 0 \\ \alpha_{\pi+} &= 0. \end{aligned} \tag{24}$$

Results of this correction

The coefficients α_{π^-} and α_{π^+} are plotted versus bin number for the proton target at electron beam energies of 29 GeV and 32 GeV data in Fig. 22. The dilution coefficient α_{π^-} decreases with increasing x which reflects the decrease in the pion rate with increasing momentum. The α_{π^+} coefficient on the other hand increases with increasing x, reflecting an increase of the pion contamination with increasing x for positron runs which happens because the positron rate falls even more rapidly with increasing momentum. The coefficients α_{e+} and α_{e-} are plotted versus bin number for the proton target at electron beam energies of 29 GeV and 32 GeV data in Fig. 23. The bins are defined in Table 11 in Appendix A. We would expect to see smooth distributions for these coefficients. However, a combination of statistics and peculiarities of the fitting can cause this scatter. The final correction is unaffected by this scatter though since these coefficients are so small. Tables 7 and 8 give the values for the average asymmetries $A_{\pi-}$, $A_{\pi+}$ and A_{e+} used in Eq. 17 for this correction. The number of positron runs collected was insufficient to determine an asymmetry with small enough error bars to distinguish it from zero. Therefore, A_{e^+} was taken to be zero in all spectrometers. The average pion asymmetries A_{π^-} and A_{π^+} were determined by fitting a straight line through the asymmetry for each bin as can be seen in Figs. 24 and 25. The error on these fits is also given in these figures. We can note that A_{π^-} is significantly negative for the 2.75° spectrometer at both beam energies of 29 and 32 GeV. Since the pion rate in the 10.5° spectrometer is very low, the asymmetries A_{π^-} and A_{π^+} were also taken

	$A_{\pi-}$	$A_{\pi+}$	A_{e+}
2.75°	-0.011	0.005	0.000
5.5°	-0.008	0.017	0.000
10.5°	0.000	0.000	0.000

Table 7: Average asymmetries used in equation 17 for the proton target at electron beam energy of 29 GeV

	$A_{\pi-}$	$A_{\pi+}$	A_{e+}
2.75°	-0.006	-0.001	0.000
5.5°	-0.002	-0.006	0.000
10.5°	0.000	0.000	0.000

Table 8: Average asymmetries used in equation 17 for the proton target at electron beam energy of 32 GeV

to be zero in the 10.5° spectrometer. Figure 26 shows the effect of the background subtraction via Eq. 17 on the results at electron beam energy of 29 GeV. This correction is on the order of 1%, and its effect is practically invisible on the plot. The corrections at electron beam energy of 32 GeV were also small.

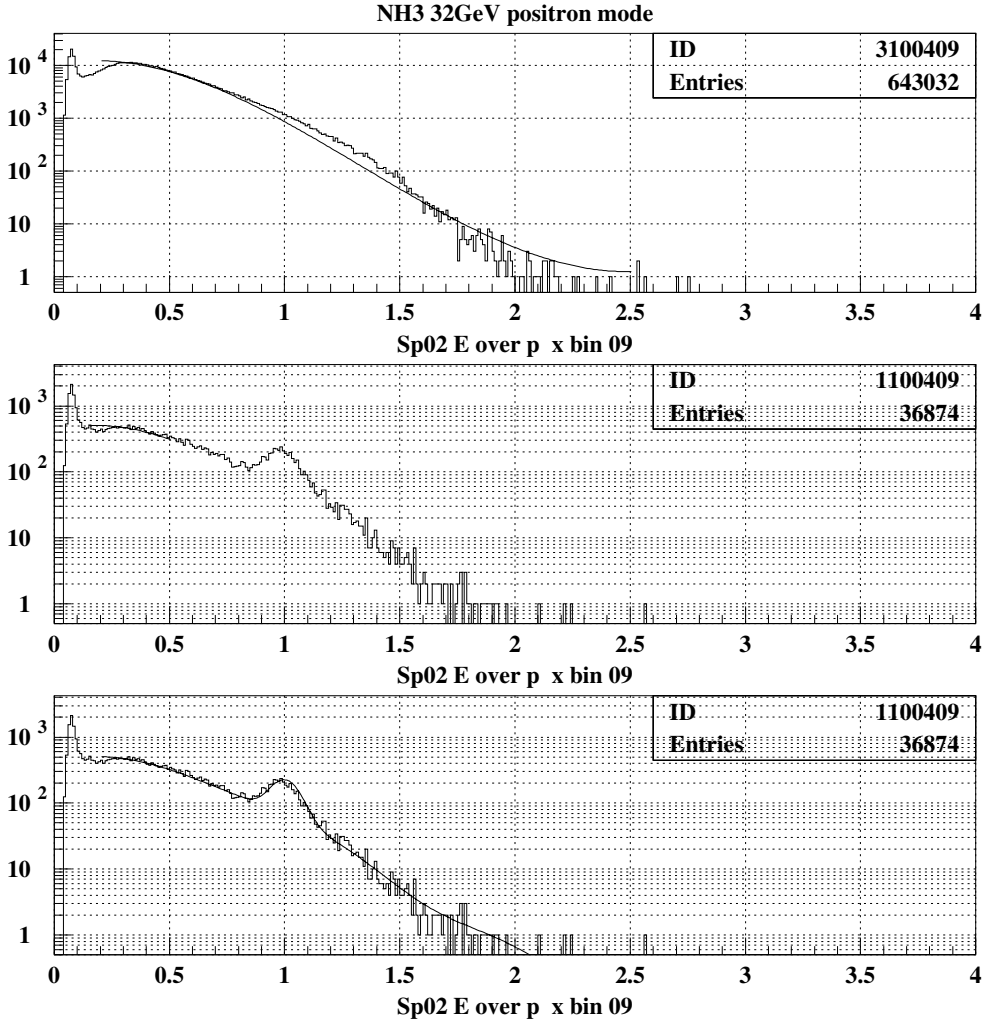

Figure 21: Example of fits used for the pion/positron correction using data from the proton target at electron beam energy of 32 GeV counts files for bin 9. Histograms were added together to increase statistics. The top plot is showing a fit (y_{π^+}) to the pion E/p distribution for positron runs. The middle plot shows a normalization of the fit from the top plot to pion rate in a positron E/p spectrum. The bottom plot shows a fit (y_{e^+}) to the positron E/p spectrum.

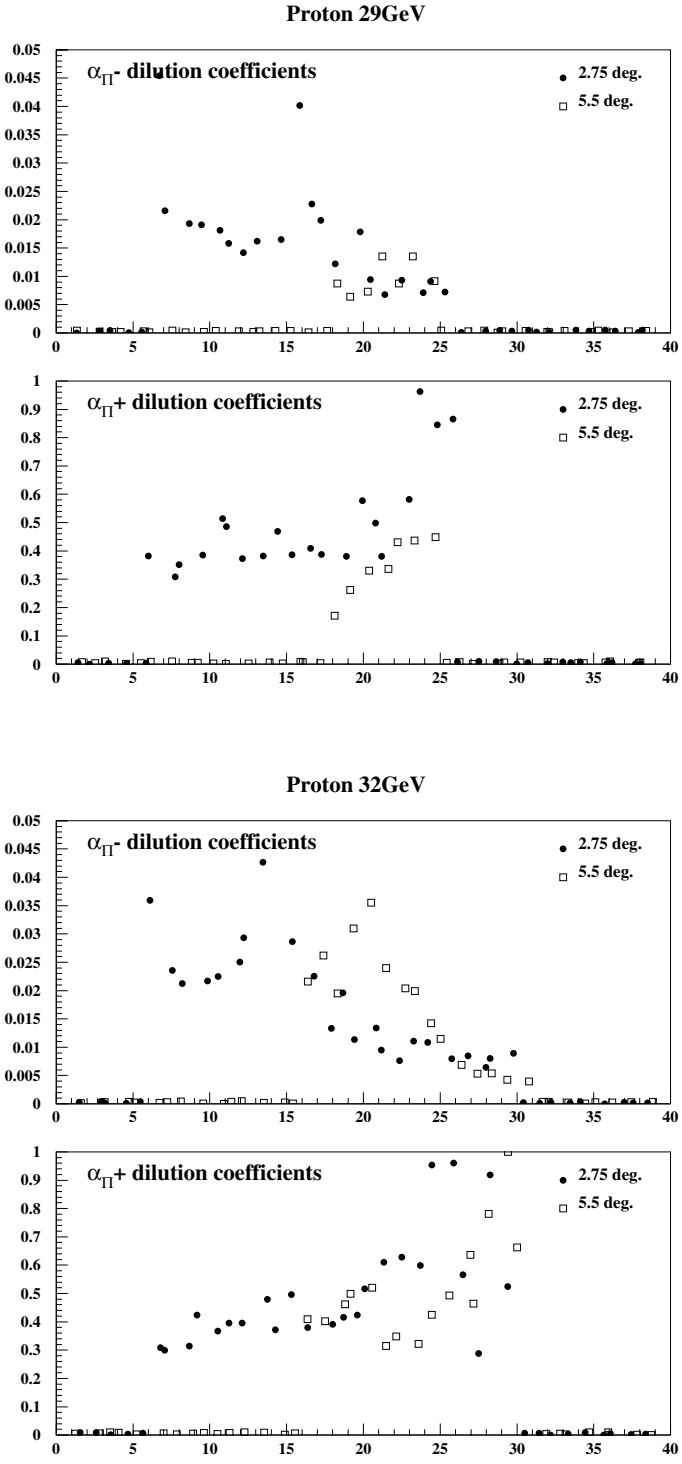

Figure 22: Dilution coefficient α_{π^-} and α_{π^+} and vs. bin number for the proton target at electron beam energies of 29 and 32 GeV.

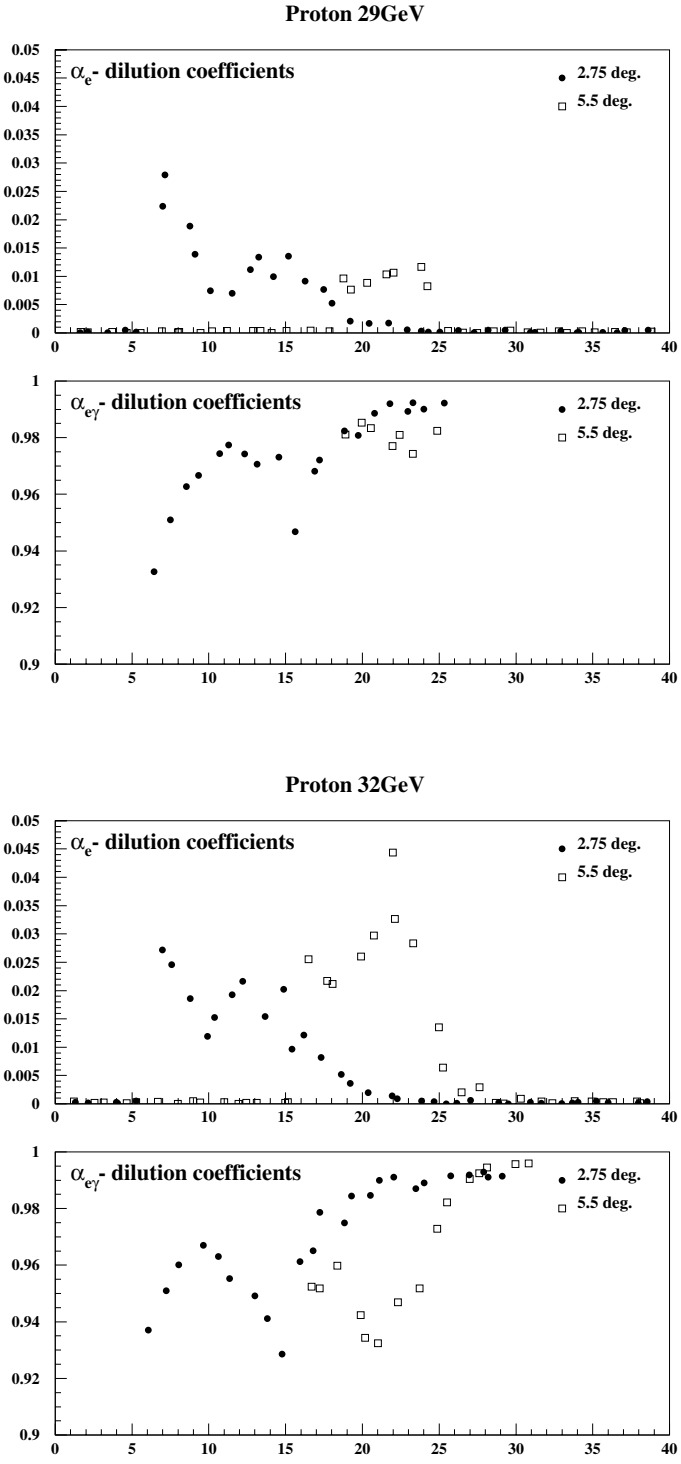

Figure 23: Dilution coefficient α_{e-} and α_{e-_γ} vs. bin number for the proton target at electron beam energies of 29 and 32 GeV.

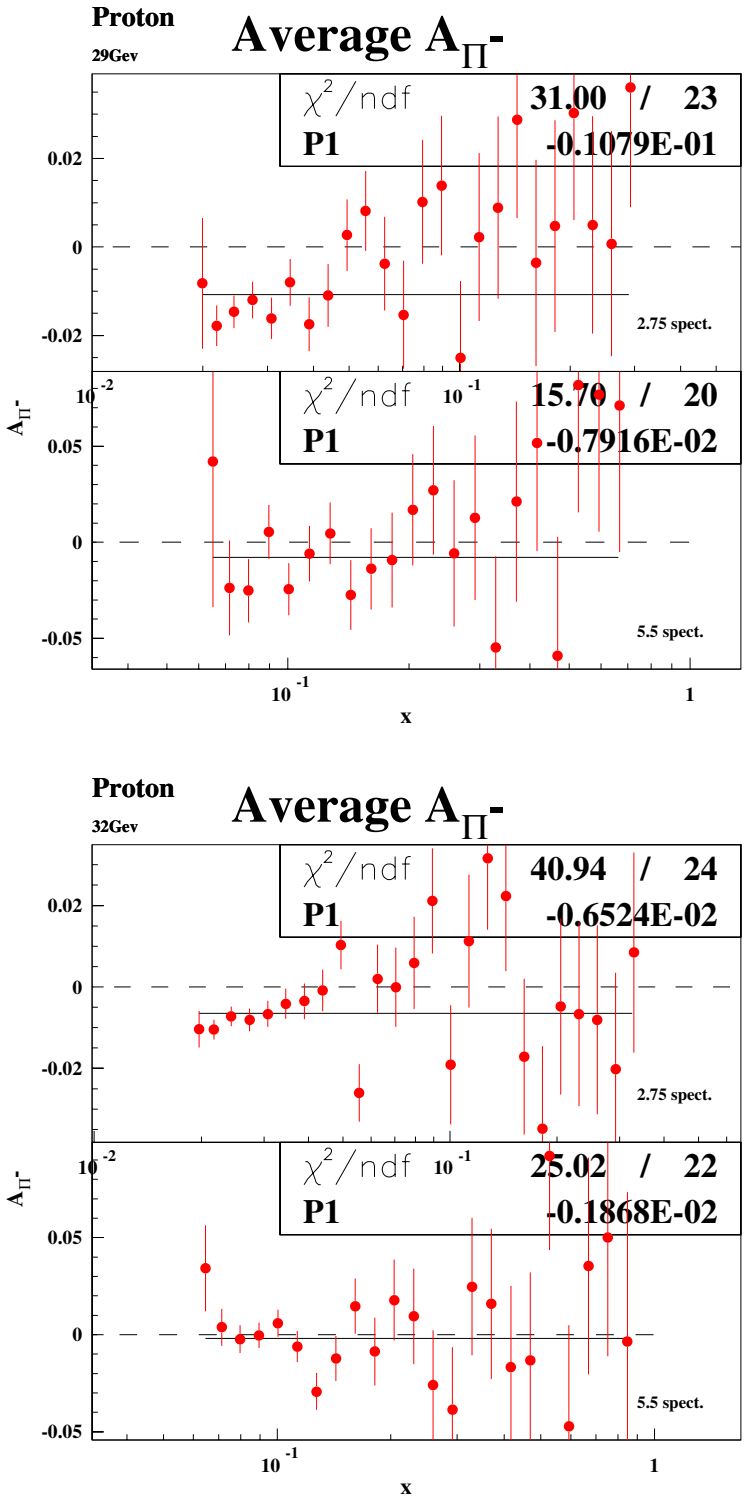

Figure 24: Average pion asymmetry over all bins for the proton target at electron beam energies of 29 and 32 GeV. A straight line is fitted through the data in each case to determine the average of the points. This average is given by the coefficient P1.

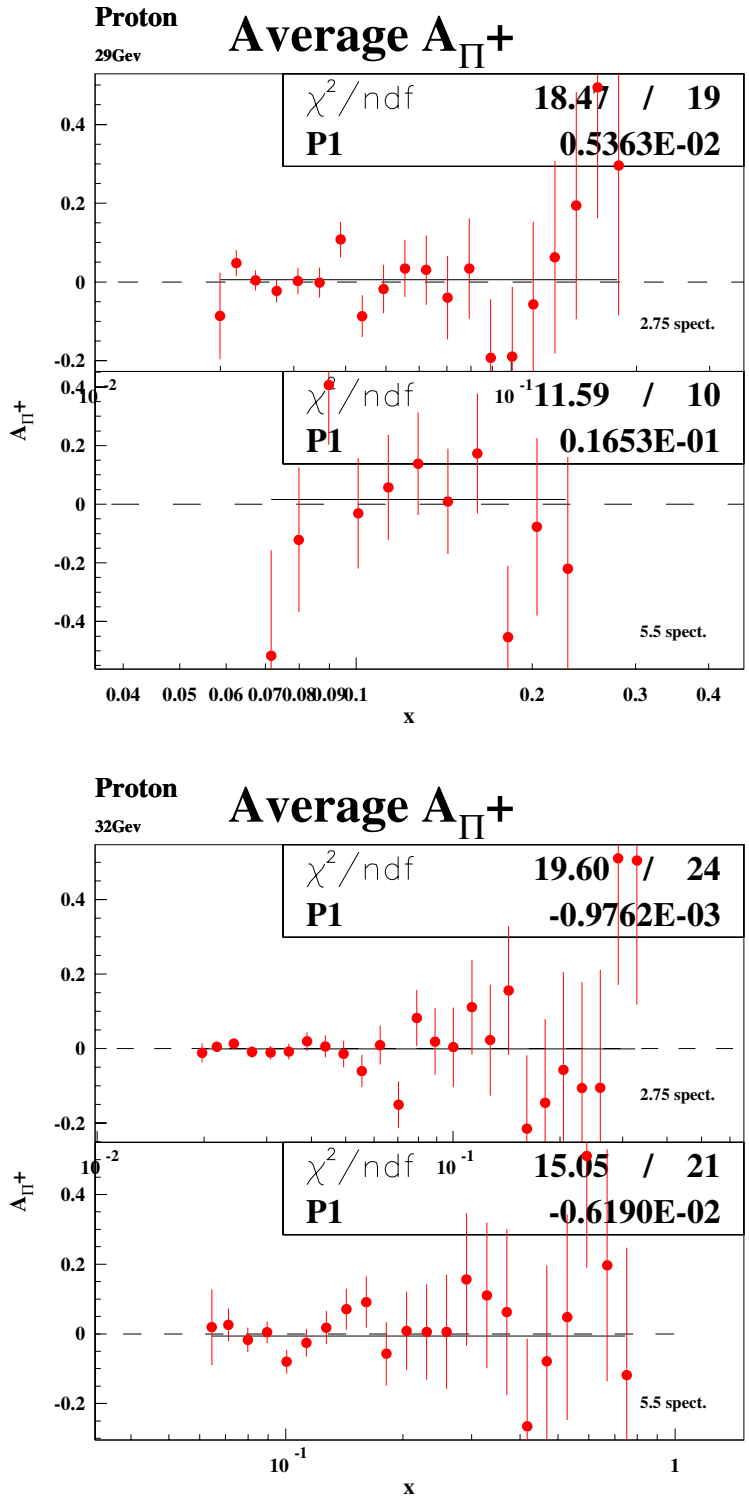

Figure 25: Average π^+ asymmetry over all bins for the proton target at electron beam energies of 29 and 32 GeV.

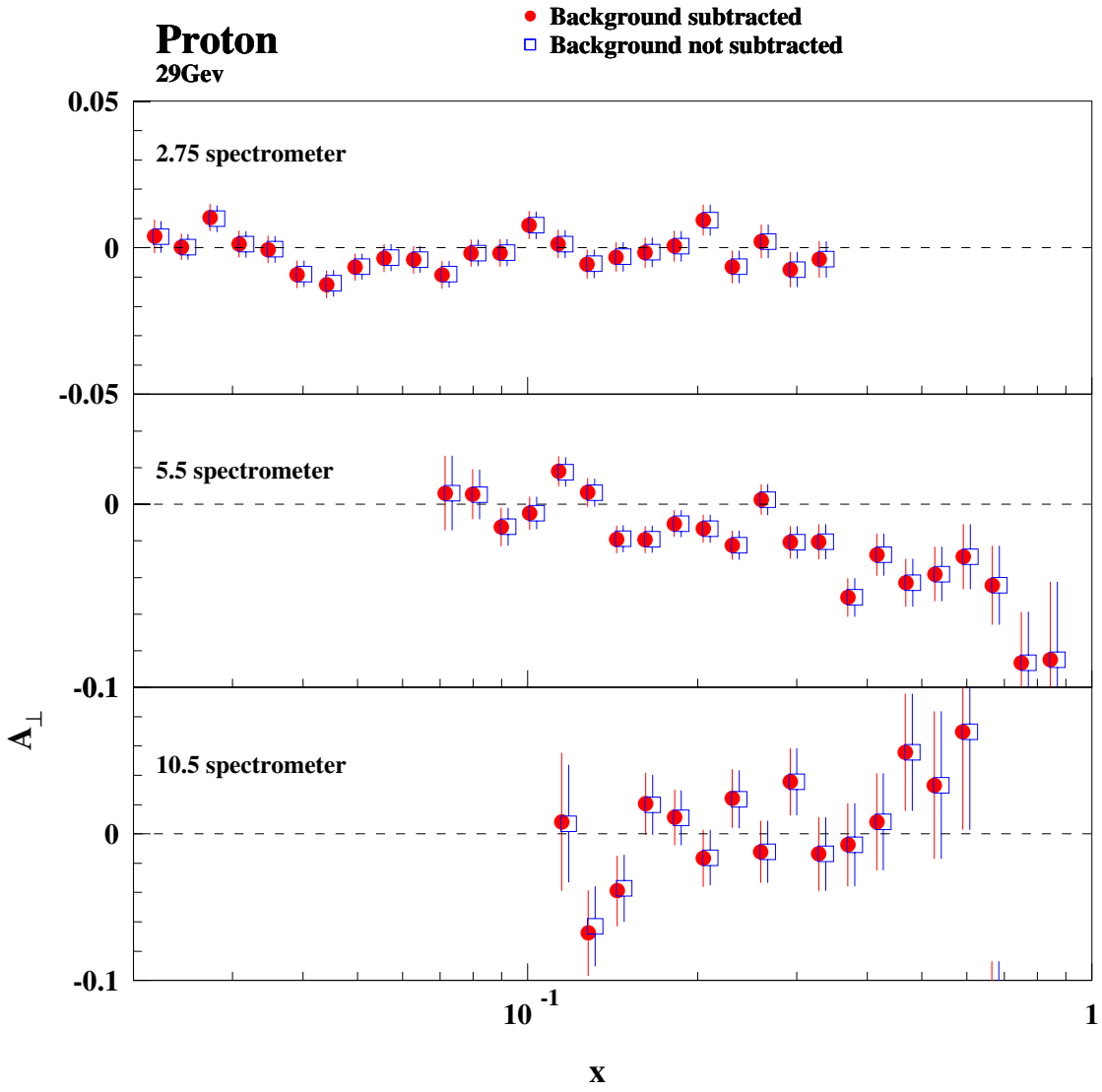

Figure 26: Comparison of $A_\perp$ with and without the background subtracted. The electroweak asymmetry correction has already been applied for these results in both cases.

4.5.3 Radiative Corrections

The asymmetry A_{meas} in Eq. 16 in Sec. 1.1, is the measured asymmetry of the spin dependent single photon exchange Born-level process seen in Fig. 1. However, the experimental asymmetry receives contributions from higher order processes known as radiative corrections, such as those shown in Fig. 27. Radiative corrections are generally separated into internal and external corrections. The internal radiative effects occur within the nuclear field of the scattering nucleon, and include processes calculated to order α^3 (electromagnetic coupling constant) such as bremsstrahlung, vertex corrections and vacuum polarization. The external radiative effects arise from the presence of other nuclei, and are dominated by bremsstrahlung radiation energy losses as the electrons traverse additional target material both before and after the scattering process. The total amount of target material in the path of the detected electrons corresponds to only about 0.05 radiation lengths, thus the external corrections generally account for only half of the total correction.

The internal corrections were applied to the measured asymmetries through the expression

$$A_{int} = \frac{\sigma^p_{int}}{\sigma^u_{int}} = \frac{\sigma^p_{Born}(1+\delta_{\rm V}) + \sigma^p_{el} + \sigma^p_{inel}}{\sigma^u_{Born}(1+\delta_{\rm V}) + \sigma^u_{el} + \sigma^u_{inel}} \tag{25}$$

where the p and u superscripts differentiate polarized and unpolarized cross sections and $\delta_{\rm V}$ denotes the vertex corrections. Contributions from internal bremsstrahlung are given by the σ_{el} and σ_{inel} terms. The fully radiated cross sections are then expressed as convolutions of the internally radiated cross sections (σ^p_{int} and σ^u_{int})

with the external bremsstrahlung energy loss probabilities for traversing material before and after the primary scattering event. These fully radiated cross sections (external and internal radiations), along with the Born cross sections form the single additive radiative correction:

$$\Delta A^{RC} = A_{Born} - A_{rad} = \frac{\sigma^{p}_{Born}}{\sigma^{u}_{Born}} - \frac{\sigma^{p}_{rad}}{\sigma^{u}_{rad}} \tag{26}$$

where A_{rad} is the experimental asymmetry which includes radiative effects. The Born asymmetry, A_{Born}, is unknown, and our goal is to extract it from the data. An itterative process is used that begins with a fit to the measured data from E155X which then served as an input model in the code which calculates the radiative corrections. This code is known as RCSLACPOL and is described in Reference [77]. If the input model for A_{Born} is not equal to the radiatively corrected asymmetry ($A_{rad} + \Delta A^{RC}$), a new fit to the corrected data is performed and is used as a new input model for A_{Born}. This procedure is iterated until the input model and the corrected data converge to better than 1% .

This additive correction ΔA^{RC} is sufficient to correct the measured values, but does not reflect the influence the radiative corrections have on the statistical uncertainty of the extracted results. The statistical uncertainty on the radiated asymmetry measured (A^{rad}) is directly related to the unpolarized cross section σ^{u}_{rad}. By extracting σ^{u}_{Born}, a statistical uncertainty can then be assigned to A_{Born}, which was achieved by splitting the single additive correction ΔA^{RC} into an additive term and a multiplicative term that affects the uncertainty as well. The multiplicative

term is known as the radiative dilution factor, f_{RC}, and is defined by

$$f_{RC} = \frac{\sigma_{rad}^{unpol} - \sigma_{tail}^{unpol}}{\sigma_{rad}^{unpol}} \tag{27}$$

where σ_{rad}^{unpol} is the radiated unpolarized cross-section and σ_{tail}^{unpol} refers to the additional unpolarized events beyond the unpolarized Born cross-section. For E155X only the elastic tail was included in the the definition of σ_{tail}^{unpol}. The single additive correction is related to the radiative dilution factor, f_{RC}, and to the additive radiative correction, A_{RC} by

$$\Delta A^{RC} = \left(\frac{1}{f_{RC}} - 1 \right) A_{rad} + A_{RC}. \tag{28}$$

The factor f_{RC} changes the effective number of events in a given bin and A_{RC} changes the effective asymmetry. Using the measured asymmetry discussed in the previous section, $A_{\perp}^{corr-bk}$, the physics asymmetry $A_{\perp}$ is then given by

$$A_{\perp} = \frac{1}{f_{RC}} A_{\perp}^{corr-bk} + A_{RC}. \tag{29}$$

Figure 28 shows a comparison of the measured asymmetry with and without radiative corrections applied. The radiative corrections tend to shift the data points in the 2.75° and 10.5° spectrometers to lower values. In the 5.5° spectrometer the data points are shifted to higher values. The radiative corrections also tend to increase the uncertainty on the extracted results, and for E155X they increased by about 4%.

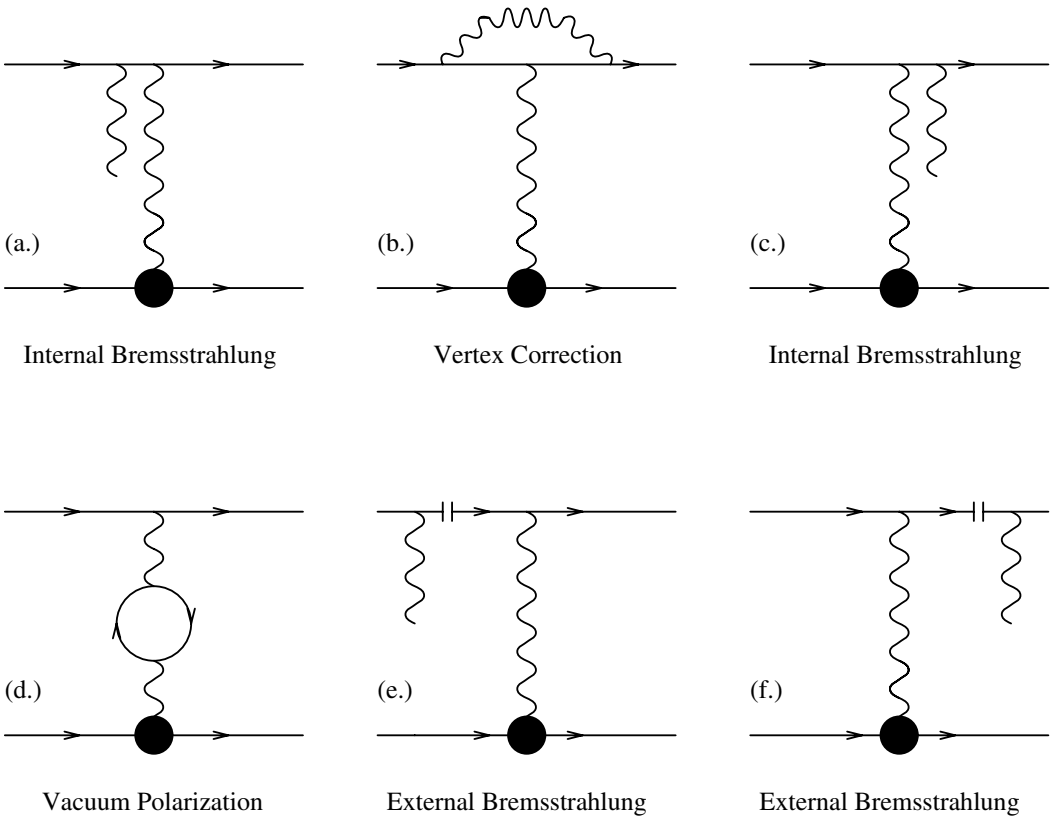

Figure 27: Feynman diagrams for internal and external processes considered in radiative corrections.

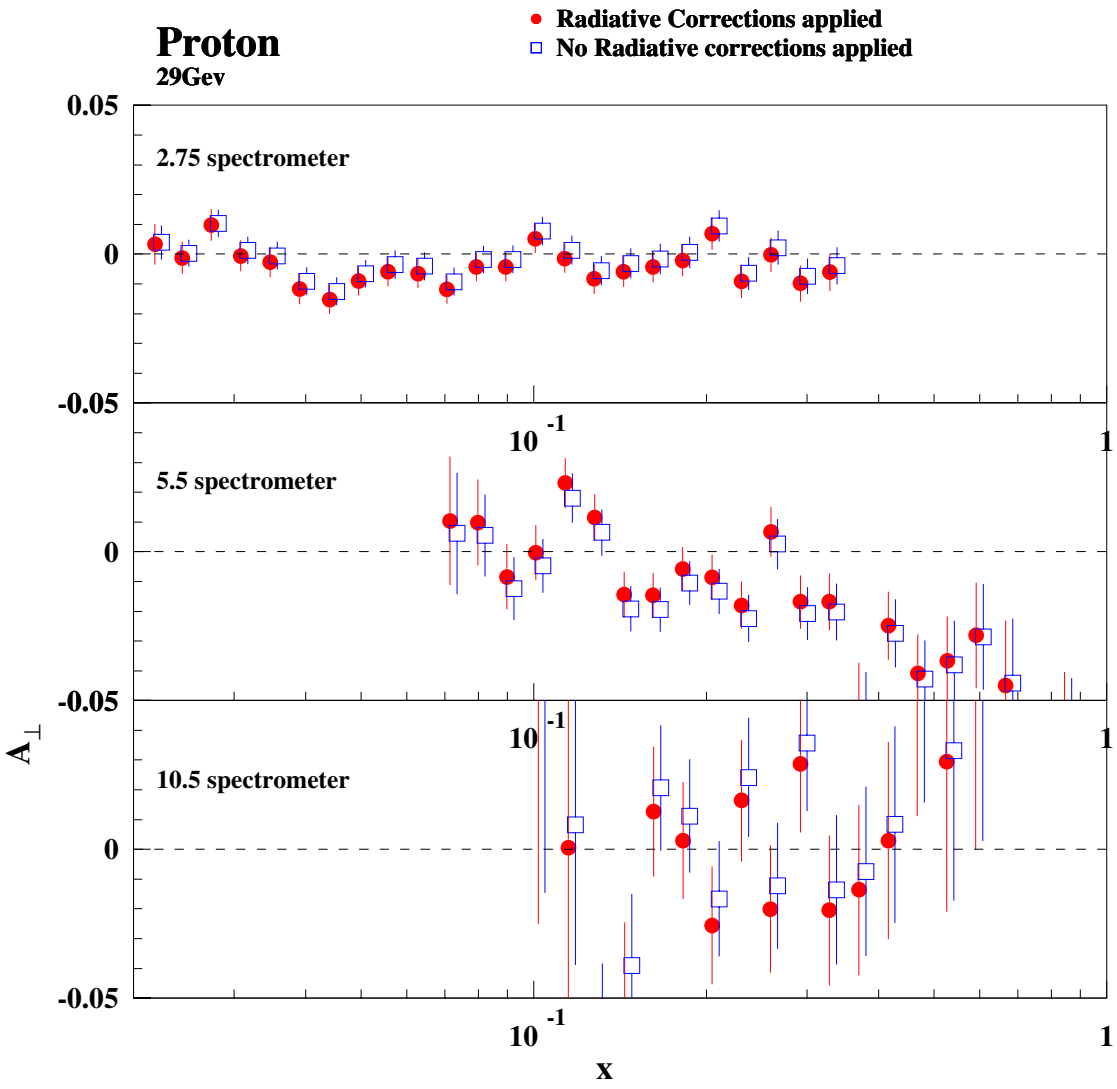

Figure 28: Comparison of $A_\perp$ results with and without radiative corrections applied to the measured asymmetry. The electroweak asymmetry correction and the background correction have already been applied in both cases.

4.6 Check for False Asymmetries

A check was performed to try to identify any additional false asymmetries that would contaminate $A_\perp$. Such false asymmetries could include helicity-dependent effects which would produce a difference in the average $A_\perp$. The proton data were therefore separated into independent sets by energy and target enhancement. Figure 29 shows that the average asymmetries for each category are consistent within the measurement's precision, which would indicate that there are no additional false asymmetries contaminating the $A_\perp$.

4.7 Target Field Angle Correction

The preliminary results from the analysis showed an unusual Q^2-dependence of g_2 suggestive of a systematic effect. An investigation of this revealed that the target orientation was not at 90° from the beam line as expected, but was actually slightly rotated with respect to the true perpendicular. When the target was installed for E155X, old SLAC survey positions (from 1993) for the four tooling balls, A, B, C and D as seen in Fig. 30, were used, rather than the new values available from the Thomas Jefferson National Accelerator Facility (Jlab). The Jlab measurements were made after repairs were performed on the target system to fix the damage caused by an accident before the target was shipped back to SLAC for experiment E155X. Comparing the two sets of numbers, there is a rotation of 2.4° (this is the average of the four tooling ball values, which range from 2.2° to 2.6° angular rotation, assuming no centroid difference). Reference [78] describes the details of

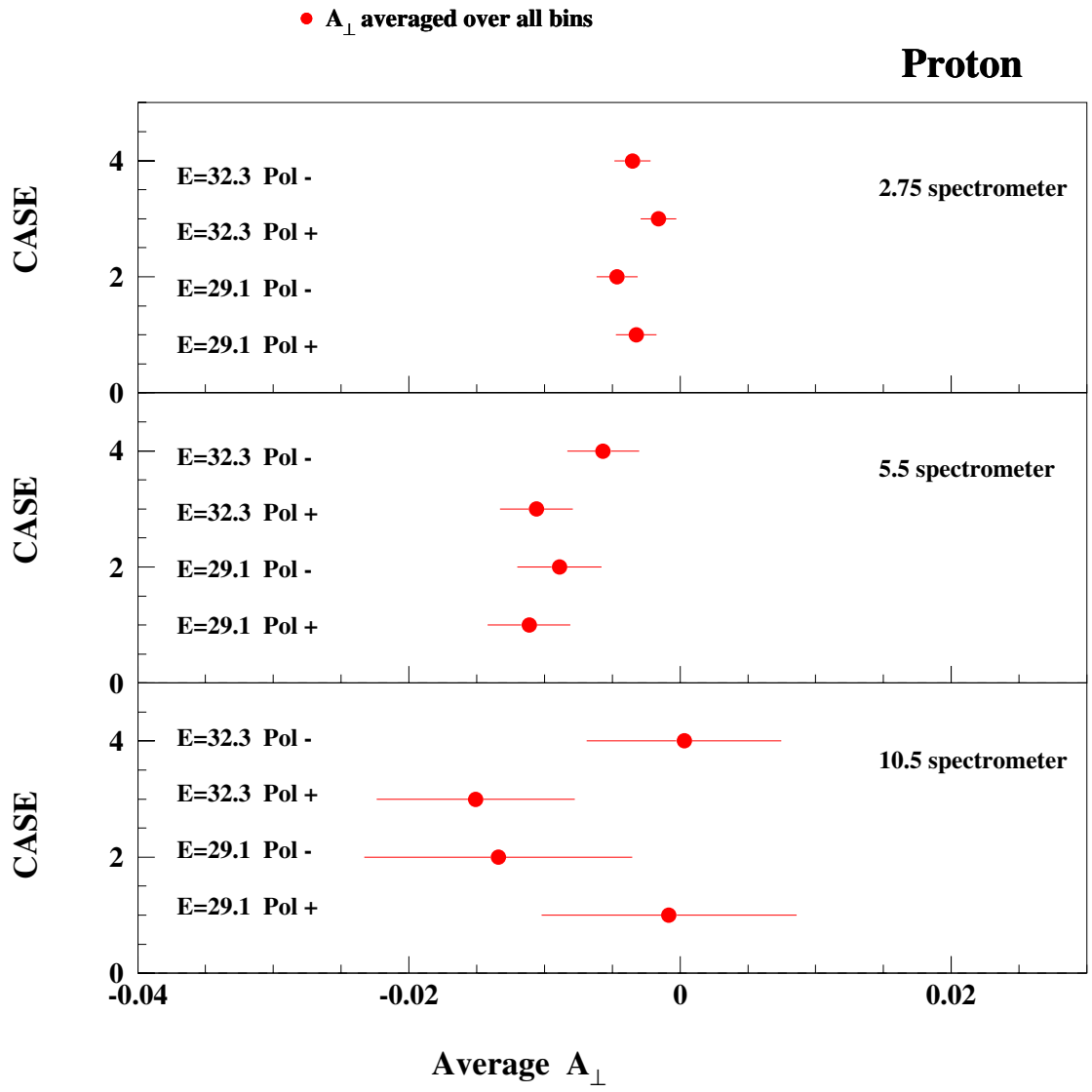

Figure 29: Average $A_\perp$ over all bins for the Proton data, separated into four different cases by energy and target polarization. The energies are given in GeV, Pol - and Pol + respectively mean negative target polarization and positive polarization.

these measurements and calculations. Since measurements performed at Jlab show that the magnetic field is lined up with the Jlab tooling ball values to within 0.1°, the magnetic field in E155X was oriented at 92.4° anti-clockwise. In other words, in addition to the main component pointing north, there is an additional component pointing west. This means that $\cos(\alpha)$ =-0.042 in Eq. 16 in Sec. 1.1. Figure 30 shows an illustration of the target rotation. Figure 31 shows the effect on xg_2 of the target angle correction for the data collected at incident beam energy of 29 GeV. The effect is similar at incident beam energy of 32 GeV. This correction shifts the data points in the 2.75° and 10.5° spectrometers to higher values, while it shifts the points in the 5.5° spectrometer to lower values.

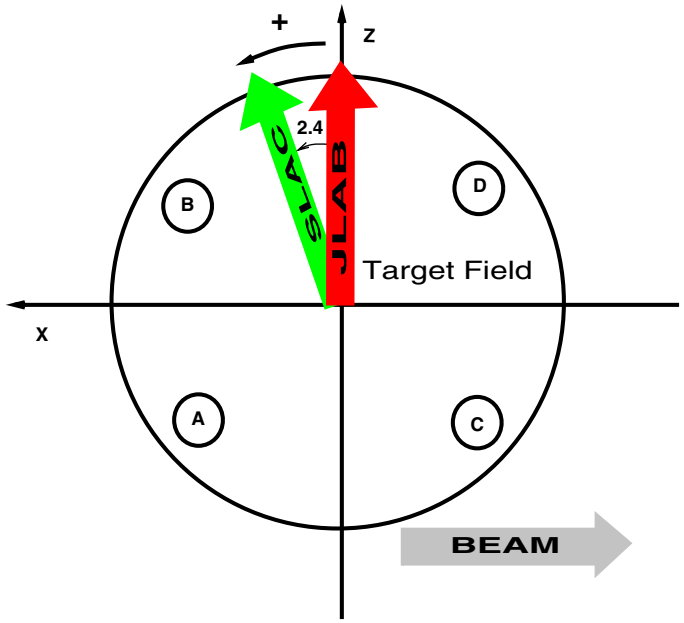

Figure 30: Target field direction at JLAB and at SLAC in the surveyors coordinate system.

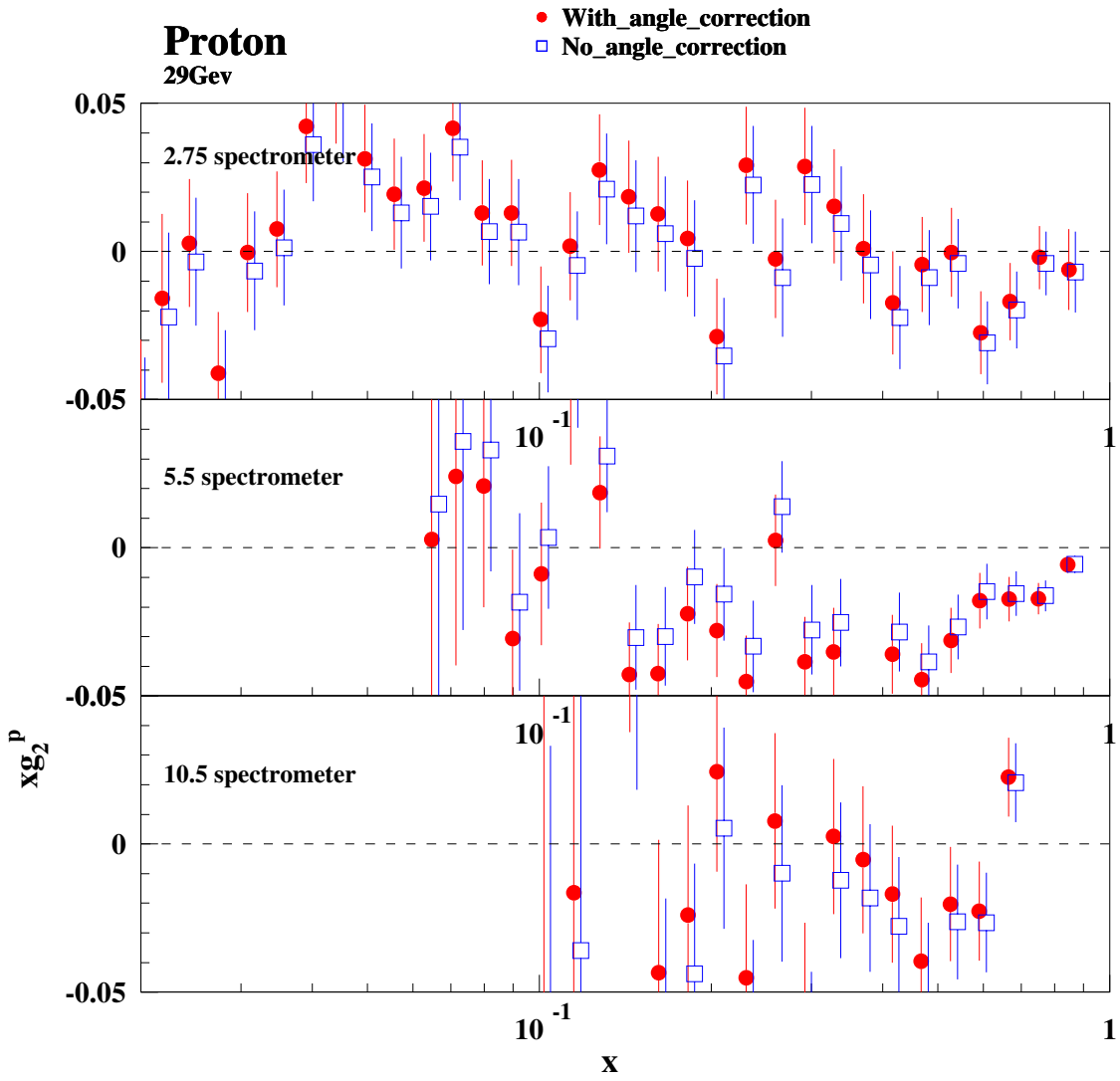

Figure 31: Comparison of xg_2 before and after the target angle correction was applied.

4.8 Systematic uncertainties

An estimate on the systematic uncertainties of the measured asymmetry was determined by taking into account the known dominant contributions. The largest contributions to the systematic uncertainties come from the beam polarization [68], the target polarization [69] and the dilution factor [70]. The systematic uncertainties for these quantities are given in Table 9 for the proton target. The systematic uncertainty on the dilution factor varies by bin, but this variation is very small. Combining the known dominant uncertainties we obtain a fractional uncertainty on $A_\perp$ of about 5.2%. The systematic uncertainties associated with the radiative corrections have not been included in these calculations because they are currently unavailable. A reasonable expectation for these uncertainties would be that they are smaller than the contributions above.

The systematic uncertainties on g_2 were obtained by propagating the systematic uncertainty on the asymmetry. The expression for g_2 can be separated into two terms

$$g_2 = K_1 F_1 A_\perp + K_2 g_1 \tag{30}$$

where K_1 and K_2 contain terms which are treated as constant in the propagation of errors. The relative sizes of the two terms in Eq. 30 was studied, and it was found that the first term is larger. We therefore neglect the second term in the propagation of errors. The fractional uncertainty on F_1 was studied by previous experiments [41] and found to be small compared to the fractional uncertainty on the asymmetry,

Quantity	Value
Beam polarization: $\delta P_B/P_B$	0.037
Target polarization: $\delta P_T/P_T$	0.017
Dilution factor: $\delta f/f$	0.030-0.035

Table 9: Dominant systematic uncertainties in the asymmetry measurement.

and is therefore neglected as well. The systematic uncertainties are shown in the tables of results in Appendix C.

CHAPTER 5

Results

Two separate data analyses were performed for E155X, one by the graduate students (referred to as the student analysis), and the other led by Prof. P. Bosted (referred to as the Bosted analysis). Chapter 4 described the student analysis, and the results of this analysis are presented in this chapter and compared to the Bosted analysis. First, the results for the measured asymmetry are given by energy and spectrometer for the proton target in 38 bins, known as the fine bins (see Table 11). This is followed by the results for g_2 and A_2 which are compared to the theoretical predictions. The Q^2-dependence of g_2 is then presented. Finally, the experimental results for the BC and ELT integrals described in Sec. 2.2.3, and the twist-3 matrix element d_2 are given.

5.1 Measured Asymmetry Results

The final values obtained for the measured asymmetry after all corrections have been applied are plotted in Figs. 32 and 33. In the 2.75° and 5.5° spectrometers, most of the asymmetry data points are inconsistent with zero, while in the 10.5° spectrometer they are consistent with zero. The 5.5° spectrometer was expected to have the most sensitivity based on a simulation performed prior to the run, and this expectation is

reflected by the results. Figure 34 shows a comparison of the asymmetry results at incident beam energies of 29 GeV and 32 GeV. The asymmetry results for the two energies are consistent with each other. The statistical error bars for the 32 GeV are smaller because more data was collected for the proton at this energy.

These results are compared to those from the independent analysis performed by P. Bosted in Figs. 35 and 36. We emphasize here again that although the measured asymmetry is referred to as $A_\perp$, it contains a small parallel component since the target polarization direction was at angle of 92.4° from the beam direction instead of 90°. The Bosted and student's results agree quite well, which is a good indication that the analyses were performed accurately.

In Appendix A, Tables 13, 14 and 15 list the values obtained for the measured asymmetry in the fine bins for the 2.75°, 5.5° and 10.5° spectrometers, respectively at electron beam energy 29 GeV. Tables 16, 17 and 18 list the values obtained for the measured asymmetry in the fine bins for the 2.75°, 5.5° and 10.5° spectrometers, respectively at electron beam energy 32 GeV. The x range of the fine bins is shown in Table 11. Asymmetry results without radiative corrections are given in Appendix B. Tables 19, 20 and 21 list the values obtained for the measured asymmetry without radiative corrections, in the fine bins, for the 2.75°, 5.5° and 10.5° spectrometers, respectively at beam energy 29 GeV. Tables 22, 23 and 24 list the values obtained for the measured asymmetry without radiative corrections, in the fine bins, for the 2.75°, 5.5° and 10.5° spectrometers, respectively at beam energy 32 GeV.

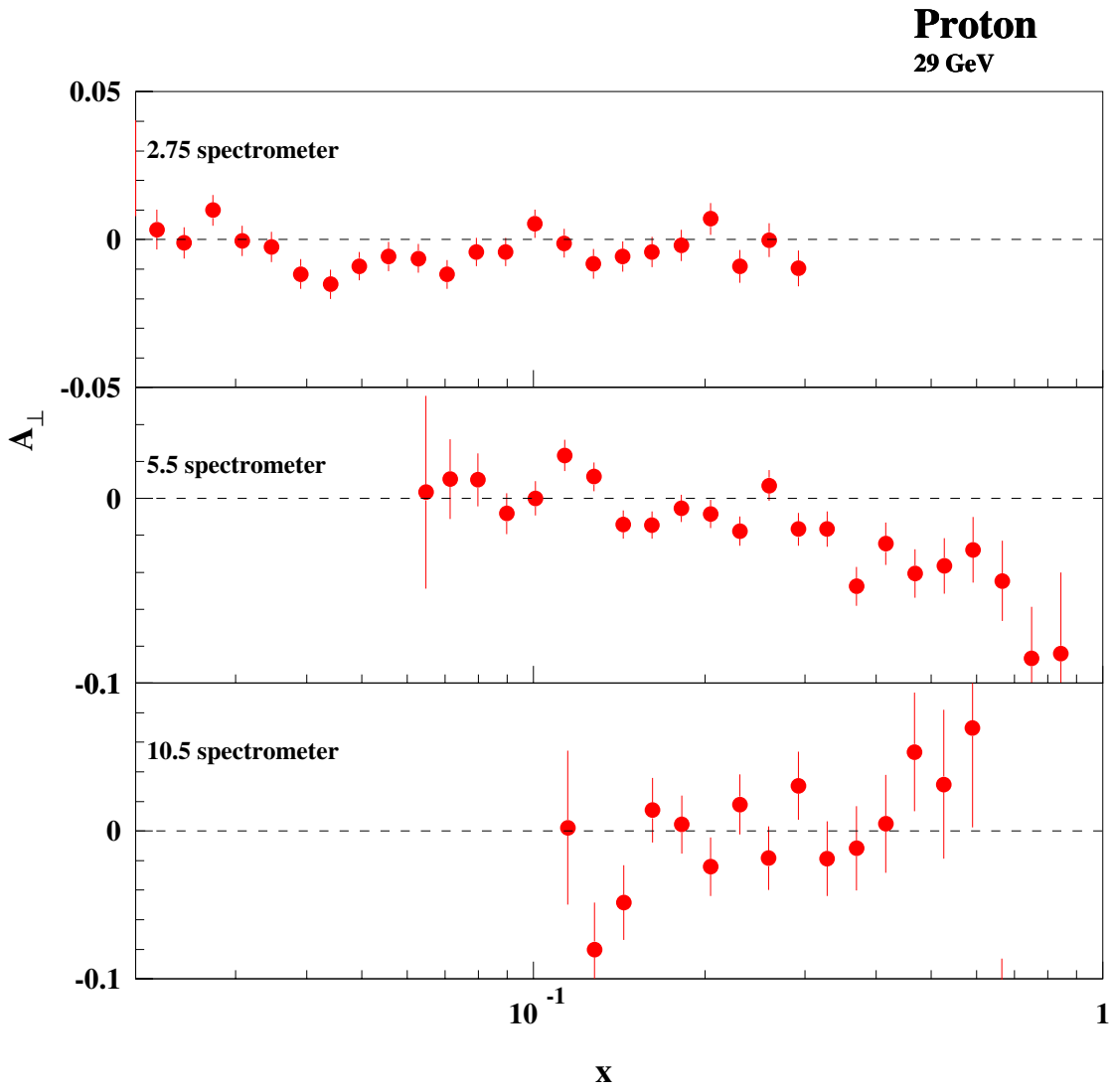

Figure 32: Final measured asymmetry results for the proton at beam energy of 29 GeV. Although referred to as $A_\perp$, this asymmetry contains a small parallel component since the target polarization direction was actually at an angle of 92.4° instead of 90°.

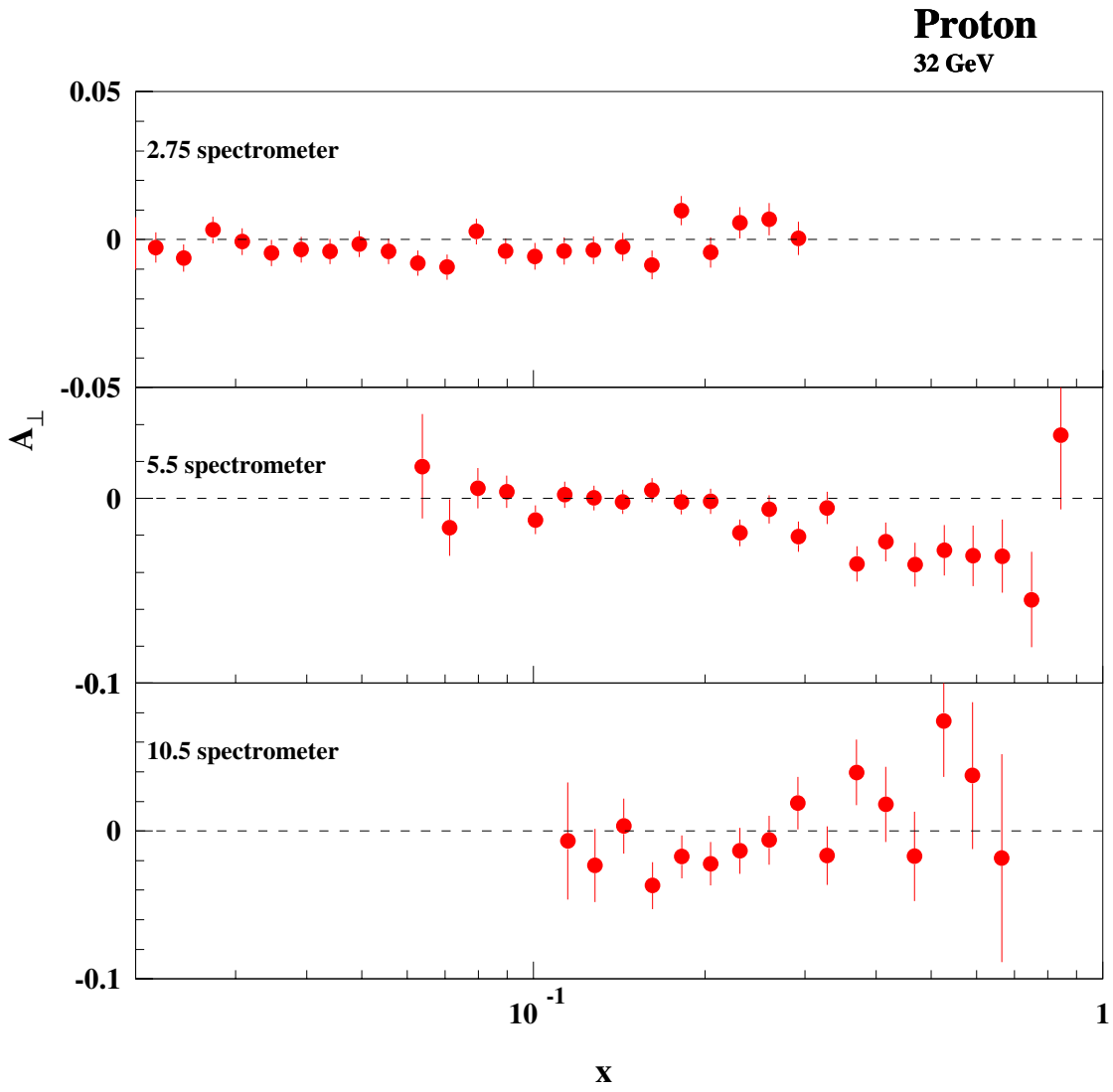

Figure 33: Final measured asymmetry results for the proton at beam energy of 32 GeV. This asymmetry contains a small parallel component since the target polarization direction was actually at an angle of 92.4° instead of 90°.

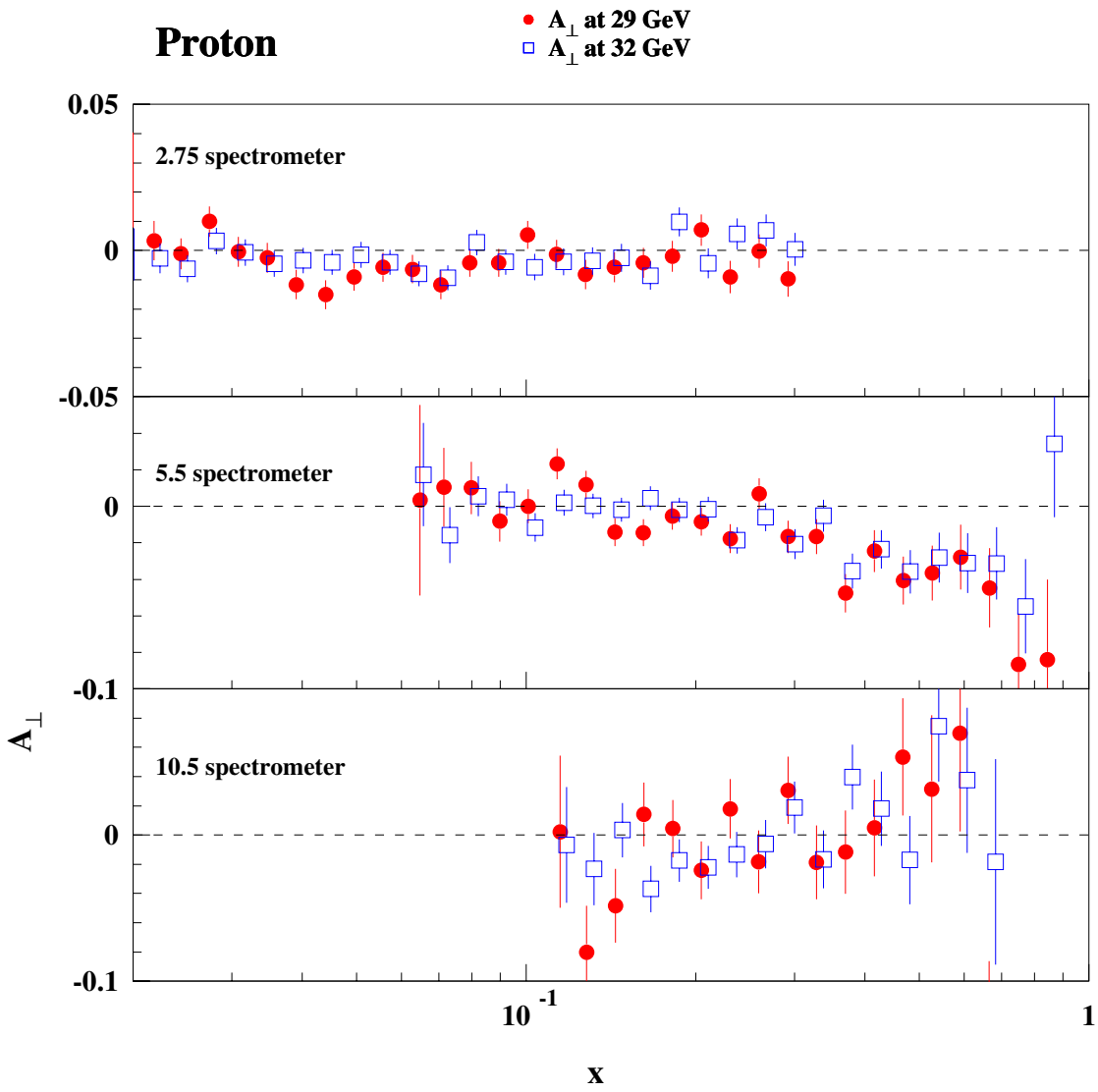

Figure 34: Comparison of the final measured asymmetry results for the proton at electron beam energies of 29 GeV and 32 GeV.

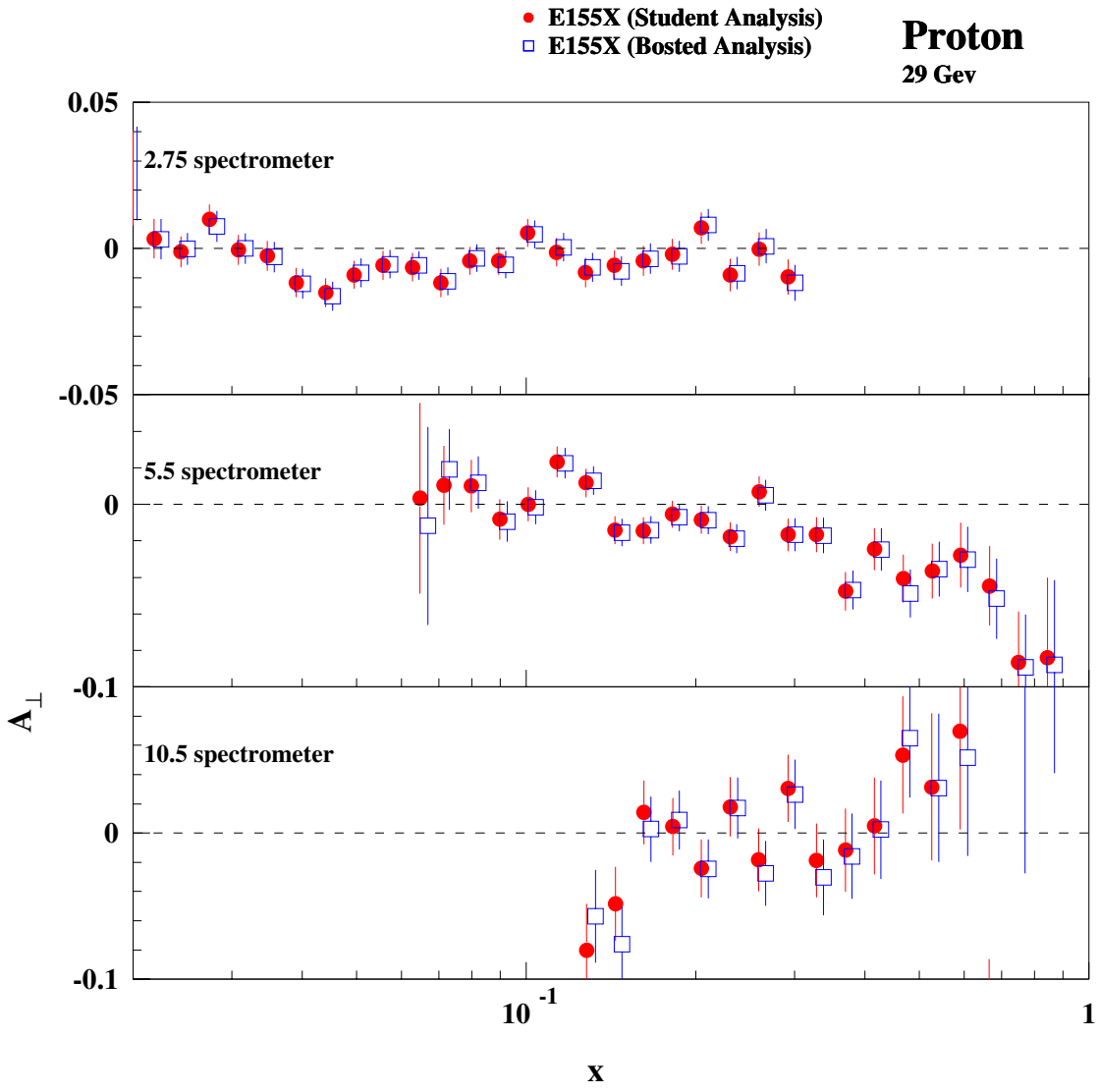

Figure 35: Comparison of measured asymmetry results from the Student analysis and the Bosted analysis for the Proton target at electron beam energy of 29 GeV.

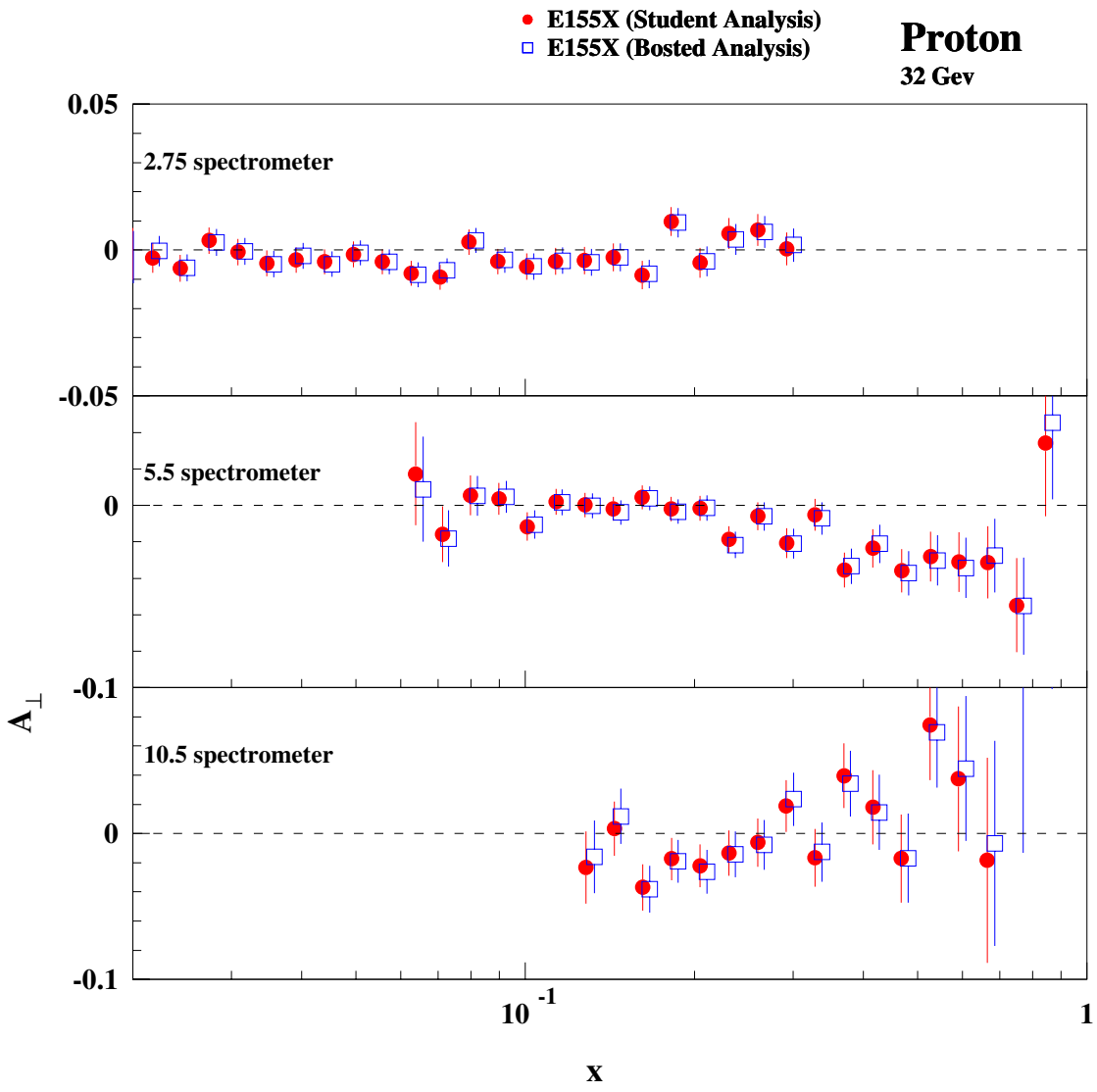

Figure 36: Comparison of measured asymmetry results from the Student analysis and the Bosted analysis for the proton target at electron beam energy of 32 GeV.

5.2 g_2 Results

Once the measured asymmetry (A_{meas}, also referred to as $A_\perp$ on the plots) has been determined, results for g_2 were obtained using

$$g_2 = \frac{yF_1}{2E'(\cos(\Theta) - \cos(\alpha))}\left[A_{meas}\nu\frac{(1+\epsilon R)}{1-\epsilon} - \frac{g_1}{F_1}(E\cos(\alpha) + E'\cos(\Theta))\right] \quad (1)$$

where the parameters are described in Sec. 1.1. The E155 phenomenological fit to g_1/F_1 [8] is used. This fit is given by

$$\frac{g_1(x,Q^2)}{F_1(x,Q^2)} = x^{0.7} \times (0.82 + 1.01x - 1.49x^2) \times \left(1 - \frac{0.037}{Q^2}\right). \quad (2)$$

The function F_1 was obtained from the NMC fit to $F_2(x,Q^2)$ [79]. The SLAC fit to $R(x,Q^2)$ [80] is used. Figure 37 shows results for g_2 for the proton after combining the data for both energies by taking a weighted average, with no attempt to evolve the data versus Q^2. Figures 38 and 39 show the results for g_2 separated by energy. There are no significant differences between the results for the two energies. Tables 25, 26 and 27 in Appendix C contain the results for xg_2 at electron beam energy of 29 GeV, for the 2.75° , 5.5° and 10.5° spectrometers, respectively. Tables 28, 29 and 30 in Appendix C contain the results for xg_2 at electron beam energy of 32 GeV, for the 2.75° , 5.5° and 10.5° spectrometers, respectively.

A more interesting result to look at is xg_2, which is plotted in Fig. 40 where the data for both electron beam energies have been combined by taking a weighted average. It should be noted that the different behaviors for g_2^{WW} for the three spectrometers come from the well-known Q^2 dependence of g_1. The g_2 results approximately follow the behavior of g_2^{WW}. Figures 41 and 42 show the results obtained for

xg_2 for the proton, separated by energy. Once again there is no significant difference between the two energies.

The results for g_2 combined for all three spectrometers are shown in Fig. 43. A clearer picture of the behavior of the function g_2 can be achieved by plotting xg_2 versus x which is shown in Fig. 44. The fine bins can be combined into 10 coarser bins, known as world bins because they are typically used when comparing the data to other experiments. Table 12 in Appendix A lists the x ranges for the 10 world bins. To combine the fine bins, the data are evolved from a specific Q^2, Q_o^2, to the average Q^2 of each world bin, Q_{avg}^2, using the Q^2-dependence of g_2^{WW} as follows

$$g_2(Q_{avg}^2) = g_2(Q_o^2) - g_2^{WW}(Q_o^2) + g_2^{WW}(Q_{avg}^2). \tag{3}$$

The rebined results are shown in Fig. 45. The combined data agrees with g_2^{WW} with a χ^2/(dof) of 2.1 for 10 degrees of freedom. The data for g_2^p are inconsistent with zero (χ^2/(dof)=14.7). The data are also compared to the bag model calculation of Stratmann [30], which is in good agreement with the data, and a chiral soliton model calculation of Weigel [34], which is somewhat too negative in the region near $x = 0.4$. The bag model calculation of Song [33] is in significant disagreement with the data. The models are calculated at the average Q^2 of the experiment, 5 GeV^2, while g_2^{WW} is evaluated at the average Q^2 of each world bin using the E155 fit to g_1.

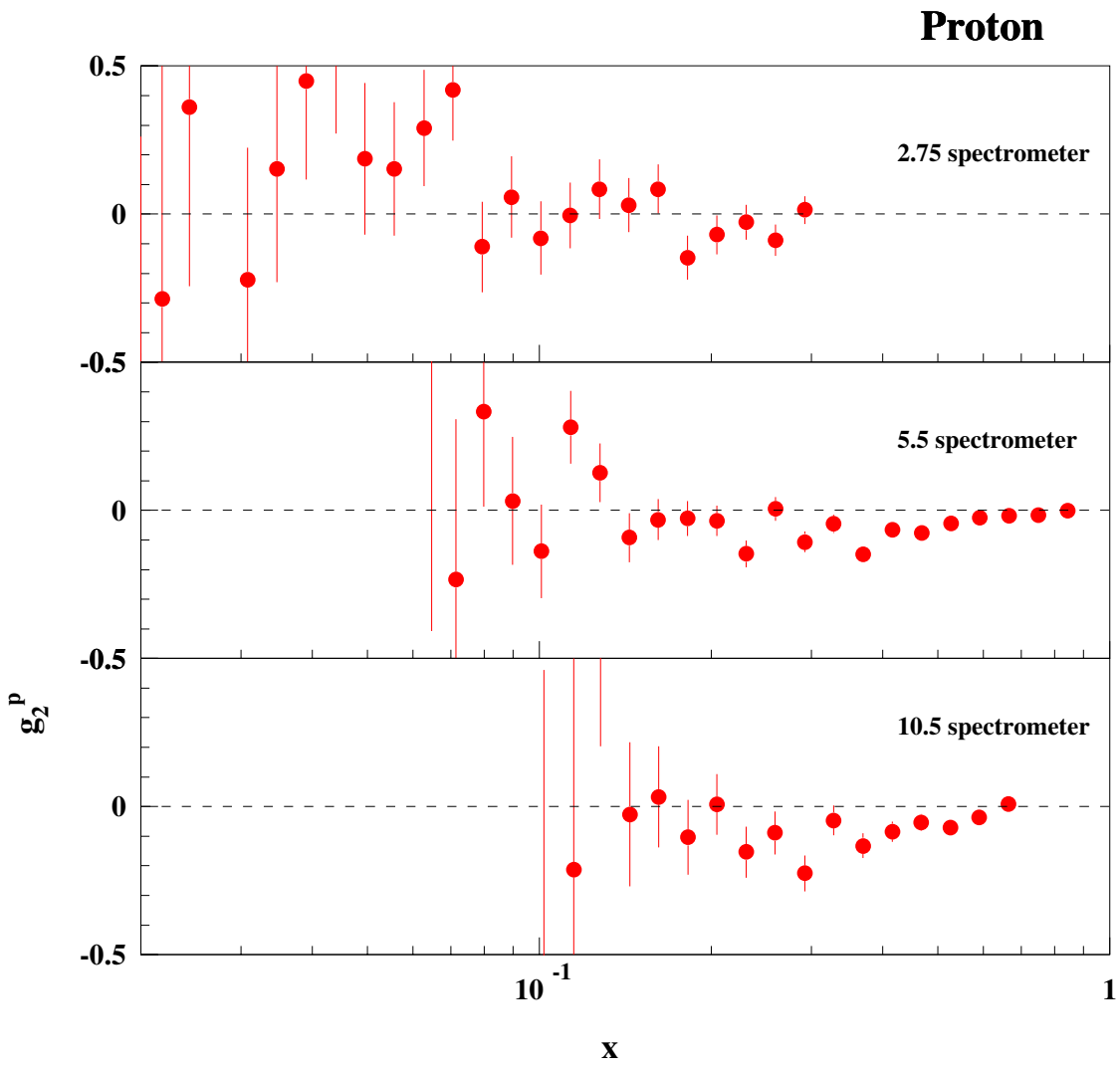

Figure 37: Final results for g_2 for the proton target with beam energies combined by taking a weighted average.

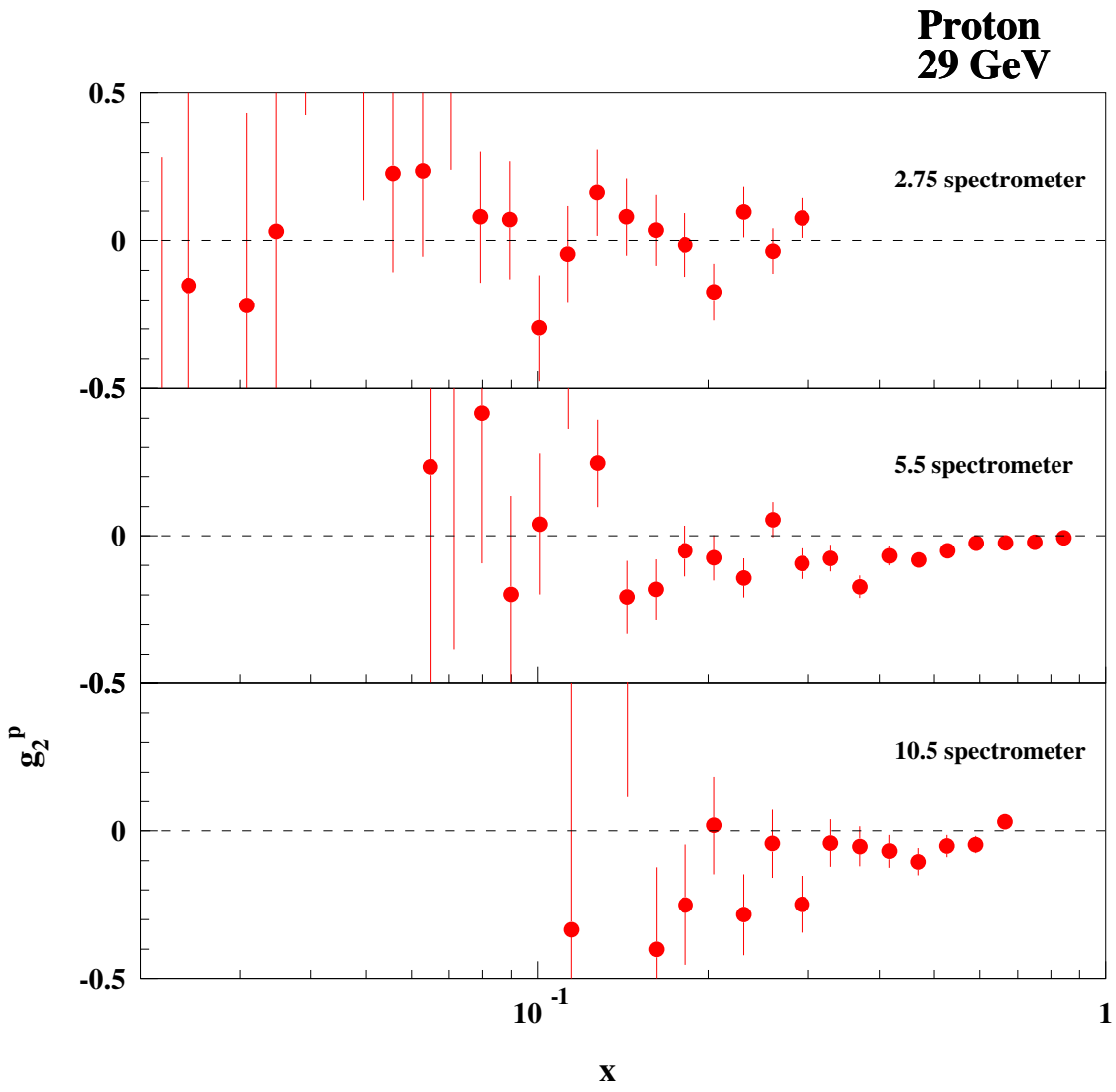

Figure 38: Results for g_2 for the proton target and a beam energy of 29 GeV.

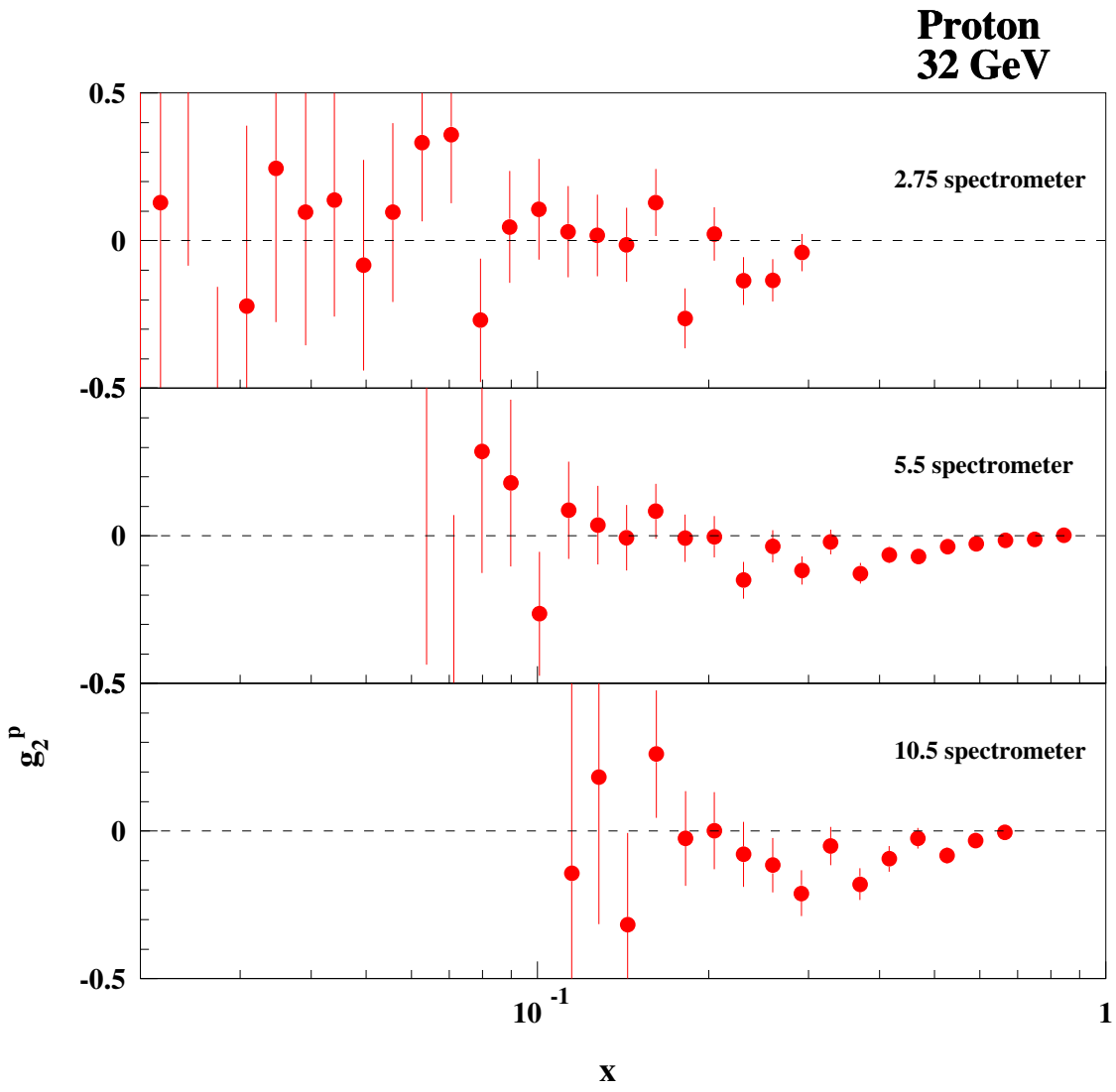

Figure 39: Results for g_2 for the proton target and a beam energy of 32 GeV.

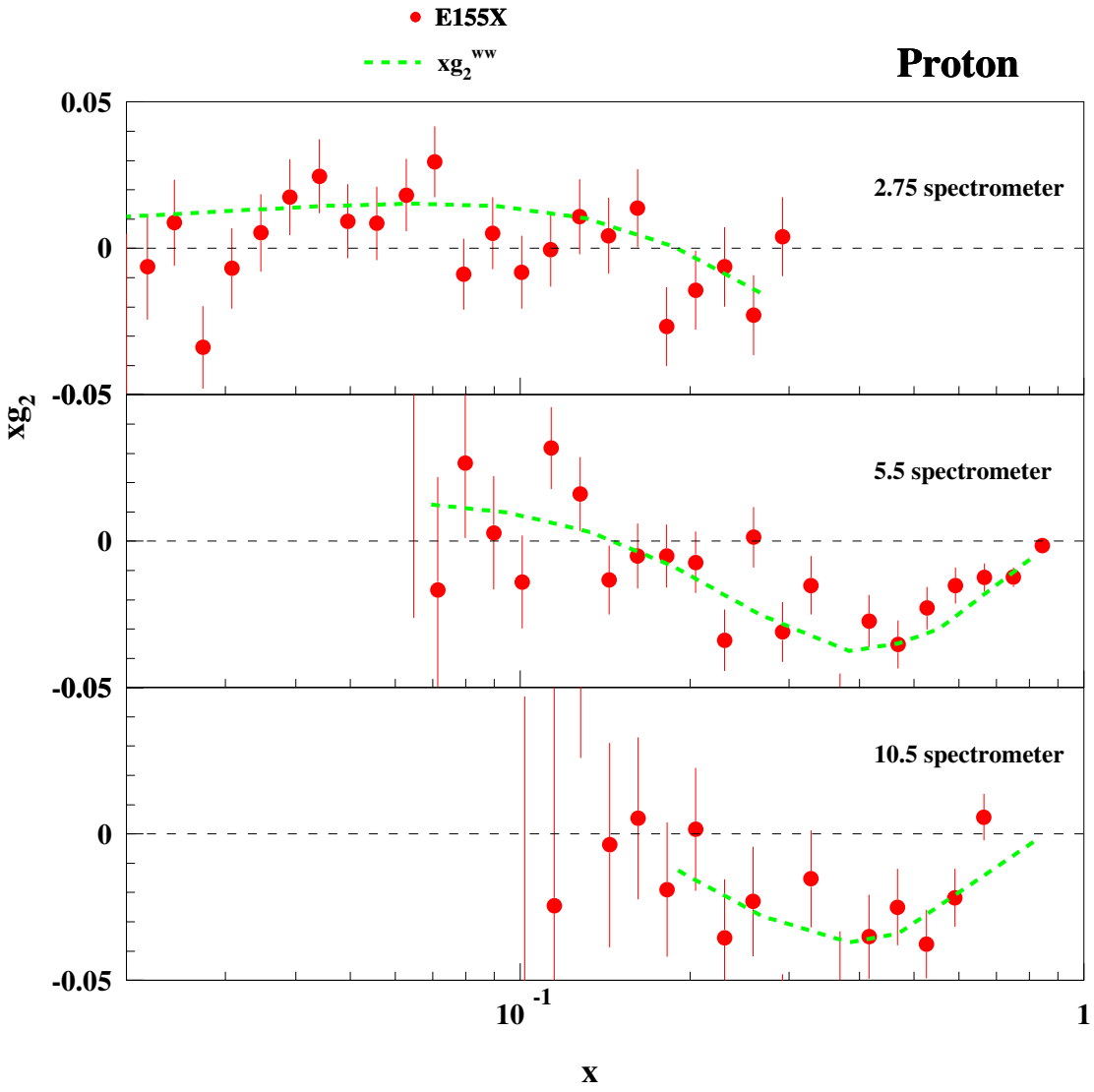

Figure 40: xg_2 as a function of x for the proton data, combined for both energies. Also shown is the curve for xg_2^{WW} using the E155 fit to g_1.

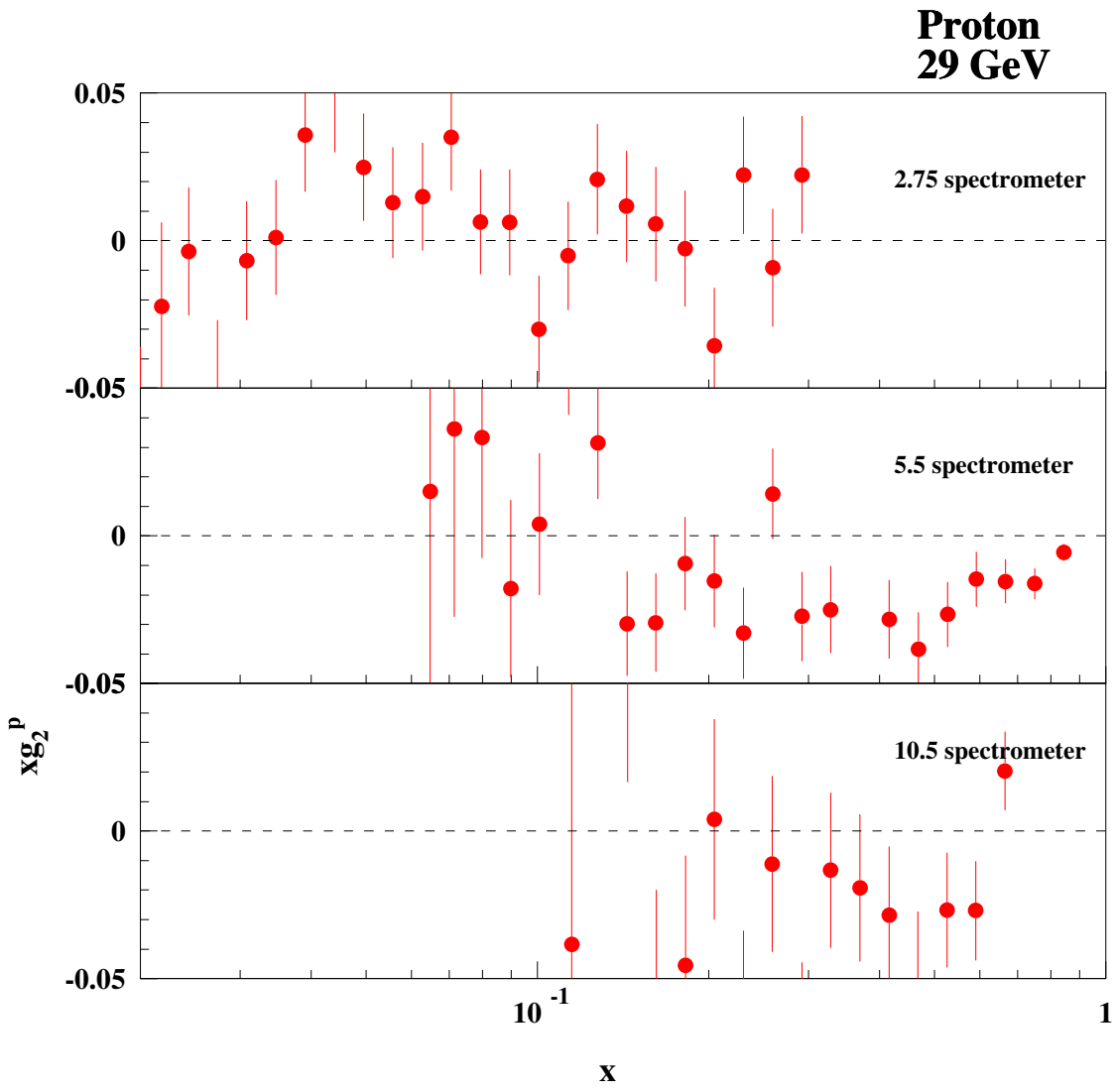

Figure 41: Results for xg_2 for the proton target and a beam energy of 29 GeV.

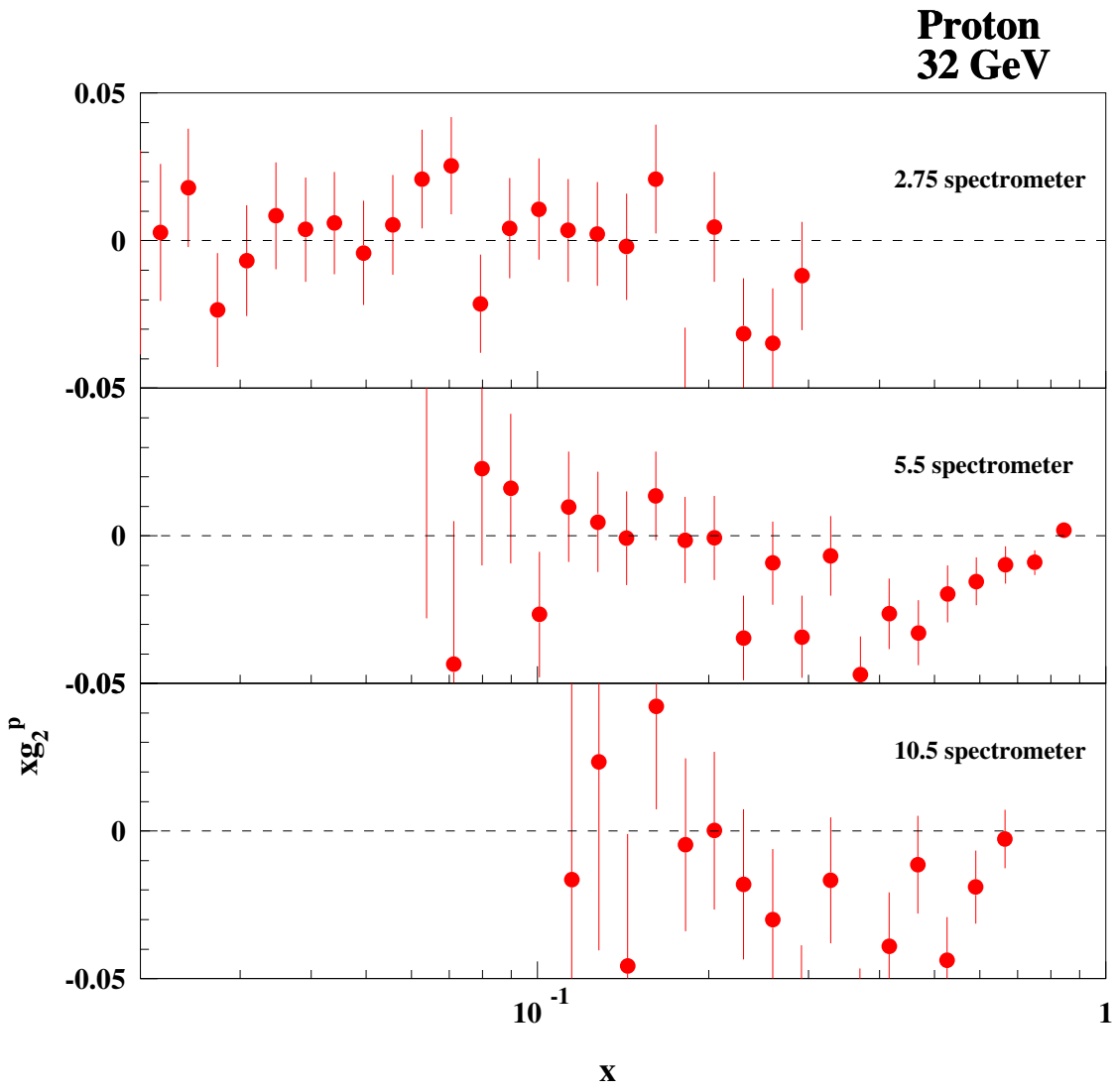

Figure 42: Results for xg_2 for the proton target and a beam energy of 32 GeV.

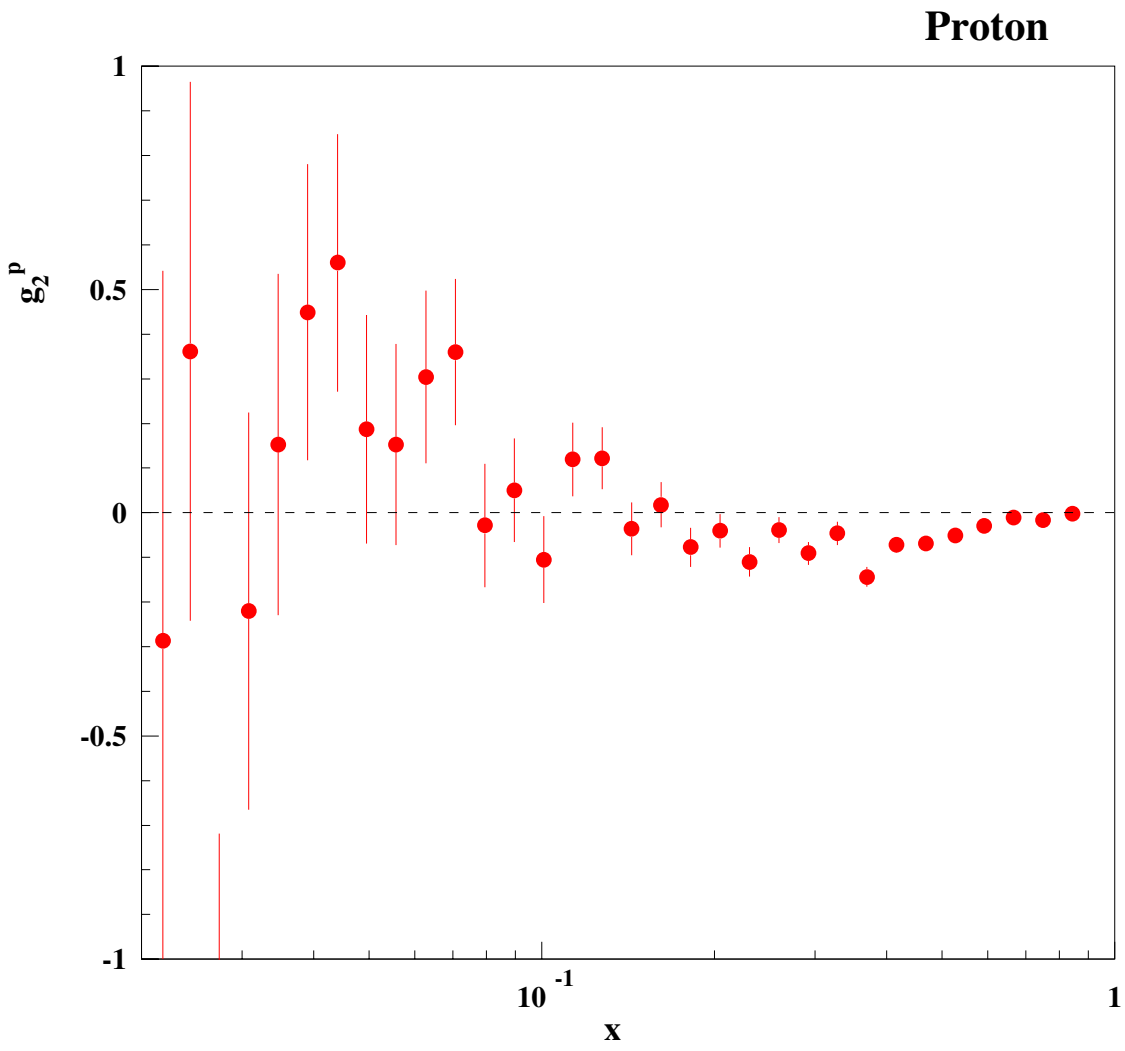

Figure 43: g_2 as a function of x for the proton target combined for all three spectrometers and bothe beam energies.

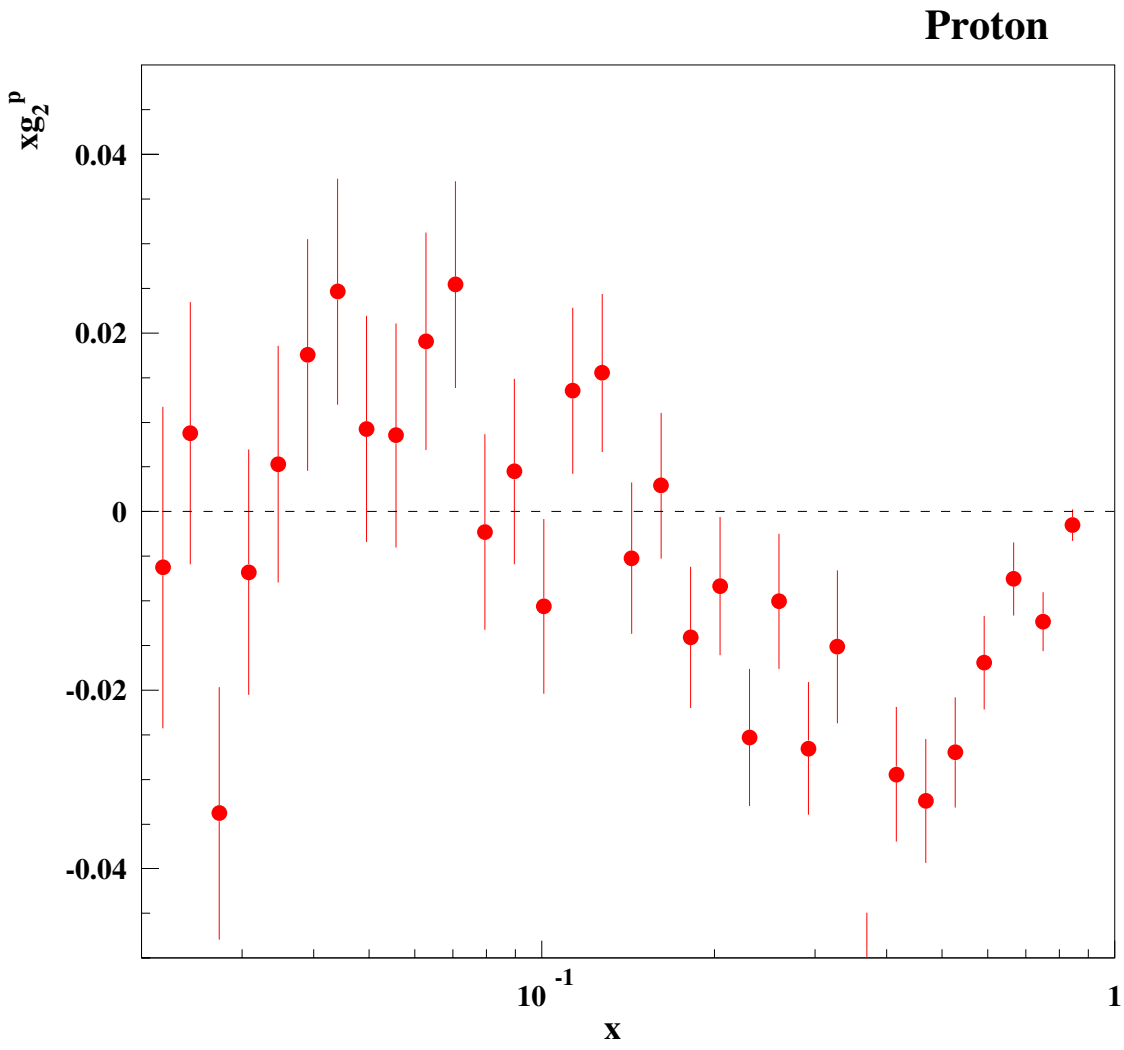

Figure 44: xg_2 as a function of x for the proton target, combined for all three spectrometers.

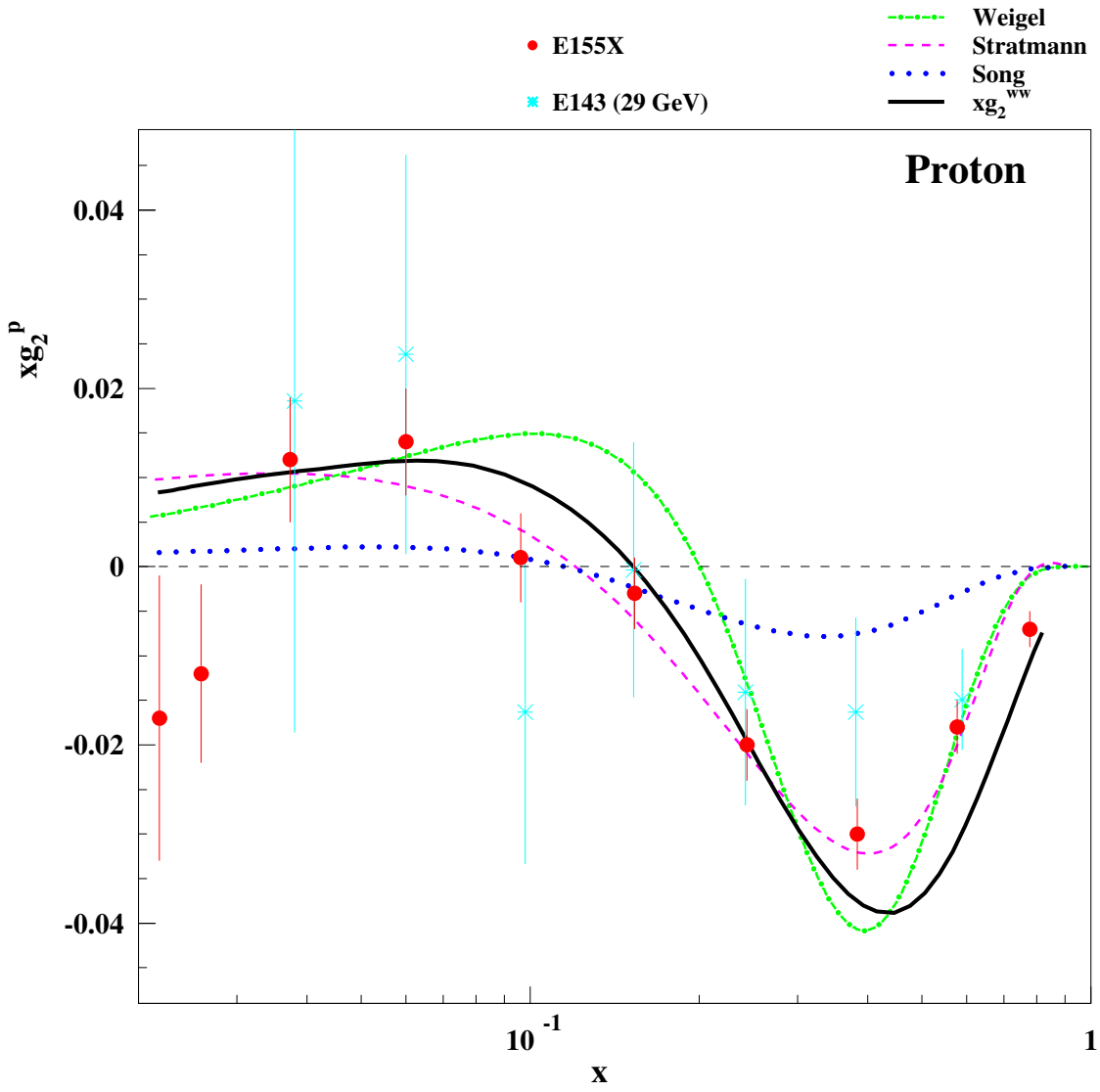

Figure 45: xg_2 as a function of x for the proton target data, rebinned in the world bins. Also shown are curves for xg_2^{WW} using the E155 fit to g_1 (solid line), the bag model calculation of Song (dotted line), the bag model calculation of Stratmann (dashed line), and the chiral soliton model calculation of Weigel (dot-dash line).

5.3 Q^2 Dependence of g_2

The Q^2 dependence of g_2 was also studied. Figure 46 shows the values of xg_2 as a function of Q^2 for several values of x. The data approximately follow the well known Q^2 dependence of g_2^{WW}, indicated by the dashed curves. There is no indication of an additional Q^2 dependence. Such a dependence could manifest itself by a $1/\sqrt{Q^2}$ type of term due to twist-3 components. The data are also consistent with no Q^2 dependence. The data do not permit us to make further distinctions about the Q^2-dependence of g_2.

5.4 A_2 Results

The results obtained for the proton target for A_2 at electron beam energies of 29 GeV and 32 GeV are plotted in Figs. 47 and 48. There is no significant difference between the results for the two different energies. The data for the two energies were combined by taking a weighted average, and the results are shown in Fig. 49. On these plots, we also show curves for the positivity limit $\sqrt{R}$, and the Soffer limit. The A_2 data is significantly lower than these limits. This result is in agreement with the theoretical predictions described in Sec. 2.6. Tables 25, 26 and 27 in Appendix C contain the results for A_2 at electron beam energy of 29 GeV, for the 2.75°, 5.5° and 10.5° spectrometers, respectively. Tables 28, 29 and 30 in Appendix C contain the results for A_2 at electron beam energy of 32 GeV, for the 2.75°, 5.5° and 10.5° spectrometers, respectively.

The A_2 results were then combined for all three spectrometers and rebinned

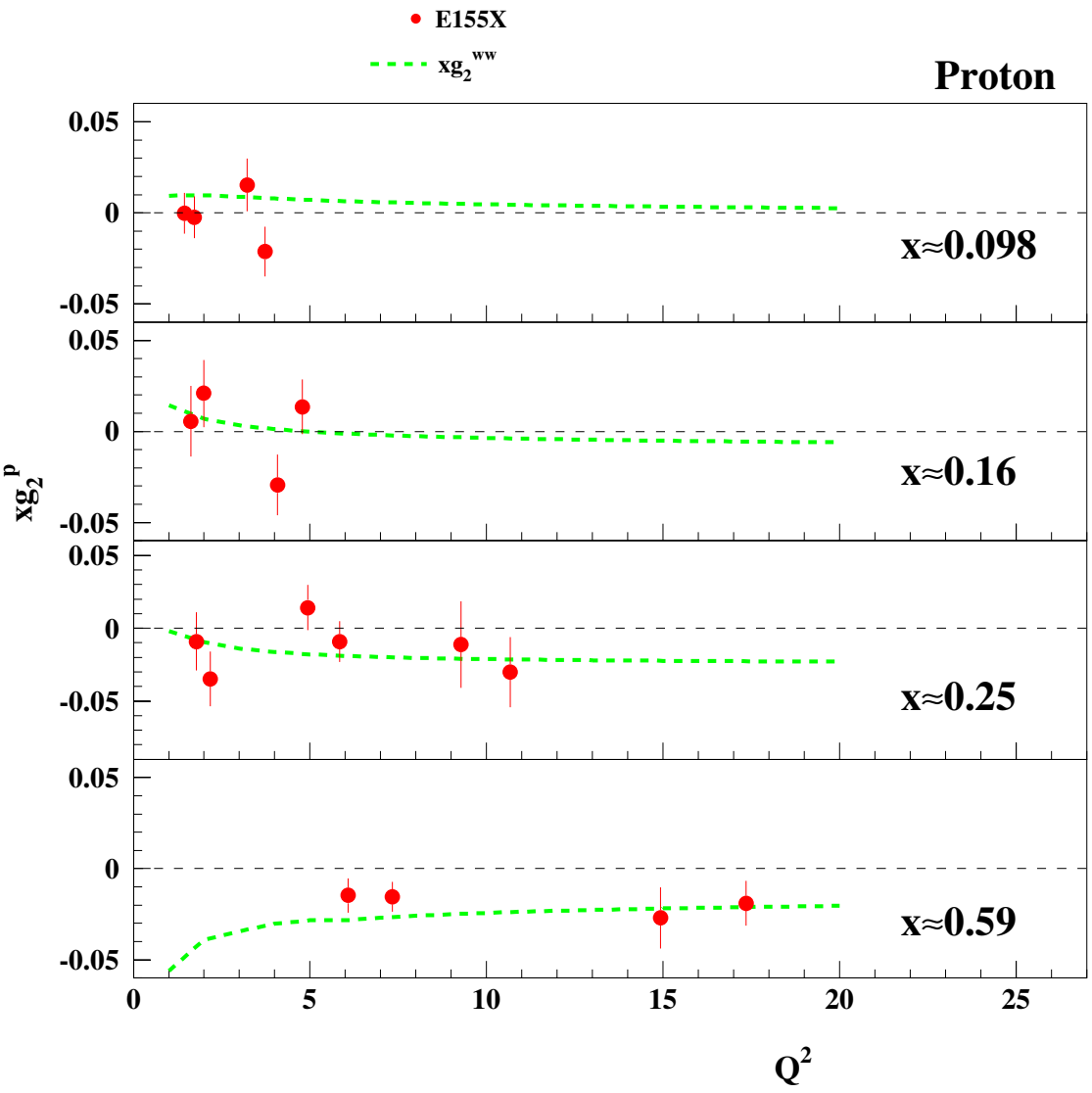

Figure 46: xg_2 for the proton as a function of Q^2 for selected values of x. The data for this experiment are the solid circles. The dashed curves indicate xg_2^{WW} using the E155 fit to g_1.

in the 10 world bins following the same method used to rebin g_2. Figure 50 shows the rebinned results for A_2. The average value for A_2 is consistent with zero at low x, but inconsistent with zero at higher x values. At the highest x value A_2 reaches about 0.1. The last data point on the plot has a large error bar making it indistinguishable from zero.

5.5 Sum Rules

5.5.1 Burkhardt-Cottingham Sum Rule

We evaluated the Burkhardt-Cottingham integral in the measured region $0.02 \leq x \leq 0.8$ at $Q^2 = 5$ (GeV)^2. The data were evolved to an average Q^2 of 5 (GeV)^2 by using the Q^2 dependence of g_2^{WW} as follows

$$g_2(Q^2_{avg}) = g_2(Q^2_{exp}) - g_2^{WW}(Q^2_{exp}) + g_2^{WW}(Q^2_{avg}). \tag{4}$$

The result for the proton is -0.036 ± 0.008. The integral result is inconsistent with the BC sum rule prediction of zero. However, since the behavior of g_2 as $x \to 0$ is not known, this is not a conclusive test of the BC sum rule.

5.5.2 ELT Sum Rule

We evaluated the Efremov-Leader-Terayev integral described in Sec. 2.3.2 in the measured region $0.02 \leq x \leq 0.8$ at $Q^2 = 5$ (GeV)^2. As discussed previously the data were evolved to the average Q^2 of the experiment by using the Q^2 dependence of g_2^{WW}. The result for the proton is -0.011 ± 0.008, which is roughly consistent with the expected value of zero. Once again the behavior of g_2 as $x \to 0$ is not

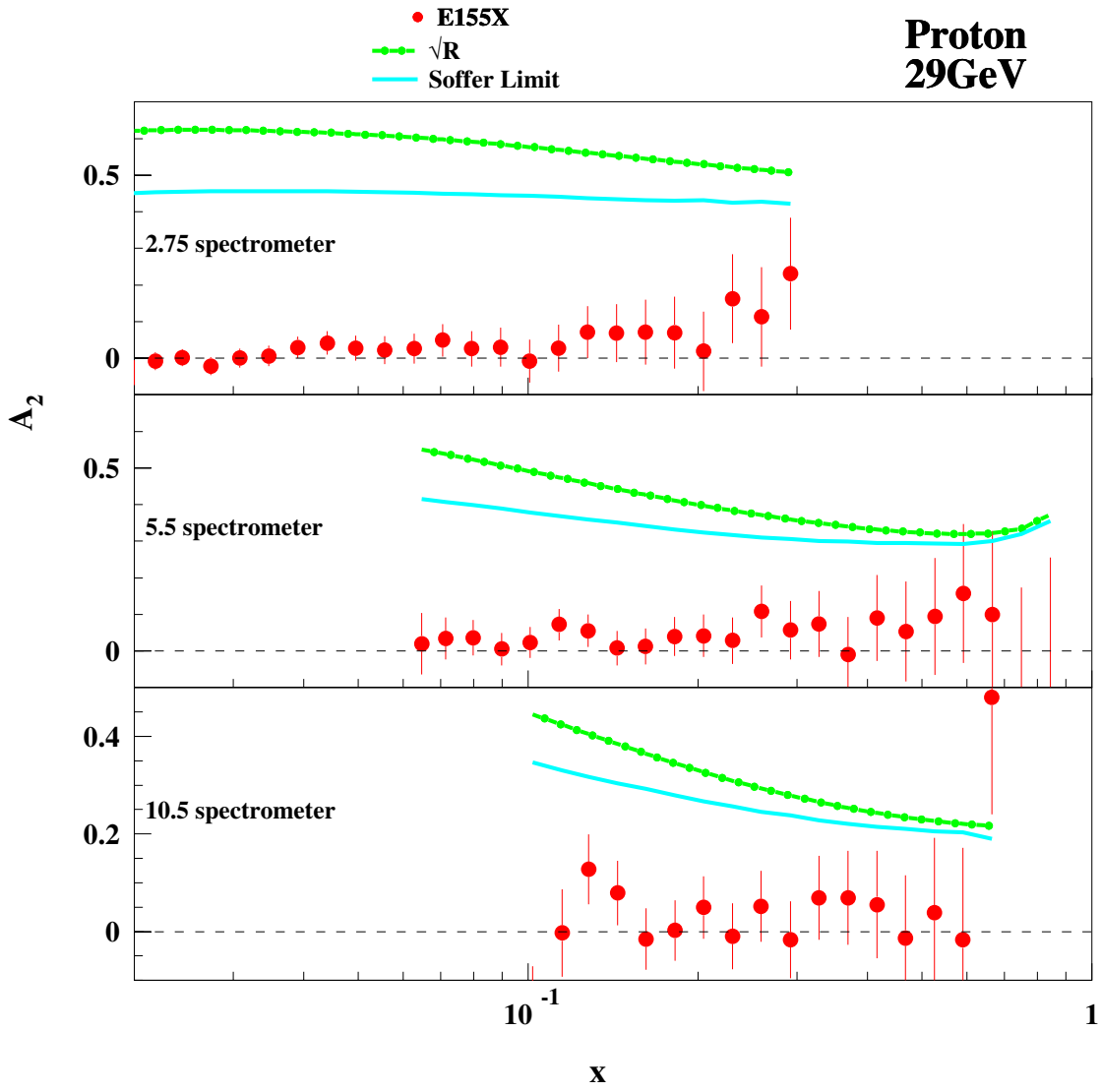

Figure 47: A_2 plotted versus x for the proton target at beam energy of 29 GeV. Also shown are the positivity limit $\sqrt{R}$ (dot-dash) and the Soffer limit (solid).

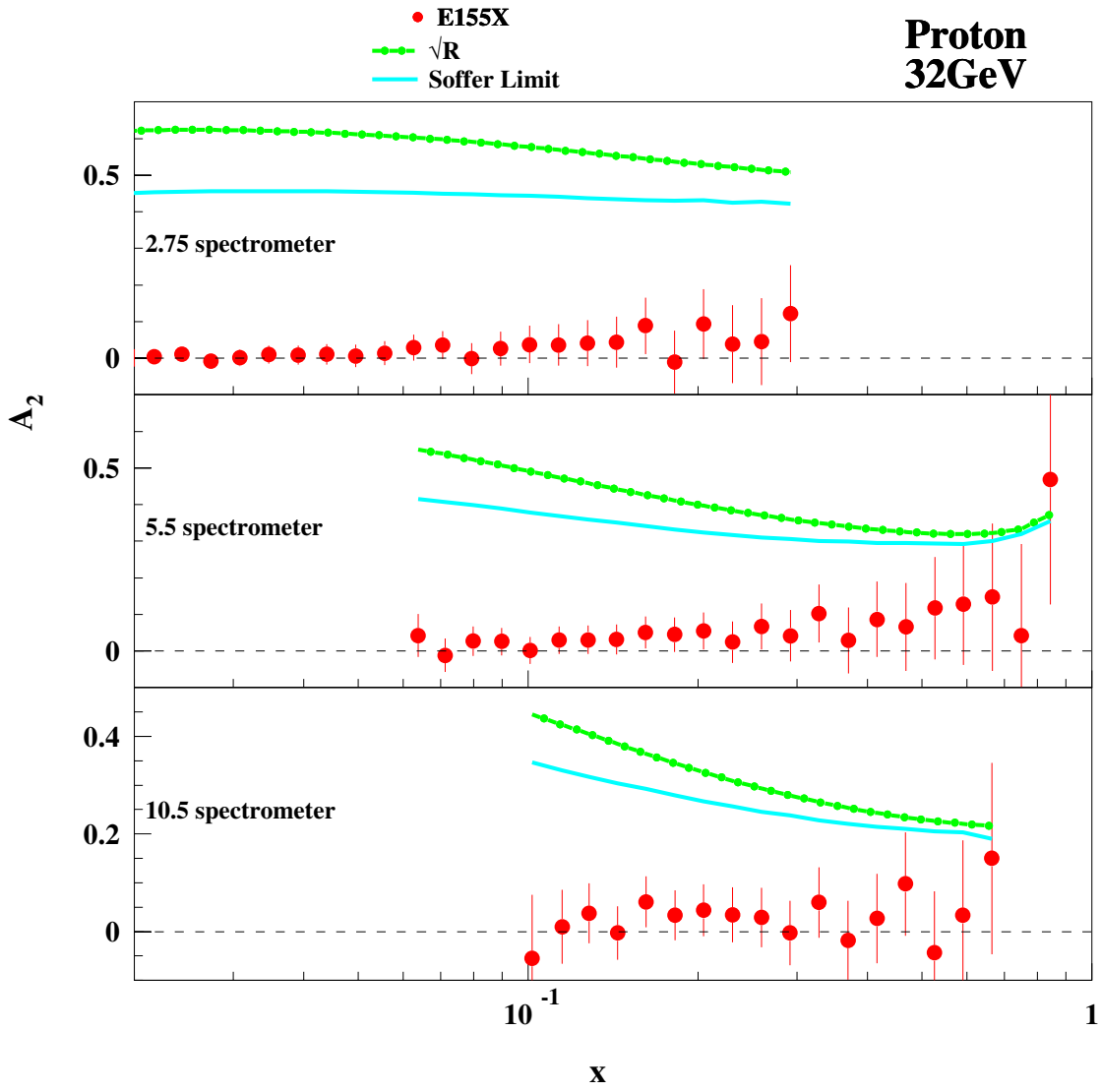

Figure 48: A_2 plotted versus x for the proton target at beam energy of 32 GeV. Also shown are the positivity limit $\sqrt{R}$ (dot-dash) and the Soffer limit (solid).

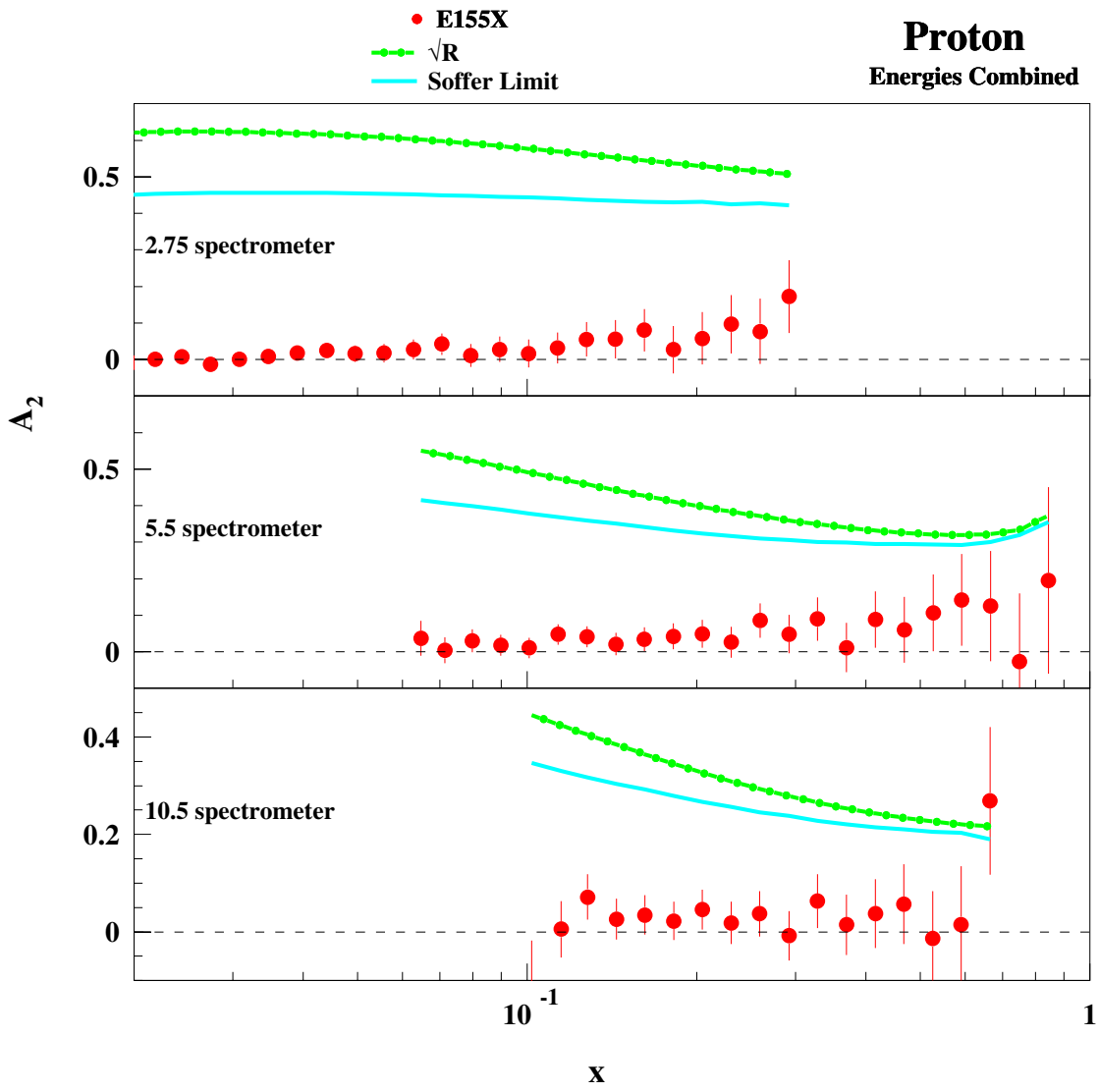

Figure 49: A_2 plotted versus x for the proton target, combined for both energies. Also shown are the positivity limit $\sqrt{R}$ (dot-dash) and the Soffer limit (solid).

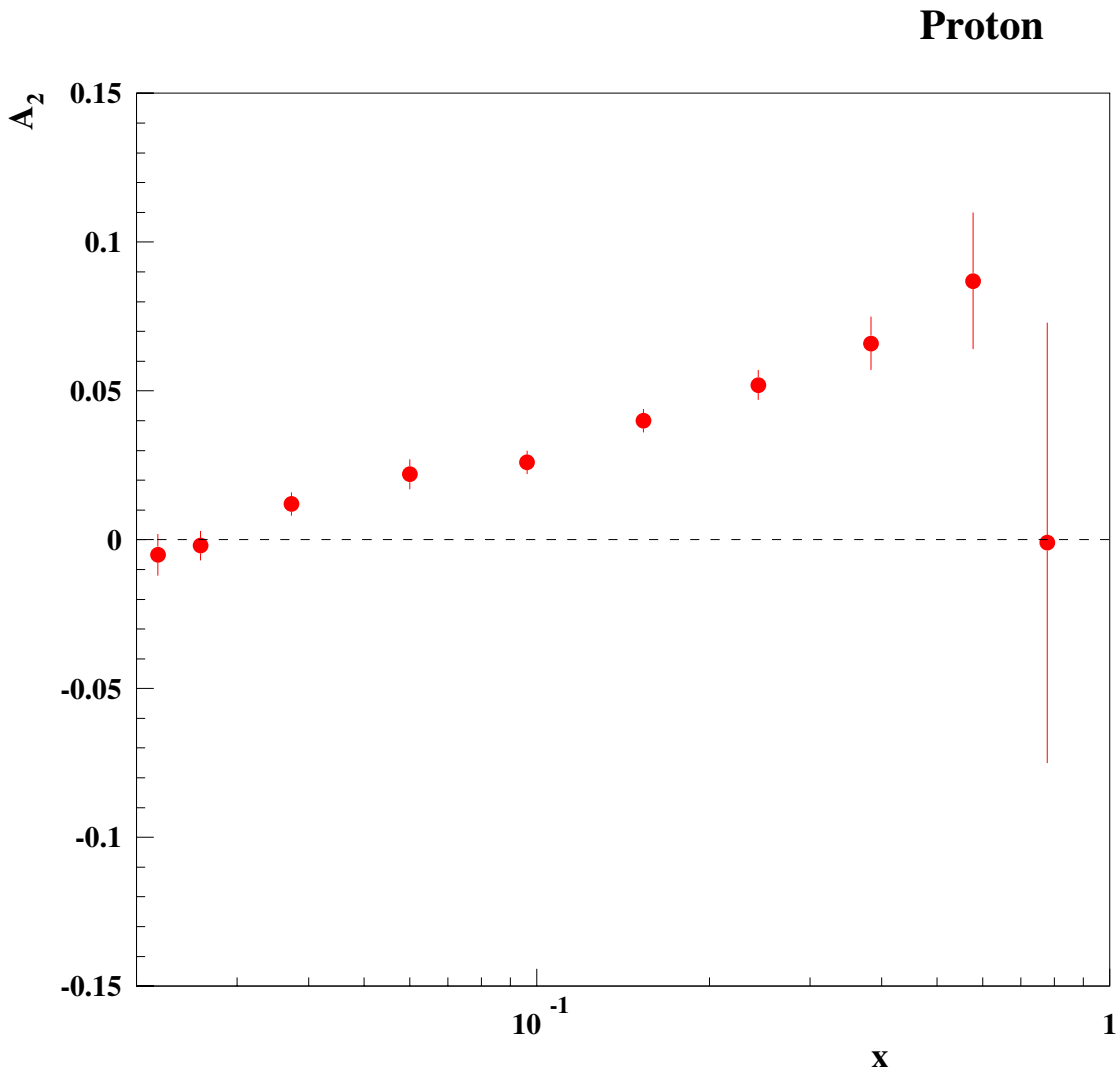

Figure 50: A_2 for the proton target data, rebinned in the 10 world bins. Each point is evaluated at the average Q^2 of the bin.

	d_2^p		
E155x	0.0028	$\pm$	0.0016
Bag Model (Stratmann) [30]	0.006	$\pm$	0.000
Bag Model (Song) [33]	0.018	$\pm$	0.000
QCD Sum Rule (Stein) [82]	-0.006	$\pm$	0.003
QCD Sum Rule (BBK) [83]	-0.003	$\pm$	0.006
QCD Sum Rule (Ehrnsperger) [84]	-0.006	$\pm$	0.003
Lattice QCD [18]	0.0085	$\pm$	0.0035

Table 10: Comparison of experimental and theoretical results for d_2^p. The values are evaluated at Q^2=5 GeV^2.

known. However, in this case the contribution is suppressed by a factor of x so that the net contribution can be expected to be reasonably small.

5.6 Twist-3 matrix element d_2

We obtained values for the matrix element d_2 which measures deviations of g_2 from the twist-2 g_2^{WW} term. The matrix element d_2 was calculated assuming that $\overline{g_2}$ is independent of Q^2 in the measured region. This assumption is reasonable since the matrix element d_2 is expected to depend logarithmically on Q^2 [81]. The part of the integral for $x \leq 0.02$ is neglected because of the x^2 suppression. For $x \geq 0.8$, $\overline{g_2} \propto (1-x)^m$ was used, where $m = 2$ or 3. This functional form was normalized to the data for $x \geq 0.5$. Since $\overline{g_2}$ is small at high x, the contribution was negligible in both cases. The value obtained for the proton was $d_2 = 0.0028 \pm 0.0016$. The result is consistent with a non-zero value for the twist-3 matrix element. Table 10 gives values obtained for d_2 by different theoretical models for comparison.

CHAPTER 6

Conclusion

A new measurement of g_2 for the proton has been presented for the kinematic range $0.02 \leq x \leq 0.8$ and $0.7 \leq Q^2 \leq 20$ $(\mathrm{GeV/c})^2$. This measurement provides an additional piece of information toward understanding the structure of matter. A new measurement for A_2 has also been presented. These results have been compared to the currently available theoretical predictions.

The precision of the data allows us for the first time to make clear statements on g_2 for the proton. It was found that g_2^p is clearly inconsistent with zero. In addition, the proton results for g_2 are reasonably consistent with the twist-2 g_2^{WW} prediction. The new precision of the proton data also allows the differentiation between theoretical models. It was found that the bag model calculation of Stratmann is in good agreement with the data, while the center of mass bag calculation of Song is not. The chiral soliton model calculation of Weigel in general agrees well with the data but is somewhat too negative around x of 0.4.

The value obtained for the twist-3 matrix element d_2 from this measurement is approximately two standard deviations away from zero, which suggests that g_2 exhibits some twist-3 dependence, but that this twist-3 component is very small. The

Burkhardt-Cottingham and Efremov-Leader-Terayev integrals were determined in the measured kinematic region of the experiment. It was found that the BC integral is inconsistent with zero, in contradiction with the prediction of zero. However, this is not conclusive since the behavior of g_2 as $x \rightarrow 0$ is not known. The ELT integral was found to be consistent with zero in the measured region. Again, this is not a conclusive test since the behavior of g_2 as $x \rightarrow 0$ is not known.

With future experiments scheduled to be performed at the Thomas Jefferson National Accelerator Facility, more data at lower beam energies will be obtained which will complement our current picture of the structure of the nucleons. The 12 GeV upgrade at Jlab will allow for a series of experiments which will provide new insight into how the nuclear building blocks are made from quarks and gluons. Dedicated experiments to measure g_2 and d_2 for the neutron have already been proposed and should provide more exciting results.

APPENDIX A

Tables of asymmetry results with all corrections applied

The following tables give the results of the measured asymmetry as obtained by the analysis described in Chapter 4. These asymmetry results include all the corrections discussed previously. The final asymmetry is referred to as $A_\perp$ even though it includes a small parallel component due to the orientation of the target polarization direction at 92.4° away from the beam line, instead of 90°. Table 11 shows the x ranges for the 38 bins in which the analysis was performed. Table 12 shows the x ranges for the 10 world bins. Tables 13, 14 and 15 contain the asymmetry results for the proton target at electron beam energy of 29 GeV for the 2.75°, 5.5° and 10.5° spectrometers, respectively. Tables 16, 17 and 18 contain the asymmetry results for the proton target at electron beam energy of 32 GeV for the 2.75°, 5.5° and 10.5° spectrometers, respectively. The tables do not show all 38 bins for the three spectrometers. Bins below bin 6 in the 2.75° spectrometer, bin 16 in the 5.5° spectrometer and bin 20 in the 10.5° spectrometer do not contain significant amounts of events, so they were removed. Bins above bin 30 in the 2.75° spectrometer were also removed because the momentum resolution becomes extremely poor in this spectrometer above bin 30 (See Reference [85]). Bins above

bin 36 in the 10.5° spectrometer do not contain any events, and have been removed as well.

x bin	x range
1	0.010 - 0.011
2	0.011 - 0.013
3	0.013 - 0.014
4	0.014 - 0.016
5	0.016 - 0.018
6	0.018 - 0.020
7	0.020 - 0.023
8	0.023 - 0.025
9	0.025 - 0.029
10	0.029 - 0.032
11	0.032 - 0.036
12	0.036 - 0.041
13	0.041 - 0.046
14	0.046 - 0.052
15	0.052 - 0.058
16	0.058 - 0.065
17	0.066 - 0.073
18	0.074 - 0.083
19	0.083 - 0.093
20	0.093 - 0.105
21	0.105 - 0.118
22	0.118 - 0.133
23	0.133 - 0.149
24	0.149 - 0.168
25	0.168 - 0.189
26	0.189 - 0.213
27	0.213 - 0.239
28	0.239 - 0.262
29	0.269 - 0.303
30	0.303 - 0.341
31	0.341 - 0.383
32	0.383 - 0.431
33	0.431 - 0.485
34	0.485 - 0.546
35	0.546 - 0.615
36	0.615 - 0.692
37	0.692 - 0.778
38	0.778 - 0.876

Table 11: Fine bins x ranges.

x bin	x range
1	0.018 - 0.023
2	0.023 - 0.029
3	0.029 - 0.047
4	0.047 - 0.075
5	0.075 - 0.120
6	0.120 - 0.193
7	0.193 - 0.310
8	0.310 - 0.498
9	0.498 - 0.700
10	0.700 - 0.900

Table 12: World bins x ranges.

x bin	$< x >$	$< Q^2 >$	$A_\perp$
6	0.020	0.71	0.0241 ± 0.0162
7	0.022	0.76	0.0033 ± 0.0068
8	0.024	0.82	-0.0012 ± 0.0053
9	0.027	0.86	0.0098 ± 0.0052
10	0.031	0.91	-0.0005 ± 0.0052
11	0.035	0.96	-0.0026 ± 0.0051
12	0.039	1.02	-0.0118 ± 0.0050
13	0.044	1.07	-0.0152 ± 0.0049
14	0.049	1.13	-0.0090 ± 0.0048
15	0.056	1.18	-0.0059 ± 0.0050
16	0.063	1.23	-0.0065 ± 0.0049
17	0.071	1.29	-0.0119 ± 0.0048
18	0.079	1.34	-0.0043 ± 0.0047
19	0.089	1.40	-0.0043 ± 0.0048
20	0.101	1.45	0.0053 ± 0.0048
21	0.113	1.50	-0.0014 ± 0.0049
22	0.128	1.54	-0.0083 ± 0.0050
23	0.144	1.59	-0.0059 ± 0.0051
24	0.162	1.63	-0.0043 ± 0.0052
25	0.182	1.67	-0.0022 ± 0.0053
26	0.205	1.71	0.0069 ± 0.0054
27	0.230	1.74	-0.0092 ± 0.0056
28	0.259	1.77	-0.0003 ± 0.0058
29	0.292	1.80	-0.0098 ± 0.0061
30	0.329	1.83	-0.0061 ± 0.0063

Table 13: Measured asymmetry results for the 2.75° spectrometer with the proton target at electron beam energy of 29 GeV.

x bin	$< x >$	$< Q^2 >$	$A_\perp$
16	0.065	2.32	0.0031 ± 0.0521
17	0.071	2.49	0.0104 ± 0.0216
18	0.080	2.71	0.0098 ± 0.0144
19	0.090	2.94	-0.0084 ± 0.0110
20	0.101	3.17	-0.0003 ± 0.0093
21	0.114	3.40	0.0231 ± 0.0084
22	0.128	3.62	0.0114 ± 0.0079
23	0.144	3.85	-0.0144 ± 0.0076
24	0.162	4.08	-0.0146 ± 0.0075
25	0.182	4.30	-0.0057 ± 0.0074
26	0.205	4.52	-0.0087 ± 0.0076
27	0.230	4.74	-0.0180 ± 0.0079
28	0.259	4.93	0.0068 ± 0.0084
29	0.292	5.13	-0.0169 ± 0.0089
30	0.328	5.31	-0.0168 ± 0.0096
31	0.370	5.50	-0.0478 ± 0.0105
32	0.416	5.66	-0.0249 ± 0.0115
33	0.468	5.81	-0.0408 ± 0.0130
34	0.527	5.96	-0.0367 ± 0.0150
35	0.592	6.08	-0.0281 ± 0.0178
36	0.667	6.20	-0.0449 ± 0.0217
37	0.750	6.30	-0.0868 ± 0.0281
38	0.844	6.39	-0.0843 ± 0.0438

Table 14: Measured asymmetry results for the 5.5° spectrometer with the proton target at electron beam energy of 29 GeV.

x bin	$< x >$	$< Q^2 >$	$A_\perp$
20	0.102	4.40	0.1404 ± 0.1655
21	0.115	4.89	0.0006 ± 0.0521
22	0.128	5.34	-0.0814 ± 0.0315
23	0.144	5.90	-0.0498 ± 0.0253
24	0.162	6.51	0.0127 ± 0.0219
25	0.182	7.17	0.0029 ± 0.0196
26	0.205	7.85	-0.0255 ± 0.0198
27	0.230	8.57	0.0164 ± 0.0204
28	0.259	9.28	-0.0201 ± 0.0215
29	0.292	10.04	0.0288 ± 0.0230
30	0.328	10.83	-0.0205 ± 0.0252
31	0.369	11.67	-0.0136 ± 0.0286
32	0.415	12.48	0.0029 ± 0.0331
33	0.467	13.30	0.0512 ± 0.0400
34	0.525	14.10	0.0294 ± 0.0504
35	0.591	14.93	0.0669 ± 0.0671
36	0.665	15.70	-0.1825 ± 0.0934

Table 15: Measured asymmetry results for the 10.5° spectrometer with the proton target at electron beam energy of 29 GeV.

x bin	$< x >$	$< Q^2 >$	$A_\perp$
6	0.020	0.81	-0.0013 ± 0.0089
7	0.022	0.88	-0.0027 ± 0.0051
8	0.024	0.94	-0.0063 ± 0.0046
9	0.027	0.99	0.0033 ± 0.0045
10	0.031	1.05	-0.0007 ± 0.0045
11	0.035	1.12	-0.0045 ± 0.0044
12	0.039	1.19	-0.0034 ± 0.0044
13	0.044	1.26	-0.0040 ± 0.0043
14	0.049	1.32	-0.0015 ± 0.0044
15	0.056	1.39	-0.0040 ± 0.0043
16	0.063	1.46	-0.0080 ± 0.0043
17	0.071	1.54	-0.0093 ± 0.0042
18	0.079	1.61	0.0028 ± 0.0043
19	0.089	1.68	-0.0039 ± 0.0044
20	0.101	1.75	-0.0057 ± 0.0045
21	0.113	1.81	-0.0038 ± 0.0046
22	0.128	1.87	-0.0036 ± 0.0046
23	0.144	1.93	-0.0025 ± 0.0048
24	0.162	1.99	-0.0086 ± 0.0049
25	0.182	2.04	0.0098 ± 0.0050
26	0.205	2.09	-0.0044 ± 0.0051
27	0.230	2.14	0.0057 ± 0.0052
28	0.259	2.18	0.0069 ± 0.0054
29	0.292	2.22	0.0004 ± 0.0056
30	0.329	2.26	-0.0053 ± 0.0059

Table 16: Measured asymmetry results for the 2.75° spectrometer with the proton target at electron beam energy of 32 GeV.

x bin	$< x >$	$< Q^2 >$	$A_\perp$
16	0.064	2.65	0.0172 ± 0.0283
17	0.071	2.87	-0.0159 ± 0.0154
18	0.080	3.13	0.0055 ± 0.0109
19	0.090	3.40	0.0035 ± 0.0088
20	0.101	3.67	-0.0117 ± 0.0078
21	0.113	3.94	0.0019 ± 0.0072
22	0.128	4.22	0.0001 ± 0.0068
23	0.144	4.50	-0.0020 ± 0.0066
24	0.162	4.78	0.0043 ± 0.0065
25	0.182	5.06	-0.0021 ± 0.0067
26	0.205	5.33	-0.0016 ± 0.0068
27	0.230	5.59	-0.0187 ± 0.0073
28	0.259	5.85	-0.0060 ± 0.0076
29	0.292	6.10	-0.0209 ± 0.0082
30	0.328	6.33	-0.0052 ± 0.0087
31	0.370	6.56	-0.0355 ± 0.0095
32	0.416	6.77	-0.0236 ± 0.0105
33	0.468	6.97	-0.0359 ± 0.0119
34	0.527	7.17	-0.0282 ± 0.0137
35	0.592	7.34	-0.0311 ± 0.0163
36	0.667	7.50	-0.0313 ± 0.0199
37	0.750	7.63	-0.0548 ± 0.0257
38	0.844	7.76	0.0340 ± 0.0401

Table 17: Measured asymmetry results for the 5.5° spectrometer with the proton target at electron beam energy of 32 GeV.

x bin	$< x >$	$< Q^2 >$	$A_\perp$
20	0.102	4.99	0.0336 ± 0.1258
21	0.115	5.55	-0.0070 ± 0.0396
22	0.128	6.09	-0.0234 ± 0.0248
23	0.144	6.71	0.0032 ± 0.0187
24	0.162	7.42	-0.0370 ± 0.0159
25	0.182	8.18	-0.0175 ± 0.0145
26	0.205	8.97	-0.0222 ± 0.0147
27	0.230	9.82	-0.0135 ± 0.0155
28	0.259	10.68	-0.0064 ± 0.0165
29	0.292	11.59	0.0186 ± 0.0178
30	0.328	12.52	-0.0169 ± 0.0198
31	0.369	13.49	0.0395 ± 0.0221
32	0.416	14.45	0.0177 ± 0.0255
33	0.467	15.41	-0.0174 ± 0.0303
34	0.526	16.38	0.0742 ± 0.0379
35	0.591	17.35	0.0370 ± 0.0498
36	0.664	18.28	-0.0189 ± 0.0704

Table 18: Measured asymmetry results for the 10.5° spectrometer with the proton target at electron beam energy of 32 GeV.

APPENDIX B

Tables of asymmetry results without radiative corrections

The following tables contain the results for the measured asymmetry without radiative corrections applied. Tables 19, 20 and 21 contain the asymmetry results without radiative corrections for the proton target at electron beam energy of 29 GeV for the 2.75°, 5.5° and 10.5° spectrometers, respectively. Tables 22, 23 and 24 contain the asymmetry results without radiative corrections for the proton target at electron beam energy of 32 GeV for the 2.75°, 5.5° and 10.5° spectrometers, respectively. The uncertainties shown are statistical uncertainties.

x bin	$< x >$	$< Q^2 >$	$A_\perp$
6	0.020	0.71	0.0204 ± 0.0130
7	0.022	0.76	0.0039 ± 0.0057
8	0.024	0.82	0.0003 ± 0.0046
9	0.027	0.86	0.0103 ± 0.0046
10	0.031	0.91	0.0013 ± 0.0046
11	0.035	0.96	-0.0005 ± 0.0047
12	0.039	1.02	-0.0091 ± 0.0047
13	0.044	1.07	-0.0125 ± 0.0047
14	0.049	1.13	-0.0066 ± 0.0046
15	0.056	1.18	-0.0035 ± 0.0048
16	0.063	1.23	-0.0041 ± 0.0047
17	0.071	1.29	-0.0093 ± 0.0047
18	0.079	1.34	-0.0018 ± 0.0046
19	0.089	1.40	-0.0017 ± 0.0047
20	0.101	1.45	0.0078 ± 0.0047
21	0.113	1.50	0.0013 ± 0.0048
22	0.128	1.54	-0.0055 ± 0.0049
23	0.144	1.59	-0.0031 ± 0.0050
24	0.162	1.63	-0.0016 ± 0.0051
25	0.182	1.67	0.0005 ± 0.0053
26	0.205	1.71	0.0095 ± 0.0053
27	0.230	1.74	-0.0065 ± 0.0055
28	0.259	1.77	0.0022 ± 0.0057
29	0.292	1.80	-0.0075 ± 0.0060
30	0.329	1.83	-0.0039 ± 0.0062

Table 19: Measured asymmetry results without radiative corrections for the 2.75° spectrometer with the proton target at electron beam energy of 29 GeV.

x bin	$< x >$	$< Q^2 >$	$A_\perp$
16	0.065	2.32	-0.0005 ± 0.0483
17	0.071	2.49	0.0061 ± 0.0204
18	0.080	2.71	0.0054 ± 0.0138
19	0.090	2.94	-0.0124 ± 0.0106
20	0.101	3.17	-0.0048 ± 0.0090
21	0.114	3.40	0.0180 ± 0.0083
22	0.128	3.62	0.0064 ± 0.0078
23	0.144	3.85	-0.0192 ± 0.0075
24	0.162	4.08	-0.0195 ± 0.0074
25	0.182	4.30	-0.0106 ± 0.0073
26	0.205	4.52	-0.0133 ± 0.0076
27	0.230	4.74	-0.0224 ± 0.0079
28	0.259	4.93	0.0025 ± 0.0084
29	0.292	5.13	-0.0208 ± 0.0089
30	0.328	5.31	-0.0204 ± 0.0096
31	0.370	5.50	-0.0509 ± 0.0105
32	0.416	5.66	-0.0275 ± 0.0115
33	0.468	5.81	-0.0429 ± 0.0130
34	0.527	5.96	-0.0381 ± 0.0150
35	0.592	6.08	-0.0287 ± 0.0177
36	0.667	6.20	-0.0442 ± 0.0216
37	0.750	6.30	-0.0866 ± 0.0278
38	0.844	6.39	-0.0848 ± 0.0424

Table 20: Measured asymmetry results without radiative corrections for the 5.5° spectrometer with the proton target at electron beam energy of 29 GeV.

x bin	$< x >$	$< Q^2 >$	$A_\perp$
20	0.102	4.40	0.1303 ± 0.1442
21	0.115	4.89	0.0087 ± 0.0471
22	0.128	5.34	-0.0673 ± 0.0293
23	0.144	5.90	-0.0386 ± 0.0240
24	0.162	6.51	0.0210 ± 0.0211
25	0.182	7.17	0.0116 ± 0.0191
26	0.205	7.85	-0.0163 ± 0.0194
27	0.230	8.57	0.0246 ± 0.0201
28	0.259	9.28	-0.0118 ± 0.0212
29	0.292	10.04	0.0362 ± 0.0228
30	0.328	10.83	-0.0131 ± 0.0251
31	0.369	11.67	-0.0069 ± 0.0284
32	0.415	12.48	0.0090 ± 0.0330
33	0.467	13.30	0.0564 ± 0.0399
34	0.525	14.10	0.0339 ± 0.0504
35	0.591	14.93	0.0706 ± 0.0670
36	0.665	15.70	-0.1796 ± 0.0933

Table 21: Measured asymmetry results without radiative corrections for the 10.5° spectrometer with the proton target at electron beam energy of 29 GeV.

x bin	$< x >$	$< Q^2 >$	$A_\perp$
6	0.020	0.81	-0.0000 ± 0.0074
7	0.022	0.88	-0.0011 ± 0.0044
8	0.024	0.94	-0.0041 ± 0.0040
9	0.027	0.99	0.0045 ± 0.0041
10	0.031	1.05	0.0011 ± 0.0041
11	0.035	1.12	-0.0024 ± 0.0041
12	0.039	1.19	-0.0014 ± 0.0041
13	0.044	1.26	-0.0020 ± 0.0041
14	0.049	1.32	0.0005 ± 0.0043
15	0.056	1.39	-0.0018 ± 0.0042
16	0.063	1.46	-0.0057 ± 0.0042
17	0.071	1.54	-0.0069 ± 0.0042
18	0.079	1.61	0.0051 ± 0.0042
19	0.089	1.68	-0.0014 ± 0.0043
20	0.101	1.75	-0.0031 ± 0.0044
21	0.113	1.81	-0.0012 ± 0.0045
22	0.128	1.87	-0.0009 ± 0.0046
23	0.144	1.93	0.0002 ± 0.0047
24	0.162	1.99	-0.0059 ± 0.0049
25	0.182	2.04	0.0123 ± 0.0049
26	0.205	2.09	-0.0018 ± 0.0051
27	0.230	2.14	0.0081 ± 0.0052
28	0.259	2.18	0.0092 ± 0.0054
29	0.292	2.22	0.0026 ± 0.0056
30	0.329	2.26	-0.0032 ± 0.0058

Table 22: Measured asymmetry results without radiative corrections for the 2.75° spectrometer with the proton target at electron beam energy of 32 GeV.

x bin	$< x >$	$< Q^2 >$	$A_\perp$
16	0.064	2.65	0.0132 ± 0.0267
17	0.071	2.87	-0.0186 ± 0.0147
18	0.080	3.13	0.0017 ± 0.0105
19	0.090	3.40	-0.0005 ± 0.0086
20	0.101	3.67	-0.0157 ± 0.0076
21	0.113	3.94	-0.0025 ± 0.0071
22	0.128	4.22	-0.0043 ± 0.0067
23	0.144	4.50	-0.0065 ± 0.0066
24	0.162	4.78	-0.0002 ± 0.0065
25	0.182	5.06	-0.0065 ± 0.0066
26	0.205	5.33	-0.0060 ± 0.0068
27	0.230	5.59	-0.0228 ± 0.0072
28	0.259	5.85	-0.0099 ± 0.0076
29	0.292	6.10	-0.0245 ± 0.0082
30	0.328	6.33	-0.0084 ± 0.0087
31	0.370	6.56	-0.0383 ± 0.0095
32	0.416	6.77	-0.0259 ± 0.0105
33	0.468	6.97	-0.0377 ± 0.0119
34	0.527	7.17	-0.0295 ± 0.0137
35	0.592	7.34	-0.0317 ± 0.0163
36	0.667	7.50	-0.0311 ± 0.0198
37	0.750	7.63	-0.0542 ± 0.0255
38	0.844	7.76	0.0307 ± 0.0392

Table 23: Measured asymmetry results without radiative corrections for the 5.5° spectrometer with the proton target at electron beam energy of 32 GeV.

x bin	$< x >$	$< Q^2 >$	$A_\perp$
20	0.102	4.99	0.0376 ± 0.1160
21	0.115	5.55	0.0005 ± 0.0372
22	0.128	6.09	-0.0149 ± 0.0236
23	0.144	6.71	0.0106 ± 0.0181
24	0.162	7.42	-0.0285 ± 0.0155
25	0.182	8.18	-0.0097 ± 0.0142
26	0.205	8.97	-0.0144 ± 0.0144
27	0.230	9.82	-0.0061 ± 0.0153
28	0.259	10.68	0.0006 ± 0.0163
29	0.292	11.59	0.0252 ± 0.0177
30	0.328	12.52	-0.0105 ± 0.0196
31	0.369	13.49	0.0451 ± 0.0220
32	0.416	14.45	0.0229 ± 0.0254
33	0.467	15.41	-0.0128 ± 0.0302
34	0.526	16.38	0.0779 ± 0.0378
35	0.591	17.35	0.0399 ± 0.0497
36	0.664	18.28	-0.0169 ± 0.0703

Table 24: Measured asymmetry results without radiative corrections for the 10.5° spectrometer with the proton target at electron beam energy of 32 GeV.

APPENDIX C

Tables of xg_2 and A_2 results

The following tables contain the results for xg_2 and A_2. Tables 25, 26 and 27 contain the results for xg_2 and A_2 for the proton target at electron beam energy of 29 GeV for the 2.75°, 5.5° and 10.5° spectrometers, respectively. Tables 28, 29 and 30 contain the results for xg_2 and A_2 for the proton target at electron beam energy of 32 GeV for the 2.75°, 5.5° and 10.5° spectrometers, respectively.

x bin	$< x >$	$< Q^2 >$	$xg_2 \pm stat \pm syst$	$A_2 \pm stat \pm syst$
6	0.020	0.71	-0.0929 ± 0.0575 ± 0.0044	-0.0395 ± 0.0338 ± 0.0020
7	0.022	0.76	-0.0216 ± 0.0285 ± 0.0007	-0.0075 ± 0.0249 ± 0.0003
8	0.024	0.82	-0.0029 ± 0.0216 ± 0.0003	0.0016 ± 0.0231 ± 0.0001
9	0.027	0.86	-0.0469 ± 0.0208 ± 0.0020	-0.0209 ± 0.0245 ± 0.0011
10	0.031	0.91	-0.0060 ± 0.0201 ± 0.0001	0.0010 ± 0.0261 ± 0.0001
11	0.035	0.96	0.0018 ± 0.0195 ± 0.0005	0.0063 ± 0.0278 ± 0.0003
12	0.039	1.02	0.0365 ± 0.0191 ± 0.0023	0.0296 ± 0.0299 ± 0.0015
13	0.044	1.07	0.0494 ± 0.0186 ± 0.0030	0.0416 ± 0.0321 ± 0.0021
14	0.049	1.13	0.0256 ± 0.0182 ± 0.0018	0.0280 ± 0.0344 ± 0.0013
15	0.056	1.18	0.0135 ± 0.0188 ± 0.0012	0.0217 ± 0.0382 ± 0.0009
16	0.063	1.23	0.0155 ± 0.0182 ± 0.0013	0.0265 ± 0.0410 ± 0.0011
17	0.071	1.29	0.0357 ± 0.0180 ± 0.0023	0.0493 ± 0.0445 ± 0.0022
18	0.079	1.34	0.0070 ± 0.0177 ± 0.0008	0.0261 ± 0.0483 ± 0.0009
19	0.089	1.40	0.0069 ± 0.0180 ± 0.0008	0.0306 ± 0.0531 ± 0.0009
20	0.101	1.45	-0.0292 ± 0.0180 ± 0.0010	-0.0074 ± 0.0583 ± 0.0012
21	0.113	1.50	-0.0045 ± 0.0183 ± 0.0003	0.0279 ± 0.0645 ± 0.0003
22	0.128	1.54	0.0214 ± 0.0187 ± 0.0016	0.0716 ± 0.0716 ± 0.0023
23	0.144	1.59	0.0122 ± 0.0189 ± 0.0011	0.0691 ± 0.0794 ± 0.0018
24	0.162	1.63	0.0062 ± 0.0193 ± 0.0008	0.0718 ± 0.0884 ± 0.0014
25	0.182	1.67	-0.0021 ± 0.0196 ± 0.0004	0.0708 ± 0.0982 ± 0.0008
26	0.205	1.71	-0.0352 ± 0.0197 ± 0.0013	0.0192 ± 0.1089 ± 0.0027
27	0.230	1.74	0.0226 ± 0.0199 ± 0.0017	0.1632 ± 0.1216 ± 0.0038
28	0.259	1.77	-0.0088 ± 0.0199 ± 0.0001	0.1144 ± 0.1360 ± 0.0001
29	0.292	1.80	0.0227 ± 0.0199 ± 0.0017	0.2320 ± 0.1526 ± 0.0048
30	0.329	1.83	0.0095 ± 0.0193 ± 0.0010	0.2349 ± 0.1706 ± 0.0032

Table 25: Results for xg_2 and A_2 for the 2.75° spectrometer with the proton target at electron beam energy of 29 GeV.

x bin	$< x >$	$< Q^2 >$	$xg_2 \pm stat \pm syst$	$A_2 \pm stat \pm syst$
16	0.065	2.32	0.0141 ± 0.1531 ± 0.0005	0.0183 ± 0.0839 ± 0.0003
17	0.071	2.49	0.0353 ± 0.0636 ± 0.0016	0.0330 ± 0.0571 ± 0.0010
18	0.080	2.71	0.0325 ± 0.0409 ± 0.0014	0.0343 ± 0.0487 ± 0.0009
19	0.090	2.94	-0.0187 ± 0.0300 ± 0.0012	0.0035 ± 0.0446 ± 0.0008
20	0.101	3.17	0.0031 ± 0.0241 ± 0.0000	0.0214 ± 0.0429 ± 0.0000
21	0.114	3.40	0.0611 ± 0.0210 ± 0.0030	0.0700 ± 0.0433 ± 0.0023
22	0.128	3.62	0.0307 ± 0.0189 ± 0.0014	0.0528 ± 0.0445 ± 0.0012
23	0.144	3.85	-0.0306 ± 0.0177 ± 0.0017	0.0051 ± 0.0468 ± 0.0016
24	0.162	4.08	-0.0302 ± 0.0167 ± 0.0017	0.0096 ± 0.0496 ± 0.0017
25	0.182	4.30	-0.0101 ± 0.0158 ± 0.0006	0.0364 ± 0.0530 ± 0.0007
26	0.205	4.52	-0.0159 ± 0.0156 ± 0.0009	0.0379 ± 0.0580 ± 0.0011
27	0.230	4.74	-0.0335 ± 0.0154 ± 0.0018	0.0241 ± 0.0640 ± 0.0024
28	0.259	4.93	0.0136 ± 0.0154 ± 0.0006	0.1036 ± 0.0714 ± 0.0010
29	0.292	5.13	-0.0278 ± 0.0152 ± 0.0015	0.0516 ± 0.0800 ± 0.0026
30	0.328	5.31	-0.0254 ± 0.0148 ± 0.0014	0.0684 ± 0.0903 ± 0.0028
31	0.370	5.50	-0.0644 ± 0.0142 ± 0.0034	-0.0159 ± 0.1025 ± 0.0084
32	0.416	5.66	-0.0286 ± 0.0133 ± 0.0015	0.0834 ± 0.1171 ± 0.0047
33	0.468	5.81	-0.0385 ± 0.0123 ± 0.0020	0.0462 ± 0.1363 ± 0.0083
34	0.527	5.96	-0.0268 ± 0.0110 ± 0.0014	0.0872 ± 0.1596 ± 0.0080
35	0.592	6.08	-0.0148 ± 0.0094 ± 0.0008	0.1517 ± 0.1896 ± 0.0066
36	0.667	6.20	-0.0155 ± 0.0075 ± 0.0008	0.0966 ± 0.2286 ± 0.0112
37	0.750	6.30	-0.0162 ± 0.0052 ± 0.0008	-0.1063 ± 0.2831 ± 0.0230
38	0.844	6.39	-0.0055 ± 0.0029 ± 0.0003	-0.1186 ± 0.3854 ± 0.0237

Table 26: Results for xg_2 and A_2 for the 5.5° spectrometer with the proton target at electron beam energy of 29 GeV.

x bin	$< x >$	$< Q^2 >$	$xg_2 \pm stat \pm syst$	$A_2 \pm stat \pm syst$
20	0.102	4.40	-0.4078 ± 0.4444 ± 0.0197	-0.2220 ± 0.1539 ± 0.0115
21	0.115	4.89	-0.0329 ± 0.1329 ± 0.0001	-0.0009 ± 0.0896 ± 0.0001
22	0.128	5.34	0.1622 ± 0.0752 ± 0.0101	0.1289 ± 0.0715 ± 0.0066
23	0.144	5.90	0.0772 ± 0.0561 ± 0.0057	0.0806 ± 0.0661 ± 0.0040
24	0.162	6.51	-0.0607 ± 0.0451 ± 0.0014	-0.0142 ± 0.0635 ± 0.0010
25	0.182	7.17	-0.0412 ± 0.0372 ± 0.0003	0.0035 ± 0.0620 ± 0.0003
26	0.205	7.85	0.0079 ± 0.0340 ± 0.0022	0.0503 ± 0.0642 ± 0.0020
27	0.230	8.57	-0.0615 ± 0.0317 ± 0.0014	-0.0091 ± 0.0677 ± 0.0013
28	0.259	9.28	-0.0075 ± 0.0298 ± 0.0014	0.0523 ± 0.0725 ± 0.0016
29	0.292	10.04	-0.0691 ± 0.0281 ± 0.0019	-0.0162 ± 0.0787 ± 0.0024
30	0.328	10.83	-0.0102 ± 0.0263 ± 0.0011	0.0694 ± 0.0861 ± 0.0016
31	0.369	11.67	-0.0165 ± 0.0249 ± 0.0006	0.0692 ± 0.0965 ± 0.0011
32	0.415	12.48	-0.0263 ± 0.0233 ± 0.0001	0.0549 ± 0.1099 ± 0.0003
33	0.467	13.30	-0.0470 ± 0.0215 ± 0.0014	-0.0134 ± 0.1283 ± 0.0046
34	0.525	14.10	-0.0256 ± 0.0194 ± 0.0006	0.0382 ± 0.1536 ± 0.0028
35	0.591	14.93	-0.0262 ± 0.0168 ± 0.0009	-0.0165 ± 0.1892 ± 0.0065
36	0.665	15.70	0.0208 ± 0.0133 ± 0.0013	0.4817 ± 0.2397 ± 0.0185

Table 27: Results for xg_2 and A_2 for the 10.5° spectrometer with the proton target at electron beam energy of 29 GeV.

x bin	$< x >$	$< Q^2 >$	$xg_2 \pm stat \pm syst$	$A_2 \pm stat \pm syst$
6	0.020	0.81	-0.0032 ± 0.0346 ± 0.0003	0.0008 ± 0.0238 ± 0.0001
7	0.022	0.88	0.0035 ± 0.0232 ± 0.0006	0.0039 ± 0.0205 ± 0.0003
8	0.024	0.94	0.0186 ± 0.0200 ± 0.0014	0.0110 ± 0.0204 ± 0.0006
9	0.027	0.99	-0.0228 ± 0.0193 ± 0.0007	-0.0074 ± 0.0216 ± 0.0003
10	0.031	1.05	-0.0062 ± 0.0188 ± 0.0001	0.0010 ± 0.0231 ± 0.0001
11	0.035	1.12	0.0091 ± 0.0181 ± 0.0009	0.0097 ± 0.0244 ± 0.0005
12	0.039	1.19	0.0044 ± 0.0176 ± 0.0007	0.0083 ± 0.0261 ± 0.0004
13	0.044	1.26	0.0066 ± 0.0173 ± 0.0008	0.0110 ± 0.0280 ± 0.0005
14	0.049	1.32	-0.0036 ± 0.0177 ± 0.0003	0.0059 ± 0.0308 ± 0.0002
15	0.056	1.39	0.0059 ± 0.0169 ± 0.0008	0.0141 ± 0.0327 ± 0.0006
16	0.063	1.46	0.0213 ± 0.0167 ± 0.0016	0.0285 ± 0.0354 ± 0.0013
17	0.071	1.54	0.0259 ± 0.0164 ± 0.0019	0.0360 ± 0.0383 ± 0.0016
18	0.079	1.61	-0.0210 ± 0.0166 ± 0.0006	-0.0016 ± 0.0420 ± 0.0005
19	0.089	1.68	0.0046 ± 0.0169 ± 0.0008	0.0255 ± 0.0464 ± 0.0008
20	0.101	1.75	0.0111 ± 0.0172 ± 0.0011	0.0372 ± 0.0512 ± 0.0012
21	0.113	1.81	0.0038 ± 0.0174 ± 0.0008	0.0352 ± 0.0566 ± 0.0009
22	0.128	1.87	0.0026 ± 0.0176 ± 0.0007	0.0407 ± 0.0625 ± 0.0009
23	0.144	1.93	-0.0018 ± 0.0180 ± 0.0005	0.0432 ± 0.0694 ± 0.0007
24	0.162	1.99	0.0211 ± 0.0184 ± 0.0017	0.0877 ± 0.0775 ± 0.0025
25	0.182	2.04	-0.0477 ± 0.0185 ± 0.0019	-0.0116 ± 0.0860 ± 0.0032
26	0.205	2.09	0.0049 ± 0.0186 ± 0.0008	0.0920 ± 0.0954 ± 0.0015
27	0.230	2.14	-0.0313 ± 0.0186 ± 0.0011	0.0373 ± 0.1062 ± 0.0022
28	0.259	2.18	-0.0346 ± 0.0187 ± 0.0012	0.0443 ± 0.1189 ± 0.0028
29	0.292	2.22	-0.0118 ± 0.0184 ± 0.0001	0.1203 ± 0.1329 ± 0.0002
30	0.329	2.26	0.0060 ± 0.0177 ± 0.0008	0.2016 ± 0.1482 ± 0.0025

Table 28: Results for xg_2 and A_2 for the 2.75° spectrometer with the proton target at electron beam energy of 32 GeV.

x bin	$< x >$	$< Q^2 >$	$xg_2 \pm stat \pm syst$	$A_2 \pm stat \pm syst$
16	0.064	2.65	0.0611 ± 0.0897 ± 0.0029	0.0409 ± 0.0585 ± 0.0015
17	0.071	2.87	-0.0441 ± 0.0485 ± 0.0026	-0.0132 ± 0.0456 ± 0.0014
18	0.080	3.13	0.0222 ± 0.0329 ± 0.0009	0.0255 ± 0.0400 ± 0.0005
19	0.090	3.40	0.0155 ± 0.0253 ± 0.0005	0.0245 ± 0.0376 ± 0.0003
20	0.101	3.67	-0.0271 ± 0.0213 ± 0.0017	0.0001 ± 0.0370 ± 0.0011
21	0.113	3.94	0.0095 ± 0.0187 ± 0.0003	0.0278 ± 0.0375 ± 0.0002
22	0.128	4.22	0.0043 ± 0.0169 ± 0.0000	0.0286 ± 0.0387 ± 0.0000
23	0.144	4.50	-0.0012 ± 0.0159 ± 0.0002	0.0293 ± 0.0406 ± 0.0002
24	0.162	4.78	0.0133 ± 0.0150 ± 0.0005	0.0482 ± 0.0431 ± 0.0005
25	0.182	5.06	-0.0017 ± 0.0146 ± 0.0002	0.0420 ± 0.0467 ± 0.0002
26	0.205	5.33	-0.0009 ± 0.0143 ± 0.0002	0.0515 ± 0.0509 ± 0.0002
27	0.230	5.59	-0.0348 ± 0.0143 ± 0.0019	0.0208 ± 0.0566 ± 0.0023
28	0.259	5.85	-0.0094 ± 0.0141 ± 0.0006	0.0633 ± 0.0627 ± 0.0008
29	0.292	6.10	-0.0343 ± 0.0140 ± 0.0019	0.0369 ± 0.0706 ± 0.0030
30	0.328	6.33	-0.0069 ± 0.0135 ± 0.0004	0.0975 ± 0.0794 ± 0.0008
31	0.370	6.56	-0.0470 ± 0.0128 ± 0.0025	0.0234 ± 0.0899 ± 0.0058
32	0.416	6.77	-0.0264 ± 0.0120 ± 0.0014	0.0806 ± 0.1029 ± 0.0041
33	0.468	6.97	-0.0329 ± 0.0110 ± 0.0017	0.0591 ± 0.1198 ± 0.0067
34	0.527	7.17	-0.0197 ± 0.0097 ± 0.0010	0.1111 ± 0.1402 ± 0.0057
35	0.592	7.34	-0.0155 ± 0.0081 ± 0.0008	0.1240 ± 0.1670 ± 0.0067
36	0.667	7.50	-0.0099 ± 0.0063 ± 0.0005	0.1445 ± 0.2013 ± 0.0073
37	0.750	7.63	-0.0091 ± 0.0042 ± 0.0005	0.0446 ± 0.2501 ± 0.0136
38	0.844	7.76	0.0019 ± 0.0022 ± 0.0001	0.4796 ± 0.3407 ± 0.0090

Table 29: Results for xg_2 and A_2 for the 5.5° spectrometer with the proton target at electron beam energy of 32 GeV.

x bin	$< x >$	$< Q^2 >$	$xg_2 \pm stat \pm syst$	$A_2 \pm stat \pm syst$
20	0.102	4.99	-0.1303 ± 0.3678 ± 0.0051	-0.0547 ± 0.1301 ± 0.0028
21	0.115	5.55	-0.0138 ± 0.1098 ± 0.0010	0.0104 ± 0.0758 ± 0.0006
22	0.128	6.09	0.0261 ± 0.0639 ± 0.0031	0.0371 ± 0.0614 ± 0.0019
23	0.144	6.71	-0.0430 ± 0.0447 ± 0.0004	-0.0029 ± 0.0550 ± 0.0003
24	0.162	7.42	0.0449 ± 0.0350 ± 0.0042	0.0606 ± 0.0521 ± 0.0029
25	0.182	8.18	-0.0021 ± 0.0293 ± 0.0018	0.0329 ± 0.0513 ± 0.0014
26	0.205	8.97	0.0026 ± 0.0267 ± 0.0021	0.0428 ± 0.0532 ± 0.0017
27	0.230	9.82	-0.0157 ± 0.0254 ± 0.0011	0.0335 ± 0.0566 ± 0.0010
28	0.259	10.68	-0.0278 ± 0.0240 ± 0.0005	0.0279 ± 0.0608 ± 0.0005
29	0.292	11.59	-0.0593 ± 0.0227 ± 0.0012	-0.0040 ± 0.0660 ± 0.0015
30	0.328	12.52	-0.0148 ± 0.0213 ± 0.0009	0.0580 ± 0.0725 ± 0.0013
31	0.369	13.49	-0.0649 ± 0.0198 ± 0.0018	-0.0199 ± 0.0806 ± 0.0032
32	0.416	14.45	-0.0378 ± 0.0183 ± 0.0007	0.0244 ± 0.0914 ± 0.0015
33	0.467	15.41	-0.0105 ± 0.0165 ± 0.0005	0.0948 ± 0.1058 ± 0.0015
34	0.526	16.38	-0.0432 ± 0.0146 ± 0.0015	-0.0465 ± 0.1259 ± 0.0066
35	0.591	17.35	-0.0187 ± 0.0124 ± 0.0005	0.0305 ± 0.1540 ± 0.0035
36	0.664	18.28	-0.0025 ± 0.0098 ± 0.0001	0.1480 ± 0.1962 ± 0.0018

Table 30: Results for xg_2 and A_2 for the 10.5° spectrometer with the proton target at electron beam energy of 32 GeV.

APPENDIX D

Tables of radiative corrections

The following tables give the radiative corrections used for determining the results in this dissertation. These radiative corrections were generated in the summer of 2001. New sets of radiative corrections are currently still being worked and should be available in the E155X paper to be published in Physics Letters. Tables 31, 32, and 33, contain the radiative corrections for the proton target at electron beam energy of 29 GeV, respectively for the 2.75°, 5.5° and 10.5° spectrometers. Tables 34, 35, and 36, contain the radiative corrections for the proton target at electron beam energy of 32 GeV, respectively for the 2.75°, 5.5° and 10.5° spectrometers.

$< x >$	$< Q^2 >$	f_{RC}	A_{RC}
0.011	0.51	0.455	-0.132
0.012	0.56	0.526	-0.126
0.014	0.56	0.702	-0.111
0.015	0.62	0.738	-0.120
0.017	0.67	0.770	-0.123
0.019	0.73	0.802	-0.133
0.022	0.79	0.834	-0.145
0.024	0.87	0.859	-0.162
0.027	0.94	0.882	-0.182
0.031	1.02	0.901	-0.196
0.035	1.07	0.922	-0.203
0.039	1.13	0.938	-0.204
0.044	1.18	0.950	-0.208
0.049	1.24	0.959	-0.216
0.056	1.30	0.967	-0.226
0.063	1.36	0.972	-0.230
0.071	1.42	0.975	-0.241
0.080	1.48	0.979	-0.251
0.089	1.54	0.983	-0.256
0.101	1.59	0.985	-0.265
0.113	1.65	0.986	-0.274
0.128	1.70	0.989	-0.278
0.144	1.74	0.988	-0.279
0.162	1.79	0.990	-0.277
0.182	1.83	0.990	-0.271
0.205	1.87	0.990	-0.266
0.231	1.91	0.990	-0.261
0.260	1.95	0.990	-0.252
0.292	1.99	0.989	-0.228
0.329	2.01	0.988	-0.213

Table 31: Radiative corrections for the 2.75° spectrometer with the proton target at electron beam energy of 29 GeV.

$< x >$	$< Q^2 >$	f_{RC}	A_{RC}
0.019	1.04	0.073	-2.138
0.022	1.15	0.178	0.169
0.024	1.28	0.282	0.285
0.027	1.42	0.388	0.280
0.031	1.57	0.487	0.290
0.035	1.73	0.579	0.325
0.039	1.90	0.661	0.376
0.044	2.09	0.731	0.425
0.050	2.29	0.790	0.466
0.056	2.50	0.841	0.491
0.064	2.50	0.927	0.363
0.071	2.72	0.944	0.388
0.080	2.96	0.956	0.415
0.090	3.20	0.966	0.443
0.101	3.46	0.975	0.469
0.114	3.71	0.985	0.480
0.128	3.96	0.987	0.492
0.144	4.22	0.990	0.498
0.162	4.48	0.992	0.496
0.182	4.74	0.994	0.489
0.205	4.99	0.996	0.473
0.231	5.23	0.996	0.457
0.260	5.46	0.998	0.426
0.292	5.69	0.998	0.397
0.329	5.92	0.998	0.357
0.370	6.13	0.998	0.317
0.417	6.32	0.999	0.265
0.469	6.51	0.999	0.210
0.527	6.69	0.998	0.146
0.594	6.86	0.998	0.066
0.668	7.00	0.996	-0.057
0.752	7.13	0.992	0.045
0.847	7.28	0.968	0.341

Table 32: Radiative corrections for the 5.5° spectrometer with the proton target at electron beam energy of 29 GeV.

$< x >$	$< Q^2 >$	f_{RC}	A_{RC}
0.071	3.82	0.200	9.031
0.080	4.24	0.372	1.083
0.090	4.70	0.519	-0.436
0.102	4.81	0.871	-0.834
0.114	5.31	0.905	-0.854
0.128	5.86	0.930	-0.868
0.144	6.44	0.949	-0.873
0.162	7.08	0.963	-0.876
0.182	7.80	0.971	-0.863
0.205	8.58	0.979	-0.852
0.231	9.36	0.984	-0.813
0.260	10.14	0.989	-0.766
0.292	10.99	0.992	-0.721
0.329	11.86	0.994	-0.677
0.370	12.73	0.995	-0.617
0.416	13.61	0.997	-0.550
0.468	14.51	0.997	-0.473
0.527	15.42	0.999	-0.385
0.593	16.32	0.999	-0.290
0.668	17.23	0.999	-0.184
0.753	18.14	0.999	-0.086
0.849	20.84	0.997	-0.054

Table 33: Radiative corrections for the 10.5° spectrometer with the proton target at electron beam energy of 29 GeV.

$< x >$	$< Q^2 >$	f_{RC}	A_{RC}
0.011	0.51	0.632	-0.099
0.012	0.56	0.677	-0.102
0.014	0.60	0.744	-0.106
0.015	0.66	0.773	-0.115
0.017	0.72	0.802	-0.119
0.019	0.78	0.831	-0.128
0.022	0.85	0.857	-0.139
0.024	0.93	0.880	-0.156
0.027	1.01	0.899	-0.171
0.031	1.08	0.918	-0.184
0.035	1.14	0.934	-0.191
0.039	1.21	0.947	-0.191
0.044	1.28	0.957	-0.195
0.049	1.34	0.965	-0.201
0.056	1.41	0.971	-0.210
0.063	1.49	0.977	-0.218
0.071	1.56	0.981	-0.226
0.079	1.63	0.983	-0.237
0.089	1.70	0.985	-0.245
0.101	1.76	0.991	-0.251
0.113	1.82	0.989	-0.259
0.128	1.88	0.989	-0.265
0.144	1.94	0.992	-0.266
0.162	2.00	0.992	-0.265
0.182	2.05	0.993	-0.262
0.205	2.10	0.993	-0.256
0.230	2.14	0.992	-0.245
0.260	2.19	0.992	-0.231
0.292	2.23	0.992	-0.222
0.329	2.27	0.991	-0.208

Table 34: Radiative corrections for the 2.75° spectrometer with the proton target at electron beam energy of 32 GeV.

$< x >$	$< Q^2 >$	f_{RC}	A_{RC}
0.019	1.04	0.543	0.176
0.022	1.15	0.596	0.181
0.024	1.28	0.648	0.198
0.027	1.42	0.697	0.227
0.031	1.57	0.744	0.257
0.035	1.73	0.788	0.288
0.039	1.90	0.826	0.311
0.044	2.09	0.860	0.337
0.050	2.29	0.889	0.340
0.057	2.46	0.927	0.327
0.063	2.67	0.943	0.329
0.071	2.91	0.956	0.353
0.080	3.17	0.966	0.378
0.090	3.43	0.974	0.403
0.101	3.71	0.980	0.428
0.113	3.98	0.985	0.443
0.128	4.26	0.989	0.448
0.144	4.54	0.992	0.454
0.162	4.83	0.993	0.455
0.182	5.11	0.995	0.450
0.205	5.39	0.996	0.438
0.231	5.65	0.997	0.421
0.260	5.92	0.998	0.396
0.292	6.18	0.998	0.366
0.329	6.42	0.999	0.328
0.370	6.66	0.999	0.288
0.417	6.89	0.999	0.241
0.469	7.09	0.999	0.190
0.528	7.29	0.999	0.134
0.594	7.48	0.998	0.065
0.668	7.66	0.997	-0.016
0.752	7.83	0.993	-0.025
0.846	7.98	0.977	0.260

Table 35: Radiative corrections for the 5.5° spectrometer with the proton target at electron beam energy of 32 GeV.

$< x >$	$< Q^2 >$	f_{RC}	A_{RC}
0.071	3.82	0.787	-0.720
0.080	4.24	0.832	-0.701
0.092	4.65	0.904	-0.670
0.102	5.11	0.922	-0.705
0.114	5.64	0.939	-0.745
0.128	6.21	0.953	-0.764
0.144	6.86	0.965	-0.773
0.162	7.57	0.974	-0.766
0.182	8.31	0.980	-0.756
0.205	9.13	0.984	-0.747
0.231	9.98	0.988	-0.725
0.259	10.84	0.991	-0.692
0.292	11.77	0.993	-0.655
0.329	12.69	0.994	-0.618
0.370	13.64	0.996	-0.566
0.416	14.61	0.997	-0.505
0.468	15.62	0.998	-0.437
0.527	16.63	0.998	-0.356
0.593	17.63	0.999	-0.267
0.667	18.54	0.999	-0.170
0.753	19.53	0.999	-0.077
0.847	20.57	0.997	-0.034

Table 36: Radiative corrections for the 10.5° spectrometer with the proton target at electron beam energy of 32 GeV.

BIBLIOGRAPHY

[1] P. L. Anthony *et al.* [E142 Collaboration], Phys. Rev. D **54**, 6620 (1996) [hep-ex/9610007].

[2] K. Abe *et al.* [E143 collaboration], Phys. Rev. D **58**, 112003 (1998) [hep-ph/9802357].

[3] K. Abe *et al.* [E154 Collaboration], Phys. Lett. B **404**, 377 (1997) [hep-ex/9705017].

[4] K. Abe *et al.* [E154 Collaboration], Phys. Lett. B **405**, 180 (1997) [hep-ph/9705344].

[5] K. Abe *et al.* [E154 Collaboration], Phys. Rev. Lett. **79**, 26 (1997) [hep-ex/9705012].

[6] P. L. Anthony *et al.* [E155 Collaboration], Phys. Lett. B **458**, 529 (1999) [hep-ex/9901006].

[7] P. L. Anthony *et al.* [E155 Collaboration], Phys. Lett. B **463**, 339 (1999) [hep-ex/9904002].

[8] P. L. Anthony *et al.* [E155 Collaboration], Phys. Lett. B **493**, 19 (2000) [hep-ph/0007248].

[9] J. Ashman *et al.* [European Muon Collaboration], Phys. Lett. B **206**, 364 (1988).

[10] D. Adams *et al.* [Spin Muon Collaboration (SMC)], Phys. Lett. B **336**, 125 (1994) [hep-ex/9408001].

[11] K. Ackerstaff *et al.* [HERMES Collaboration], Phys. Lett. B **404**, 383 (1997) [hep-ex/9703005].

[12] A. Airapetian *et al.* [HERMES Collaboration], Phys. Lett. B **442**, 484 (1998) [hep-ex/9807015].

[13] M. Anselmino, A. Efremov and E. Leader Phys. Rept. **261**, 1 (1995) [hep-ph/9501369].

[14] J. D. Bjorken, Phys. Rev. **D1**, 1376 (1970).

[15] K. G. Wilson, Phys. Rev. **179**, 416 (1974).

[16] Leader and Predazzi, "An introduction to Gauge Theories and the 'New Physics', *Cambridge University Press 1982, 362 (1982).*

[17] R. Jaffe and X. Ji, Phys. Rev. D **43**, 724 (1991).

[18] M. Göckeler *et al.*, Phys. Rev. D **63**, 074506 (2001).

[19] S. Wandzura and F. Wilczek, Phys. Lett. **B72**, 195 (1977).

[20] E. Leader, University of London, Private Communication (2001).

[21] P. DePietro, Ph. D. thesis, American University (December 2001), unpublished.

[22] H. Burkhardt and W. Cottingham, Ann. Phys. **56**, 453 (1970).

[23] G. Altarelli et al., Phys. Lett. B **334**, 187 (1994).

[24] I. Ivanov et al., Phys. Rep. **320**, 175 (1999).

[25] A. Efremov, O. Teryaev and E. Leader, hep-ph/9607217 (1996).

[26] EMC, J. Aubert et al., Phys. Lett. B **123**, 175 (1983).

[27] R. Jaffe Phys. Rev. D **11**, 7 (1975).

[28] A. W. Schreiber, A. I. Signal, A. W. Thomas, Phys. Rev. D **44**, 2653 (1991).

[29] T. DeGrand et al., Phys. Rev. D **12**, 2060 (1975).

[30] M. Stratmann, Z. Phys. C **60** 763-771 (1993).

[31] G. Altarelli, G. Parisi, Nucl. Phys. B **126** 298 (1977).

[32] A. Ali, V.M. Braun, G. Hiller, Phys. Lett. B **266** 117 (1991).

[33] X. Song, [hep-ph/9604264] (1996).

[34] H. Weigel and L. Gamberg, [hep-ph/0004057] (2000).

[35] Y. Nambu and G. Jona-Lasinio, Phys. Rev. **122**, 1 (1961).

[36] J. Bardeen, L. Cooper and J. Scheiffer, Phys. Rev. **106**, 162 (1957).

[37] J. Soffer, [hep-ph/0005132] (2000).

[38] R. Alley et al., Nucl. Instr. Meth. **A365**, 1 (1995).

[39] K. Griffioen, E155 Technical Note #90 (1999), unpublished.

[40] G.S. Mitchell, Ph. D. thesis, University of Wisconsin, unpublished, SLAC-R-540 (June 1999).

[41] T. D. Averett, Ph. D. thesis, University of Virginia (August 1995), unpublished.

[42] P. Mckee, Ph. D. thesis, University of Virginia (August 2000), unpublished.

[43] G. R. Court et al. Nucl. Instr. and Meth., A324, 433 (1993)

[44] G. Petratos et al., SLAC-PUB 5678 (1991).

[45] P. Bosted, E155 Technical Note #10 (1996), unpublished.

[46] P. King, E155 Technical Note #47 (1998), unpublished.

[47] L. Sorrell, E155 Technical Note #48 (1998), unpublished.

[48] T. S. Toole, Ph. D. thesis American University (September 2000), unpublished.

[49] J. Groves and J. Olmsted, E155 Technical Note #23 (1996), unpublished.

[50] J. D. Jackson "Classical Electrodynamics," *John Wiley & Sons, Inc. (1998).*

[51] C. Prescott, E155 Technical Note #25 (1996), unpublished.

[52] W. R. Leo "Techniques for Nuclear and Particle Physics Experiments" *Springer-Verlag (1994).*

[53] P. Bosted, E155 Technical Note #64 (1998), unpublished.

[54] P. King, Ph. D. thesis, The College of William and Mary (July 2000), p.75-85, unpublished.

[55] K. Brown and R. Lindgren, E155 Technical Note #87 (1999), unpublished.

[56] N. Benmouna, E155 Technical Note #106 (1999), unpublished.

[57] N. Benmouna, E155 Technical Note #107 (1999), unpublished.

[58] P. King, E155 Technical Note #71 (1999), unpublished.

[59] N. Benmouna, E155 Technical Note #72 (1999), unpublished.

[60] P. DePietro, E155 Technical Note #73 (1999), unpublished.

[61] M. Olson, Ph. D. thesis, Kent University (May 1999), unpublished.

[62] P.L. Anthony and Z.M. Szalata, SLAC-PUB-7201 (1996).

[63] Yu. G. Kolomensky, Ph. D. thesis, University of Massachusetts, Amherst, SLAC-R-503 (February 1997).

[64] L. Sorrell, E155 Technical Note #113 (2000), unpublished.

[65] L. Sorrell, E155 Technical Note #114 (2000), unpublished.

[66] N. Benmouna, E155 Technical Note #92 (1999), unpublished.

[67] N. Benmouna, E155 Technical Note #83 (1999), unpublished.

[68] T.R. Wright,H.R. Band, E155 Technical Note #108 (2000), unpublished.

[69] S. Bueltmann, E155 Technical Note #84 (1999), unpublished.

[70] D. McNulty, E155 Technical Note #119 (2001), unpublished.

[71] J. Bauer, E143 Technical Note #71 (1994), unpublished.

[72] T. Averett, E155 Technical Note #27 (1997), unpublished.

[73] SLAC-proposal E149 *bis*.

[74] P. Bosted, E154 Technical Note #29 (1995), unpublished.

[75] N. Benmouna, P. Depietro E155 Technical Note #115 (2000), unpublished.

[76] K. Griffioen, E155 Technical Note #121 (2001).

[77] D. Reyna , Ph. D. thesis, American University, (1998).

[78] N. Benmouna, P. Bosted, E155 Technical Note #109 (2000), unpublished.

[79] M. Arneodo *et al.*, Phys. Lett. B **364**, 107 (1995).

[80] K. Abe *et al.*, Phys. Lett. B **452**, 194 (1999).

[81] E. Shurayk and A. Vainshtein, Nuc. Phys. B **201**, 141 (1992).

[82] E. Stein *et al.*, Phys. Lett. B **343**, 369 (1995).

[83] I. Balitsky, V. Braun and A. Kolesnichenko, Phys. Lett. B **242**, 245 (1990); **318**, 648 (1993) (Erratum).

[84] B. Ehrnsperger and A. Schafer, Phys. Rev. D **52**, 2709 (1995).

[85] N. Benmouna, E155 Technical Note #120 (2001).